Università Campus Bio-Medico di Roma

Corso di dottorato di ricerca in Bioingegneria e Bioscienze
XXXII ciclo a.a. 2016-2017

Substituting and Augmenting Humans with Robots

Alessia Noccaro

Supervisor
Prof. Domenico Formica

Co-Supervisor
Prof. Giovanni Di Pino

November 2020

Abstract

Humans have attempted to develop substitutes able to execute their tasks and mimic their behavior. Robots represent the answer to this research, which leads to industrial robots, social humanoids robots, prostheses, that can replace humans in difficult tasks, help them like a relative and restore their lost limbs.
Moreover recent years have seen the growth of robots to augment and enhance healthy humans, providing supernumerary robotic limbs that open a range of new possibilities.

This thesis aims to investigate the use of robots to both substitute and augment humans. The first part presents three substitution scenarios: i) teleoperation of a 7 dof robotic manipulator using M-IMU sensors; ii) teleoperation of a virtual avatar using stereotaxic systems to investigate multisensory integration; iii) development of a robot-aided Transcranial Magnetic Stimulation (TMS) platform to substitute and improve the performance of expert operators.

The second part focuses indeed on the use of supernumerary limbs, addressing three main aspects: i) how humans perform in three-hands tasks; ii) control of a supernumerary limb through high density EMG interface; iii) a vibrotactile interface to provide proprioceptive feedback of a supernumerary robotic limb.

Besides proposing useful a reproducible implementation, this thesis also presents the validation of the proposed solutions, whose main results can be resumed as follows: i) in teleoperation reaching tasks with an anthropomorphic robotic arm constraining the robot elbow configuration to be as close as possible to the human elbow one improves the control performance; ii) the proposed VR platform allows to investigate multisensory integration and confirmed the existence of an-hand-centered peripersonal space; iii) the proposed robot-aided TMS platform reresents a low-cost and reproducible alternative to the few devices commercially available; iv) the optimization approach allows to significantly decrease the calibration errors regardless of the mathematical implementation; v) the platform allows to elicit MEP amplitudes comparable with the ones measured in manual sessions, reducing the coil orientation error by 46% with respect to expert operators; vi) in three hands tasks people perform better in 3-coupled task than in independent or 2-coupled and in general perform better in couple rather than in solo sessions; vii) the validation of the proposed EMG interface for 2 dof control proved the system proper functioning and easiness of use; viii) the

proposed vibrotactile interface allows to effectively identify the end-effector position of a supernumerary robotic limb when the proprioceptive feedback is conveyed as end-effector cartesian information.

Table of contents

List of Publications

[1] A. Noccaro, L. Raiano, G. Di Pino, and D. Formica, "Evaluation of hand-eye and robot-world calibration algorithms for tms application," in *2018 7th IEEE International Conference on Biomedical Robotics and Biomechatronics (Biorob)*. IEEE, 2018, pp. 1115–1119.

[2] L. Raiano, G. Di Pino, A. Noccaro, D. Accoto, and D. Formica, "Design of a wearable mechatronic device to measure the wrist rigidity in parkinson's disease patients," in *2018 7th IEEE International Conference on Biomedical Robotics and Biomechatronics (Biorob)*. IEEE, 2018, pp. 497–502.

[3] A. Noccaro, F. Cordella, L. Zollo, G. Di Pino, E. Guglielmelli, and D. Formica, "A teleoperated control approach for anthropomorphic manipulator using magneto-inertial sensors," in *2017 26th IEEE International Symposium on Robot and Human Interactive Communication (RO-MAN)*. IEEE, 2017, pp. 156–161.

[4] F. Le Jeune, M. D'Alonzo, A. Noccaro, L. Raiano, D. Formica, and G. Di Pino, "Manipulating the body representation: Assessment of a novel platform," in *2020 42nd Annual International Conference of the IEEE Engineering in Medicine & Biology Society (EMBC)*. IEEE, 2020, pp. 3248–3251.

[5] A. Noccaro, M. Pinardi, D. Formica, and G. Di Pino, "A virtual reality platform for multisensory integration studies," in *2020 42nd Annual International Conference of the IEEE Engineering in Medicine & Biology Society (EMBC)*. IEEE, 2020, pp. 3244–3247.

[6] A. Noccaro, L. Raiano, M. Pinardi, D. Formica, and G. Di Pino, "A novel proprioceptive feedback system for supernumerary robotic limb," 2020, accepted in 9th IEEE International Conference on Biomedical Robotics and Biomechatronics (Biorob).

[7] A. Noccaro, A. Mioli, M. D'Alonzo, M. Pinardi, G. Di Pino, and D. Formica, "Development and validation of a novel calibration methodology and control approach for

robot-aided transcranial magnetic stimulation (tms)," 2020, under Third Review in IEEE Transaction on Biomedical Engineering.

[8] A. Noccaro, J. Eden, G. Di Pino, E. Burdet, and D. Formica, "Human performance in three-hands tasks," 2020, in preparation.

List of figures

List of tables

Chapter 1

Introduction

Over the centuries, social, philosophical, economic and scientific motivations have driven humans to find substitutes able to replace them in the execution of tasks, mimicking their behavior [1]. The word *robot* derives from the Slav *robota*, that means serf, and was used the first time in 1921 by Karel Capek in the satirical play Rossum's Universal Robots [2]. Capek depicted robots as machines resembling people but working tirelessly. In the 1940s the science fiction writer Asimov introduced the term *robotics* as the science devoted to the study of robots.

Nowadays robots are a constant presence in everyday life, from the industrial manipulators that execute repetitive pick-and-place tasks, through the social humanoid robots that help old people and autistic children, to robotic prostheses that replace lost limbs in amputees. Furthermore robotic interfaces were developed on one hand to restore missing sensorimotor functions of disabled people and on the other hand to enhance able-bodied capabilities.
Beyond the traditional concept of robots substituting human limbs, in the last years researchers have been investigating the promising topic of adding robotic extra limbs to humans [3], [4]. Supernumerary robotic limbs could on the one hand help people affected by neurological diseases and on the other hand augment humans capabilities [5]. In the augmentation scenario it is important to investigate if and how humans are able to adapt themselves to integrate external additional limb into their sensorimotor representation [6].
Several studies assessed that the use of a bidirectional human-machine interface induces human brain plasticity, i.e. the brain ability to adapt its structure and functional connections to promote novel functions in response to external conditions [7].
Another crucial aspect in the augmentation is the cross-modal plasticity. Multisensory mechanisms build the representation of the body in the brain, which are able to integrate external objects; such integration process is known as embodiment [8]. In order to embody supernumerary limbs, multisensory integration neurons enlarge their receptive fields in the

premotor cortex -involved in the motor representation and control of an external tools- and in the intraparietal sulcus -involved in the visual representation of the tool. In other words, the augmentation-related plasticity can lead to the control and the feeling of a supernumerary limb as a natural limb. So far, the knowledge on this topic is limited, but can be extended through the investigation of sensorimotor training, cross-modal plasticity, sensory and motor substitution, embodiment of external tools.

A useful tool to modulate and analyze non-invasively the brain activity is the Transcranial Magnetic Stimulation (TMS), a non-invasive brain stimulation technique widely used in clinics and research. TMS induces cortical currents using an electromagnetic field generated by a coil placed over the scalp. Typically, the stimulation is manually administered by expert operators, leading to user-dependent performance, limited accuracy and lack of repetability. Last years have seen few attempts to overcome those drawbacks employing robotic devices.

In this work we aim to investigate how robotic technologies can be employed not only to substitute humans but also to enhance their functionality in augmentation scenarios.

Typical examples of robots conceived to substitute missing parts of the human body are prostheses and wearable robots. However, not only amputees need to replace their limbs with robotic devices, also healthy people working in dangerous environment need to use a robotic arm instead of their own to move hazardous materials. This concept of extending humans' sensing and manipulation capabilities to a remote location is called *teleoperation*. *Telerobotics* is a form of teleoperation where the user supervise a subordinate robot (slave) that executes a task following direct commands provided by the user through an interface (master) [9].

In the second chapter we describe how an anthropomorphic robot can be teleoperated using magneto-inertial sensors to track human arm movements. Since the anthropomorphism plays a key role also for the embodiment of external tools, this aspect is further analyzed, exploiting the robot redundancy to implement and compare different anthropomorphic criteria to constraint the robot motion.

The third chapter presents a similar teleoperation strategy using the human arm as master, but to control a virtual human avatar. This teleoperated platform aims to investigate the above-mentioned multisensory integration, providing the user with multimodal stimuli and recording a set of features such as reaction time, hand position, stimuli intensity, etc. Although the system represents an example of teleoperation, it is a useful tool to investigate the cross-modal plasticity involved in the augmentation; an example is indeed the study -used for the system validation- of the peripersonal space, i.e. the part of the space where a subject is able to act through his limbs.

Going further in the human substitution, we present in chapter 4 a robot-aided TMS platform

that allows to automatically administer TMS increasing the coil accuracy positioning compared to a human operator. As for the previous chapter, this platform represents an example of substitution (demanding to the user only the stimulation protocol setting), that can be used to increase the knowledge about the augmentation.
This chapter concludes the first part of the thesis, about substitution solutions. The following three chapters deal with the augmentation topic analyzing its main aspects: i) human performance in augmentation tasks; ii) control of supernumerary limb; iii) feedback from supernumerary limb.
Chapter 5 presents a detailed analysis of the human performance in three-hands tasks, comparing on one side scenarios with different levels of mechanical coupling between the limbs and on the other side people working alone or sharing the control with dyads.
The control is the focus of chapter 6, that presents the development and validation of a 2-dof EMG interface for the leg to control an extra limb.
To conclude our study on the augmentation topic, chapter 7 describes a novel interface to provide the feedback of a supernumerary robotic limb.
Finally, chapter 8 summarizes the major findings and the relevance of the present work.

Author's contribution

Summing up, the author aims to investigate how robots can enhance humans' capabilities, starting from the substitution of the user's arm, both in a real and in a virtual environment, going through the complete substitution of the user with a robotic platform, and ending with the use of a robotic manipulator as additional limb in three-hands tasks.

Part I

The first part of the work addresses the use of robots as user's substitutes, but it represents also a prelude of the second part, i.e. the augmentation problem. Indeed, the investigation of different control strategies to substitute human's motion can be considered as preparatory for the augmentation tasks, where the user has to control the robot, achieving good performance.
Although the substitution topic has a wide range of application scenarios, the author focused on specific applications useful for the second part of the work:

- **Teleoperation and Anthropomorphism**: since the embodiment of an external limb increases if the fake limb appears human-like, the author wondered if the embodiment of an anthropomorphic manipulator, and the performance controlling it, vary forcing the robot motion to be human-like. This aspect is addressed in chapter 2, where healthy subjects teleoperated a 7 dof robotic manipulator in reaching tasks, using different control strategies that exploit the redundancy of the robot to implement

anthropomorphic criteria or to minimize a cost function typically used in robotics to avoid singularities.

- **Virtual Reality and Multisensory Integration**: the author goes deeper investigating the brain mechanisms beyond the embodiment of an external tool, i.e. the multisensory integration. The author implements a teleoperated control in a virtual environment to test with a single platform the many processes of multisensory integration. The platform, presented in chapter 3, is validated on healthy subjects to test the peripersonal space.

- **Robot-aided TMS platform**: in chapter 4 the author proposed a robotic TMS platform, useful for several protocols to non-invasively inhibit or excite brain areas. The platform represents an automatic and more comfortable stimulation system, able to substitute the manual approach used so far, improving the accuracy and the repeatability. In particular, the author proposes an optimization method to reduce the calibration errors and a control strategy based on the impedance regulation.

Part II

The objective of the second part is the augmentation: this topic, partially introduced in the first part, is here analyzed deeper. The topic is divided in three main sections:

- **Trimanual Tasks**: first in chapter 5, the author analyzes three-hands tasks in order to understand if a "super-human" with three hands perform better or worse that two "normal people" working together, and if this result varies across the scenarios. Three cases are investigated: i) three independent sub-tasks; ii) two independent sub-tasks with a virtual mechanical coupling between the two hands; iii) one single task with all three limbs mechanically coupled in the virtual environment.

- **EMG Control of a Supernumerary Limb**: then the author proposes a 2-dof EMG control interface for additional robotic limbs. The interface is designed for the leg, to not interfere with the natural arm movements in three-hands tasks. Chapter 6 presents the interface implementation and validation controlling a virtual cursor on a screen.

- **Proprioceptive Feedback of a Supernumerary Limb**: chapter 7 presents the validation of a vibrotactile system to provide proprioceptive feedback of a supernumerary robotic limb. The author aims here to close the loop providing the bi-directional communication needed to embody and efficiently control an external tool. The system is designed to be as intuitive as possible and is used for the comparison of different encoding strategies to convey the robot state (i.e. the end-effector position and the torque applied to the 2 active joints).

Chapter 2

Teleoperated Control of an Anthropomorphic manipulator using M-IMU sensors

This chapter presents a case of human arm substitution with a robotic manipulator. The anthropomorphic robot is controlled by the arm movements using M-IMU sensors. The study focuses on the analysis of human performance teleoperating the robot, with and without the implementation of anthropomorphic limitations on the robot motion.

2.1 Background

Teleoperation was introduced for controlling robotic manipulators operating in hazardous environments [10]. Later, it was used in many other applications, such as robot-assisted surgery [11] and tele-rehabilitation [12]. A telerobotic system is composed of a master and a slave robot, with the slave usually controlled by a human operator through the master interface.
Several slaves exhibit anthropomorphic kinematic chain (and appearance). Indeed, the introduction of anthropomorphic criteria in robot design has several advantages: (i) safety improvements during human-robot interaction, since the human subjects can predict more easily human-like robot motion, (ii) higher robot acceptance from the human beings, (iii) more intuitive control from the user when his/her movements are mapped into movements of the slave side [13] [14] [15]. Furthermore, the redundancy of the anthropomorphic robots allows to achieve movements that are comparable to the one performed by the operator arm (that is a redundant manipulator from a kinematic viewpoint) [16].

The input provided by the human operator on the master side can be acquired by different devices, which are usually robots, joysticks or other systems, which in general have different kinematics, number of Degrees of Freedom (DoFs) and workspace than the slave robot [10]. Therefore, the human operator typically needs a specific training to learn how to control the slave.

An alternative approach consists in using a motion tracking system for acquiring the human movements (such as cameras [17], magneto-inertial sensors (IMUs) [18]), and map them onto robot movements. In this case, the similarity between the human arm and the anthropomorphic robot in terms of kinematic chain, allows the user to control more easily and intuitively the robotic platform by means of free movements performed on the master side, thus not requiring particular skills or training to use the interface.

Once the master movements are acquired, they should be mapped into corresponding slave movements by means of an appropriate human to robot motion mapping. Several mapping strategies are proposed in the literature such as joint-to-joint, fingertip, functional pose and object-specific mapping [19] [20].
The fingertips mapping is the most adopted method in the literature since, unlike the other methods, it can be easily adapted to a wide range of systems even though it is conceived for hand motion mapping. It is based on the computation of forward kinematics for each human finger to obtain their positions in 3D space. Then the inverse kinematics for each robotic finger is computed, achieving the same 3D positions of the human one [21].
Most of the studies proposed in the literature adopted the fingertip method for mapping the motion of a human arm on robotic manipulators, focusing on achieving high accuracy in terms of end-effector pose, but without taking into account anthropomorphic criteria not allowing to achieve the same configuration for the human and the robot arm in the joint space [15].

Therefore, the main objective of the study presented in this chapter is to overcome this limitation by proposing a teleoperated control approach for an anthropomorphic robot manipulator that allows mapping the motion of the human hand on the robot end-effector by exploiting a fingertip mapping method and meeting anthropomorphic criteria in the joint space. Three different inverse kinematics algorithms (i.e. Damped Least Squares (DLS) [10], Elastic Potential (EP) [10] and Augmented Jacobian (AJ) [22]) are compared in order to find the best method for control the robot arm [23] [24]. The EP and AJ methods basically exploit the robot redundancy in order to achieve anthropomorphic configurations of the kinematic chain.

It is interesting to note that the proposed teleoperated control can be intuitively and easily used by the subjects since the human motion tracking on the master side is achieved by means

of magneto-inertial sensors positioned on the subject arm. The user can control the robot arm by freely moving his/her own arm guaranteeing in this way a wide extended workspace. Furthermore, the setup time is low as well as the costs of the master system. This makes the system suitable for industrial environment so as for everyday life contexts, such as assistive or rehabilitation scenarios.

The proposed approach has been experimentally validated on the anthropomorphic robotic arm Kuka Light Weight Robot (LWR) 4+ [25], controlled by the user through four Xsens Wireless Motion Tracking sensors (MTw) [26]. An experimental study on four healthy subjects have been carried out in order to compare the performance of the three inverse kinematic algorithms. The recruited subjects were asked to control the robotic arm to reach three target poses in the robot workspace by using the three teleoperated controls. Position and orientation errors between human hand and robot end-effector were evaluated to assess task performances. Additionally for the EP and AJ approaches the position error between the human and the robot elbow joint was evaluated as anthropomorphism index.

2.2 Methods

2.2.1 Proposed approach

The proposed teleoperated control strategy is based on a forward-inverse kinematics approach for human to robot motion mapping (see Fig. 2.1). On the master side the human arm motion was acquired by a motion tracking system, which provides human arm forward kinematics (see Sect. 2.2.3). Then, the inverse kinematics was computed for providing the robot joint angle values, achieving a robot end-effector pose equal to the one of the human hand (see Sect. 2.2.4). Moreover, taking advantage of the robot redundancy, the initial configuration was selected in order to obtain a robot-human joint correspondence. On the slave side three different inverse kinematics algorithms were implemented and compared. In particular, elbow position data were processed in the EP and in the AJ methods in order to achieve human-like robot motion. Indeed, previous studies investigated the human motion, focusing on what anthropomorphism means and how it can be measured, expecially for replicating it on an arm-hand robotic system [23], [24], [27]. In the end, anthropomorphism and its measure have been defined through the comparison between human and robot motion. Many comparison criteria have been proposed and analyzed. Among them, the minimization of the distance between human and robot elbow joints resulted to be the best criterion for obtaining an anthropomorphic motion with the robotic system.

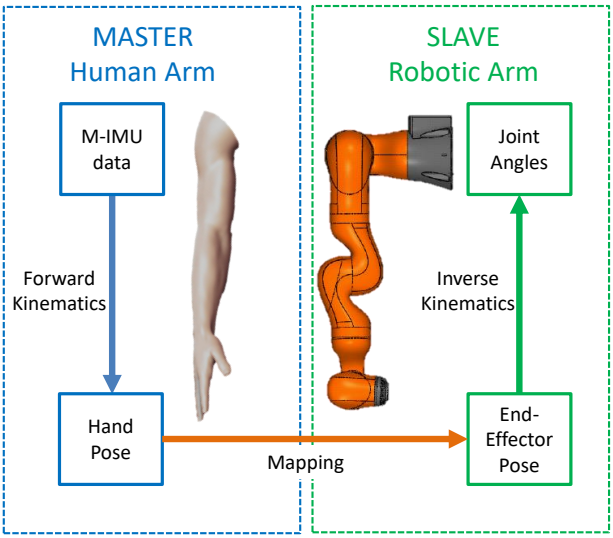

Fig. 2.1 Scheme of forward-inverse kinematics approach for human to robot motion mapping.

2.2.2 Experimental Setup

On the slave side a 7 DoFs robotic arm (i.e. the KUKA LWR4+) was used as the anthropomorphic manipulator. It is an anthropomorphic robotic arm, which communicates with a remote PC through the Fast Research Interface (FRI) Library, provided by the manufacturer. On the master side four wireless Xsens Motion Trackers were positioned on the human body in order to acquire human arm motion. MTws are magneto-inertial units and make it possible to record orientation data thanks to a Kalman Filter [28].
The four MTws were placed on the human thorax, upper arm, forearm and hand, using click-in body straps included into the Xsens kit (Fig. 2.2).

Orientation data were wireless recorded connecting the sensors to the Awinda Station. The Station was also connected through USB to an Asus PC with Ubuntu 14.04 OS. The PC established an UDP protocol based communication with the robot, through an Ethernet cable. Algorithms, both for recording MTws data and for controlling the robot, were implemented in C++ language.
The initial configuration of the human and robot arms was defined in order to obtain a robot-human joint correspondence. Hence, as shown in Figure 2.2, the robot second joint coincides with the human shoulder joint, the fourth robot joint coincides with the human elbow joint, etc. Notice that the KUKA end-effector corresponds to the human palm, in order to avoid wrist singularity. Afterwards, both robot and human frames were defined according to Denavit-Hartenberg representation.

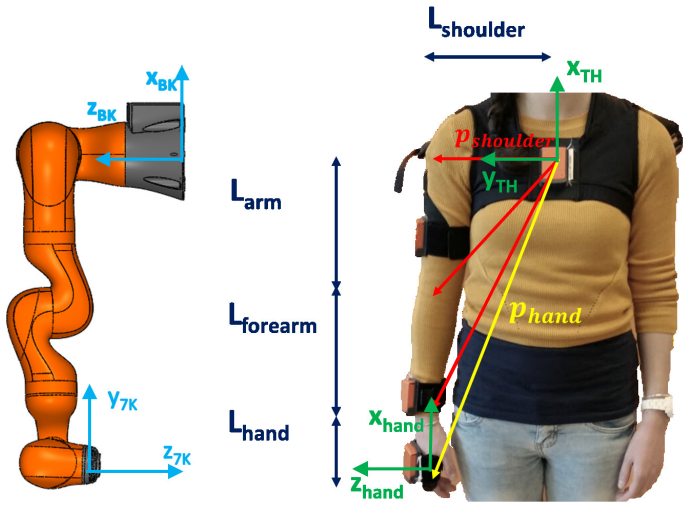

Fig. 2.2 Initial configuration of the human and robotic arms. On the left side the KUKA initial configuration with its base and end-effector reference frames is shown. On the right side the human configuration with IMUs placed on thorax, arm, forearm and hand link using click-in body straps is shown. Human thorax and hand reference frames are outlined. Hand position p_{hand} is computed as vectorial sum of each arm joint vector.

2.2.3 Forward Kinematics

Human links orientation data were recorded from MTws at 100 Hz as rotation matrices. Since the sensors were placed manually on the human arm, sensor frames turn out to be not aligned to the previously defined human frames. Therefore, a calibration procedure was executed in order to re-align these frames. The calibration provides the rotation matrix between each sensor frame and its related human link frame. The matrices are computed by processing accelerometer and gyroscope data acquired during human arm rotation around fixed axes (see [29] for details on the calibration procedure).

Afterwards, the human hand pose was computed. Assuming that the sensors were rigidly connected to the human links, each human joint position was computed as the product between the sensor frame axes aligned with the related link and the link length L_{link}. All measures were referred to the thorax reference frame R^{th0} at the time 0, with the operator in standing position (see Fig. 2.2).

Then, as shown in Fig. 2.2, the hand position p_{hand} was computed by means of a vectorial sum of human joint positions ($p_{shoulder}$, p_{elbow}, p_{wrist}), as in Eq. 2.1-2.4,

$$p^{th0}_{shoulder} = R^{th0}_{th} * v_{shoulder} \tag{2.1}$$

$$p_{elbow}^{th0} = p_{shoulder}^{th0} - R_{arm0}^{th0} * R_{arm}^{arm0} * v_{arm} \tag{2.2}$$

$$p_{wrist}^{th0} = p_{elbow}^{th0} - R_{for0}^{th0} * R_{for}^{for0} * v_{forearm} \tag{2.3}$$

$$p_{hand}^{th0} = p_{wrist^{th0}} - R_{hand0}^{th0} * R_{hand}^{hand0} * v_{hand} \tag{2.4}$$

with $v_{shoulder} = [0 \quad L_{shoulder} \quad 0]^T$, $v_{arm} = [L_{arm} \quad 0 \quad 0]^T$, $v_{for} = [L_{forearm} \quad 0 \quad 0]^T$ and $v_{hand} = [0 \quad 0 \quad L_{hand}]^T$.

R^{link0} represents each link reference frame at the starting time 0 (see Fig. 2.2). The hand orientation was basically provided by the orientation of the corresponding sensor.

$$R_{hand}^{th0} = R_{hand0}^{th0} * R_{hand}^{hand0} \tag{2.5}$$

It is worth noticing that the robot link lengths were used in liue of the human one (i.e. L_{link} in Eq. 2.1-2.4), thanks to the initial configuration previously defined (Fig. 2.2) [23]. Initially, the hand pose was referred to the thorax frame. Then, it was computed with respect to the KUKA base frame, taking into account also the rotation between the robot end-effector and the human hand frames.

$$p_{hand}^{BK} = R_{th0}^{BK} * p_{hand}^{th0} \tag{2.6}$$

$$R_{hand}^{BK} = R_{th0}^{BK} * R_{hand}^{th0} * R_{7K}^{hand} \tag{2.7}$$

Therefore, starting from the human hand pose referred to the thorax frame, the corresponding robot end effector pose with respect to the robot base frame was obtained.

2.2.4 Inverse Kinematics

In order to control the robot in the joint space taking advantage of the robot redundancy, three inverse kinematic algorithms were implemented and compared.
The DLS algorithm reduces the mean joint velocities, accepting a higher error near singular configurations. The inverse of Jacobian is replaced by a damped least squares expression (Eq. 2.8 and 2.9),

$$q(t_{k+1}) = q(t_k) + J^{DLS}(q(t_k)) * (v + Ke) * (t_{k+1} - t_k) \tag{2.8}$$

$$J^{DLS} = J^T (JJ^T + k^2 I)^{-1} \tag{2.9}$$

where $q(t_{k+1})$ represents the robot joint angles vector for a $k+1$ time sample, J is the robot Jacobian, v is the desired speed in cartesian space, K is a positive squared matrix, e represents the error between the desired and the actual pose in cartesian space, k is a damping constant and I is the identity matrix.

In the EP algorithm, the null projector is used to minimize a cost function w. For our application, this function is chosen to be an elastic potential, that represents a virtual spring connecting robot and human elbows, in order to minimize their distances. The algorithm expression is

$$q(t_{k+1}) = q(t_k) + (J^*(q(t_k)) * Ke - (I_n - J^*J)\dot{q}_0) * (t_{k+1} - t_k) \tag{2.10}$$

$$J^* = J^T (JJ^T)^{-1} \tag{2.11}$$

where I_n is a squared identity matrix of nxn dimension.

$$\dot{q}_0 = k_0 \left(\frac{\delta w(q)}{\delta q} \right)^T \quad ; \quad w = k_{elastic} \left(||p_{he} - p_{re}|| \right)^2 \tag{2.12}$$

If the robot elbow position p_{re} is the same of the human one p_{he}, the spring is at rest position, on the contrary the more is the distance between the joints, the more the spring is strained and the elastic potential is high. At the beginning, a symbolic expression of the null projector (elastic potential derivative) was computed. Then, numerical solutions were calculated for each forward kinematics output according to Equations 2.10 and 2.11.
Since the forward kinematics evaluates the desired pose at a frequency of 100 Hz, the inverse kinematics output was computed at the same frequency. Each algorithm loop was computed N times before providing output, assuming $N * t_{IK} \leq \frac{1}{100}$, with t_{IK} representing the algorithm computational time. This approach was adopted for all three algorithms.
The AJ algorithm was implemented using the swivel angle as elbow position measure [22]. This angle α represents the elbow position for fixed shoulder and hand positions (see Fig. 2.3).

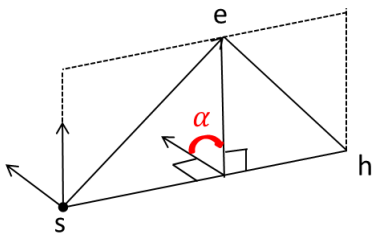

Fig. 2.3 Swivel angle (α) representing the elbow position (e) for fixed shoulder (s) and hand (h) positions.

The Augmented Jacobian J_A is computed adding to the Jacobian a row which represents the relation between the time derivative of α and the joints configuration. Also the cartesian

pose (and the related v and e values) is augmented with the additional swivel angle value.

$$q(t_{k+1}) = q(t_k) + (J_A^{-1} q(t_k) * (v + Ke)) * (t_{k+1} - t_k) \tag{2.13}$$

$$J_A^{DLS} = J_A^T (J_A J_A^T + k^2 I_n)^{-1} \tag{2.14}$$

The algorithm was implemented according to Eq. 2.13 and 2.14, where I_n is the nxn identity matrix and J_A^{-1} is replaced by J_A^{DLS} in order to avoid singularity.

2.2.5 Experimental Protocol

Four healthy subjects, 25.4 ± 1.6 years old, volunteered to participate in the study. They were asked to use the IMU sensors positioned on their body for controlling the robotic arm to reach three target positions in the robot workspace. Each task was repeated 3 times for each of the three inverse kinematic approaches (i.e. DLS, EP, AJ).
Before starting the experiments, the subjects were instructed to perform calibration movements required to reconstruct arm kinematics (see [29] for further details) and to be in standing position (see Fig. 2.2) for few seconds. Then he/she moved the arm to a comfortable configuration (i.e. with the upper arm aligned with the trunk, the elbow rotated roughly at 90 degrees and the hand palm pointing toward the chest) before starting the task, in order to let the robot move to this starting configuration. The data acquired from the IMUs were used for moving the robot arm from its initial pose to the human corresponding pose by means of a fifth order polynomial interpolation on each joint value. Then the subject started to control the robot movements for reaching the target position. During the task execution, the participants were located behind the robot in order to continuously see the robot motion.

2.3 Results

The teleoperated controls based on the previously described inverse kinematics algorithms were validated in simulation and on a real robotic arm, i.e. the KUKA LWR4+. In simulation, the inverse kinematics error was computed, obtaining values lower than one millimeter for the position and one degree for the orientation. These preliminary results showed the effectiveness of algorithm implementation.

Then, the approaches were validated on the KUKA LWR (Fig. 2.4). In order to achieve the best performance, each algorithm's gain value was empirically estimated. Performance parameters were defined as (i) the error between the human hand and the robot end-effector pose and (ii) positional error between the robot end-effector and the three targets.

For the sake of brevity, only the results obtained by one subject performing one task are shown. In particular, the error between human hand and robot end-effector position and the $SO3$ norm of the orientation error between the human hand and the robot end-effector using the three inverse kinematics approaches are shown in Figs. 2.5 and 2.6, respectively.

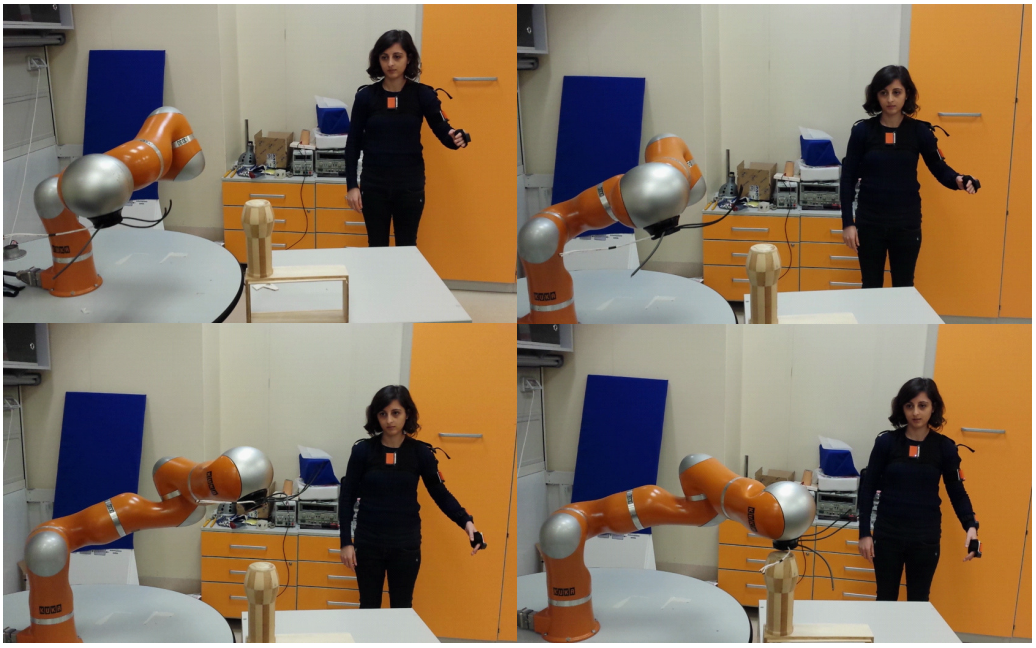

Fig. 2.4 Experimental validation on the KUKA LWR4+. Four frames of the reaching task performed by Subject 1 are shown.

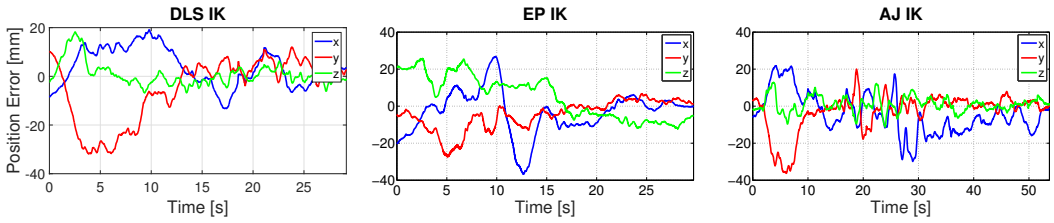

(a) (b) (c)

Fig. 2.5 Error between the human hand and the robot end-effector position using the a) DLS, b) EP and c) AJ algorithm. The values were estimated during the reaching task performed by subject 1.

The mean estimated performance value for each recruited subject are shown in table 2.1. Mean value were computed on the whole task trajectory. Additionally the positional error between end-effector and fixed target were reported as general quality indicator of task performance.

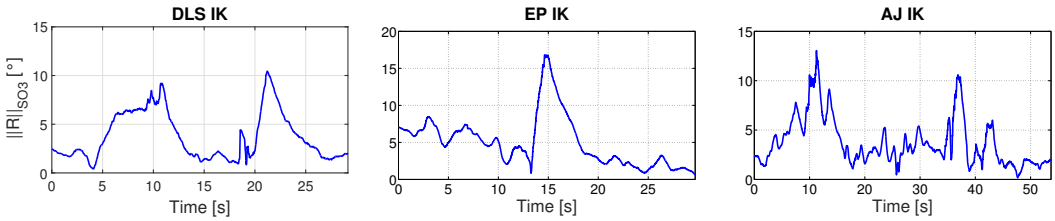

(a) (b) (c)

Fig. 2.6 *SO*3 norm of the orientation error between the human hand and the robot end-effector using the a) DLS, b) EP and c) AJ algorithm. The values were estimated during the reaching task performed by subject 1.

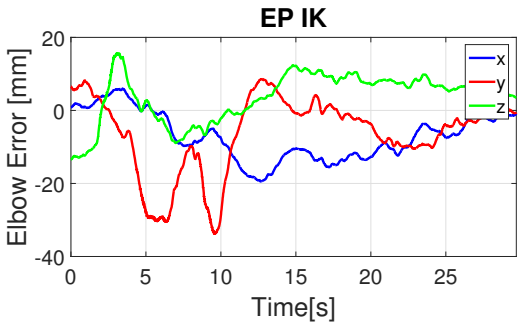

Fig. 2.7 Error between human and robot elbow position using the EP algorithm. The values were estimated during the reaching task performed by subject 1.

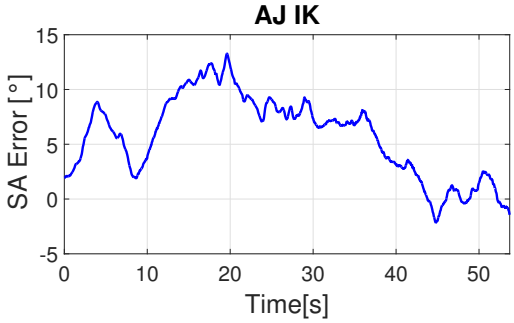

Fig. 2.8 Error between human hand and robot swivel angle using the AJ algorithm. The values were estimated during the reaching task performed by subject 1.

As evident from Figs. 2.5 and 2.6, comparable performance were obtained for the three methods, as revealed also in table 2.1.

The error between hand and end-effector pose decreases largely when the target is reached and a static pose is maintained, as we can see in the last column of table 2.1. Concerning the anthropomorphic indicators, both the swivel angle error measure and the error between the human and the robot elbows positions seem to assume high value. Nevertheless, the reason is the implementation of moderate anthropomorphic constraints instead of hard constraints, in order to achieve human-like behaviour on the slave side, preserving high accuracy on the end-effector pose (and the target reaching). The main performance dissimilarity between algorithms consists in the target reaching. Indeed, except for subject 2, the EP method showed the lowest error between the end-effector and the target positions, suggesting its easer use with respect to the other methods. On the other hand, the EP method results to have the highest error in static poses. Probably the selected gain values make this method lower accurate than the others, but overall more intuitive for subjects. A new selection of the gain values could improve the accuracy of the algorithm, preserving his usability.

It is worth noticing that the proposed approach, especially the initial configuration, is based on a robot to human joint correspondence. This implies that the robot should be installed with the base on the wall, if the subject is standing (or seated). However, we performed the task on a robot pre-installed on a table, implying some difficulties for the subjects in accomplishing the task and, therefore, decreasing their performance.

2.4 Discussion

Using human arm movements as input, and implementing anthropomorphism criteria on robot movements allowed the user to control the robotic platform more easily and intuitively than traditional master interfaces. The implemented algorithms resulted in comparable performance in terms of error between hand and end-effector pose. For instance, for subject 1, we have the following mean values:

- DLS: 12.34 ± 8.94 mm and 3.81 ± 2.76 deg
- EP: 15.64 ± 8.33 mm and 4.07 ± 2.74 deg
- JA: 11.67 ± 9.02 mm and 2.79 ± 2.12 deg

Nevertheless, the EP method showed the lower position error for targets reaching, suggesting its easier use by the subjects with respect to the other methods. On the contrary, the EP method showed also the higher static error during the last trajectory's second. Therefore

Sub	Algorithm	$\|\|PosErr\|\|$[mm]	$\|\|R\|\|_{SO3}$[deg]	$\|\|ElbowPosErr\|\|$[mm]	SA Error [deg]	$\|\|TErr\|\|$ [mm]	$\|\|SErr\|\|$ [mm] [deg]
1	DLS	12.34 ± 8.94	3.81 ± 2.76			32.15	2.49 ± 0.55 0.89 ± 0.09
	EP	15.64 ± 8.33	4.07 ± 2.74	134.33 ± 208.36		24.07	7.28 ± 0.73 1.57 ± 0.17
	AJ	11.67 ± 9.02	2.79 ± 2.12		3.38 ± 2.39	71.58	4.32 ± 0.74 1.38 ± 0.10
2	DLS	9.79 ± 8.30	3.20 ± 2.35			20.79	3.77 ± 0.43 1.80 ± 0.07
	EP	13.05 ± 10.20	3.80 ± 1.94	32.42 ± 34.65		22.88	17.24 ± 1.06 2.28 ± 0.06
	AJ	10.21 ± 8.12	3.91 ± 2.84		2.99 ± 2.18	19.99	4.2 ± 0.70 1.23 ± 0.12
3	DLS	12.37 ± 9.55	4.73 ± 2.85			48.50	6.43 ± 0.88 2.03 ± 0.26
	EP	13.89 ± 12.09	6.58 ± 3.82	140.08 ± 212.02		28.21	23.94 ± 3.61 5.84 ± 0.84
	AJ	13.92 ± 11.95	5.91 ± 2.61		3.74 ± 4.29	39.90	12.33 ± 1.73 3.69 ± 0.45
4	DLS	13.94 ± 12.68	8.33 ± 4.17			31.56	15.84 ± 1.84 5.17 ± 0.56
	EP	13.69 ± 11.40	11.47 ± 6.34	132.78 ± 208.16		25.29	21.74 ± 4.43 6.14 ± 0.56
	AJ	11.45 ± 8.64	2.15 ± 3.29		3.61 ± 8.74	35.12	7.11 ± 1.10 2.69 ± 0.39

Table 2.1 Experimental results: (i)$||PosErr||$ is the mean norm error between the human hand and the end-effector position during the whole trajectories; (ii)$||R||_{SO3}$ is the mean $SO3$ norm of the rotation matrix between the hand and end-effector in the whole trajectories; (iii)$||ElbowPosErr||$ is the mean norm positional error between human and robot elbow joints during the whole trajectories; (iv) SA Error is the mean error value between human and robot swivel angle; (v)$||TErr||$ is the mean norm positional error reaching fixed targets; (vi)$||SErr||$ is the static position and orientation error (i.e. $||PosErr||$ and $||R||_{SO3}$ values for the last trajectory second). Clearly (iii) is computed only for EP method and (iv) only for AJ method.

in the future new gain values could be selected in order to improve the EP performance, preserving its usability. Future works will be addressed to enhance the system performance by adjusting the algorithm gain values and to extend the study on a greater number of subjects. Questionnaires for assessing system usability will be also submitted to the subjects.

Chapter 3

A virtual reality platform for multisensory integration studies

This chapter presents the teleoperation of a virtual avatar, using infrared cameras and reflective passive markers, to investigate the multisensory integration of vision (or hearing) and touch. In particular the proposed platform is designed to provide the most useful stimulation and recording devices able to test different multisensory integration protocols with the same system. The platform is then validated to test the cross-modal congruency effect involved in the peripersonal space coding.

3.1 Background

Multisensory integration is an important brain function and plays a key role in understanding the brain. Cross-modal integration contributes to creating a unified and coherent representation of the environment [30] and the body; it also affects reaction behaviors [31], [32] and body ownership [33].

Renowned protocols that investigate multisensory integration are: the rubber hand illusion, the motor hand illusion, the visuo-tactile interference, etc. [34], [35]. Although those protocols investigate similar underlying process, they present very different setups and most of them requires the experimenter to manually provide stimulations. Only recently, engineers contributed to develop more accurate and automated setups [36] to improve accuracy and repeatability of the experimental paradigms.

Is it possible to have only one setup useful in any kind of multisensory integration studies? What do they have in common? The key factor seems to be the spatial-temporal coherence between the stimuli, which strongly affects the efficacy of multisensory integration (let's

think of the rubber hand illusion which does not occur if the visual and tactile stimuli are asynchronous) [37].

The key idea is to design a multi-purpose platform, exploitable in a wide range of cross-modal integration studies. We validated the platform on two healthy participants, implementing a visuo-tactile integration task to investigate the peripersonal space (PPS).
PPS can be defined as the human body field of action [38]; the human brain can differentiate between the space close to the body (PPS) and the far one, depending on the potential interaction with objects, i.e. reaching or grasping [39], [40], [41]. For example, the visual receptive field of neurons located in the ventral intraparietal cortex is linked to the arm's tactile receptive field [42]. Those neurons code the peripersonal space integrating tactile and visual (or auditory) stimuli that occur close to the arm [43], [42], [44].
Thus, the reaction time -in response to a tactile stimulus on the hand- decreases the more a simultaneous visual (or auditory) stimulus is presented near the hand [45], [46], [47].

We aim to develop a single platform able to collect and quantify all those factors; a virtual reality platform that provides synchronous stimuli, acquires behaviour reactions and measures critical features (such as reaction times and the hand and stimulus positions) both in static and dynamic tasks.
Virtual reality that exploits immersive technologies such as headsets, allows to easily test and manipulate several conditions and features, thus granting the opportunity to delve deeper into brain plasticity and embodiment [32], [33]. The use of virtual reality is legitimated by the occurrence of cross-modal effects even using an object that mimics the appearance of a real hand (e.g. a rubber hand) [33].
The platform also includes a motion tracking system, which allows the real-time tracking of the human arm movement and the active control of virtual avatars and objects, possibly improving the embodiment and the agency.

3.2 Materials and Methods

3.2.1 Platform Design and Features

A custom software was developed to manage all the platform elements and their synchronization. The application includes a user-friendly interface to set the stimulus parameters: type, amplitude, position, duration, etc.
To make the virtual environment as immersive as possible, the avatar is presented in first-person perspective and animated by the participant's movement (see Fig. 3.1). If required, the platform allows to select also a back-view and a mirrored perspective.

The VR headset, used to best exploit the first person perspective, can also be used to track the head movement and the gaze.
In the user interface the avatar height, as well as the gender, can be adjusted to match the limbs' length and the point of view of the participant.

Four infrared cameras, fixed on a structure surrounding the experimental area, track the participant's motion through reflective passive markers attached to 3D printed rigid bodies. The motion tracking has a twofold role: i) mapping the human motion on the virtual avatar, thus improving the VR vividness and the embodiment; ii) measuring in real-time the human arms position with respect to the stimuli, to the environment and to his own thorax and head.

The rigid bodies fixed on the thorax, arms, forearms and hands allow to track the upper limb and thorax motion. In the present case only three rigid-bodies were used to track the right arm. As depicted in Fig. 3.2a, they were placed on the human links, far from the muscles to avoid jerky movements due to muscle contractions.

Since the implemented protocol (see section 3.2.2) assumes a unique position for the participant in the experimental setup, a fixed reference system was employed. The orientation of each human link was computed with respect to the base reference frame of the experimental setup (ES) and then mapped into the not left-handed virtual reality coordinate system (VR), according to:

$$^{VR}q = [^{ES}q_z, ^{ES}q_y, ^{ES}q_x, -^{ES}q_w]^T \tag{3.1}$$

where q is a unit quaternion represented by three vectorial (x, y and z) and a scalar (w) component as $q = [q_x, q_y, q_z, q_w]^T$. This mapping requires an initial alignment between the experimental reference frame and the experimental setup, i.e. the table and the chair in this case (see section 3.2.3).
The developed software allows to skip this step, taking as reference frame $ES0 = arm0 = for0 = hand0$ a starting known pose, i.e. the T pose (see Fig. 3.2a). The orientation of each link is computed according to the following equations:

$$\begin{cases} ^{arm0}q_{arm} = ^{b}q_{arm0}^{-1} * ^{b}q_{arm}; \\ ^{arm}q_{for} = ^{arm0}q_{arm}^{-1} * (^{b}q_{for0}^{-1} * ^{b}q_{for}); \\ ^{for}q_{hand} = ^{arm}q_{for}^{-1} * ^{arm0}q_{arm}^{-1} * (^{b}q_{hand0}^{-1} * ^{b}q_{hand}); \end{cases} \tag{3.2}$$

where arm, for and $hand$ refer to the arm, forearm and hand links respectively; b is the unknown base frame; $^{b}q_{link0}$ is the orientation of the link acquired at time 0, with the participant in the T pose (see Fig. 3.2a); q^{-1} is the inverse quaternion. Once the orientation of each link with respect to the previous one and to the initial pose is computed, as in Eq. 3.2, each quaternion is converted according to Eq. 3.1.

The participant's response was recorded using a keypad. The tactile stimulation was provided through an electric stimulator, controlled through serial communication by the main software developed to manage also the virtual environment and the motion tracking.

The visual stimulus was presented as a red light with a semi-sphere shape, similar to a led (see Fig. 3.1), that appears on the virtual table surface and lasts for 100 milliseconds. The led position was randomly selected according to the following criteria:

- the stimulus is provided only in the right hemispace (with respect to the participant/avatar's thorax)
- the stimulus distance from the hand is randomly selected within an adjustable range
- the stimulus never appears on the hand nor the arm (i.e. the light direction is included in the $-45 \div 225$ deg range, considering the hand as the center of a reference system as shown in Fig. 3.2b).

Since the horizontal plane is represented by the xz plane in the VR environment (see Fig. 3.2a), let us consider the virtual table plane as the xz plane of a reference system. Thus, the above criteria led to the following equations:

$$x_{led} = x_{hand} + r\cos\alpha \tag{3.3}$$

$$z_{led} = z_{hand} + r\sin\alpha \tag{3.4}$$

with $\alpha = -45 \div 225\,\text{deg}$ and $r = d_{min} \div d_{max}$, being d_{min} and d_{max} the minimum and maximum led-hand distances computed as the cartesian norm (see Fig. 3.2b).

3.2.2 Experimental Protocol

We asked the participant to react as fast as possible to a tactile stimulus provided on his right index, regardless to eventual visual stimuli.
The protocol starts with a familiarization phase where the participant, in first-person perspective, moves his arm to control the virtual one in a simple reaching task. This goal-oriented task could improve the agency and the embodiment of the virtual arm, in addition to let the participant become familiar with the VR environment. A cross in the centre of the virtual table helps the participant to fix his gaze on the same point during the whole experiment.

The familiarization is followed by four sessions of fifty trials each. A single trial consists in the presentation of a stimulus condition, that can be:

- V: visual stimulus only

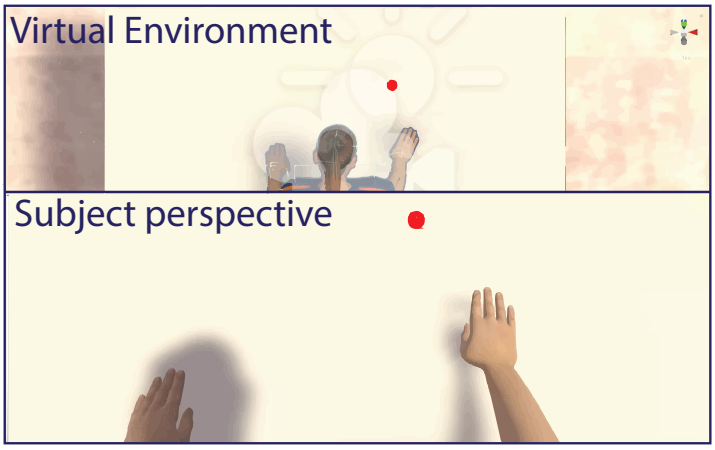

Fig. 3.1 TOP: Virtual environment with the avatar seated on a chair and the arms placed on the table. The left arm is still, whereas the right arm motion is controlled by the participant's arm. The red led appears in the right hemispace. BOTTOM: Virtual environment from the participant's point of view (first-person perspective).

- T: tactile stimulus only
- VT: visual and tactile simultaneous stimuli

The first two are control conditions to ensure that the participant is reacting to the tactile stimuli only and not to whatever stimulus he perceives.
In this pilot test each session was composed of eight T conditions, eight V conditions and thirty-four VT conditions. The protocol was tested two times: the first time with the right hand always in the same position (hereafter called "single pose" condition); the second time asking the participant to change his hand position, always in the right hemispace, ten times during each session ("multiple poses" condition). In the "multiple poses" condition, the stimulation was delivered when the hand was still, i.e. in static states.
The "multiple poses" condition was included to deeper investigate if and how the position of the hand affects the cross-modal congruency effect, being the hand the supposed center of the peripersonal space.

3.2.3 Experimental Setup

The experimental setup was composed of a table and a chair (both duplicated in the virtual environment) placed into a structure with the four Prime Optitrack cameras fixed on. The participant was seated on the chair, wearing the HTC Vive headset, with the hands and forearms placed on the table in a comfort position (see Fig. 3.3), and the left index placed in correspondence to the keypad.

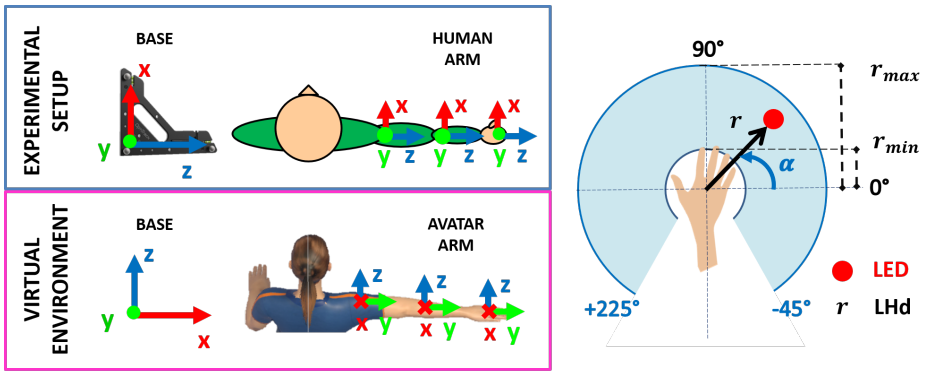

a) b)

Fig. 3.2 a) Scheme of the motion mapping between the human arm link orientation, defined in the experimental base reference frame, and the virtual avatar arm defined with respect to the not left handed base frame in the virtual environment; b) Scheme of the visual stimuli workspace. The blue area is the region where the red led can appear and it is limited by a led-hand distance (LHd) $r = r_{min} \div r_{max}$ in a direction defined by an angle α in the range $-45 \div 225$ deg with respect to the hand. The workspace is also limited to the right hemispace with respect to the participant/avatar's thorax.

The main application was developed in C# language using the Unity3D environment. A dedicated electronic board sent the input to the electric stimulator (Grass Astro-Med S88x stimulator), which provided the tactile stimulation through two electrodes placed on the right index. The electric stimulation intensity was set to the minimum one clearly perceivable by the participant.

The signal used for the motion tracking was acquired using the software Motive and the provided Unity plugin. The developed VR application was set with a hand-led distance in the range $8 \div 30cm$ (i.e. $r_{min} \div r_{max}$ in Fig. 3.2b).

The following measures were computed from the recorded data:

- RT: reaction time computed as the time between the tactile stimulus and the participant's response (keypad button pressed)
- LHd: led-hand distance computed as the cartesian norm in the xz plane (i.e. the horizontal plane in the VR environment) between the led and the hand.
- LAd: led-avatar distance computed as the cartesian norm in the xz plane (i.e. the horizontal plane in the VR environment) between the led and the thorax.

Two participants not aware of the aim of the study were enrolled to test the proposed protocol. They were healthy and reported to have normal vision and proprioceptive sensations; they provided written informed consent in accordance with the declaration of Helsinki and to the Ethical Committee of the Università Campus Bio-Medico di Roma.

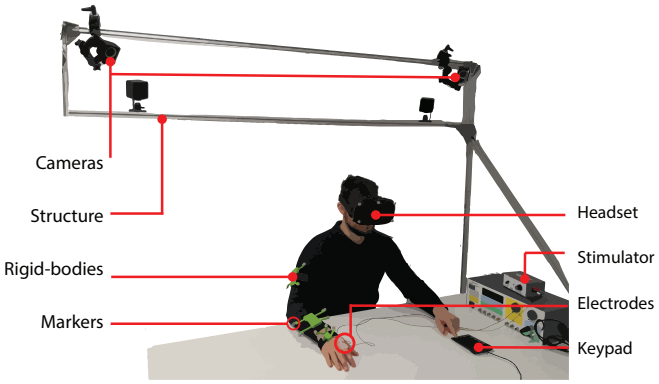

Fig. 3.3 Experimental setup. The participant is seated on a chair, wearing the VR headset. Three rigid-bodies 3D printed are placed on his right arm, forearm and hand. Each rigid-body is equipped with four reflective passive markers to be tracked by the infrared cameras placed on the structure surrounding the table. The tactile stimulus is provided by the stimulator through two electrodes placed on the participant's right index. The response is acquired by means of a keypad, pressed with the left index.

3.2.4 Data Analysis

Data were analysed in Matlab 2017, removing the outliers meant as values outside the range $m \pm 2sd$, with m representing the mean value and sd the standard deviation. The statistics software JASP was used to analyse how the reaction time is affected by the presence of visual stimuli and their position with respect to the participant's hand or thorax (LHd, LAd).
The analysis took into account the VT trials, for both the "single pose" condition and "multiple poses" condition.

3.3 Results

Fig. 3.4 shows the results of the correlation analysis (Pearson's coefficient) between the led distance from the hand or avatar and participants' reaction times (RT). The two rows correspond to the two participants S1 and S2. The left block (first two columns) represents the "single pose" condition, whereas the right block (third and fourth columns) is related to the "multiple poses" condition. It is worth noting that the stimuli administration and the RT recording occurred in static conditions (with the hand still). In the first column of each block the correlation between the RT and the led-hand distance (LHd) is depicted, whereas the second column shows the correlation between the RT and the distance between the led and the avatar thorax (LAd). The analysis revealed a significant correlation (rho=0.203; p=0.013) between led-hand distance and reaction times in the "single pose" condition for participant one. The second participant shows the same trend, even if not significant.

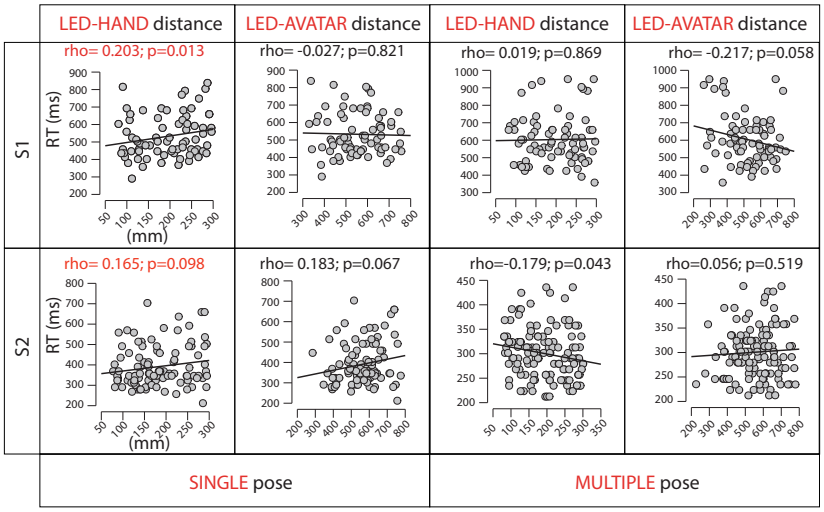

Fig. 3.4 Correlations between the distance of the LED (from hand or avatar) expressed in millimetres and reaction times (RT) expressed in milliseconds, for participant S1 and S2.

No other significant correlations were found, except for the LHd in the “multiple poses" condition of the second participant.

3.4 Discussion

The presented platform let us disentangle and study the specific contributions of features that play a role in cross-modal integration studies: stimulus type, duration and distance from participants body; arm position, orientation and appearance; participant’s gaze; etc..
During the validation on a peripersonal space protocol, we found a correlation between the participant’s hand distance from a visual stimulus and reaction times: the closer the visual stimulus is presented to the participant’s hand, the “faster" he responds to that stimulus. Even though the correlation coefficient is rather low (rho=0.203), the trend is coherent with expected results, based on existing literature [46]. The absence of a correlation between reaction times and led-avatar distance also confirms the previous finding on the arm-centred nature of the peripersonal space [42].
We should deeper investigate the “multiple pose" condition, enrolling more participants, to clarify how the hand movement affects the peripersonal space representation.

Summing up, the main advantage of the proposed platform is the possibility to use a single system for a great variety of experiments, real-time recording a huge set of quantitative measures, thus having the chance to deeply study the brain plasticity and the related features.

Future perspective consists in employing the platform in many additional studies, investigating how the cross-modal congruency affects the body schema representation, the embodiment of external objects, the space representation and behaviour reactions.

Chapter 4

Development and validation of a novel calibration methodology and control approach for robot-aided Transcranial Magnetic Stimulation (TMS)

This chapter presents the development of a robotic platform to substitute human operators in administering TMS. Together with the implementation of the system and its control approach, the author presents also an optimization method to reduce calibration errors in robot-aided TMS systems. On one hand the platform represents an extreme case of human substitution; on the other hand it its a useful tool to improve and automatize the brain stimulation, allowing also to increase the knowledge of the brain mechanisms involved in the embodiment.

4.1 Background

The last decades have seen an increasing use of Transcranial Magnetic Stimulation (TMS) to investigate and modulate human brain functions. TMS is a non-invasive and painless technique used to elicit a local stimulation in the cerebral cortex, through an electromagnetic field generated by a coil placed upon the scalp [48], [6]. Depending on the coil shape (e.g. figure of eight or circular), it can stimulate wider or more focal cortical surfaces [49], and it is used for both clinical assessment and research purposes [50], [51]. Usually the TMS is carried out manually by an expert operator who holds the coil on the subject's head [52]. However, the coil position and orientation above the scalp hugely affect the intensity and the location of the induced current inside the stimulated area [53], [54], [55].

Many efforts have been made to improve the coil positioning, through the employment of neuronavigation systems that guide the operator in placing the coil over the scalp [56]. These neuronavigators are typically made of a stereotaxic system combined with a software for the estimation of 3D models of the scalp and the brain, based on the correlation of the geometrical data of the scalp with average or personal Magnetic Resonance Images. [57]. Despite the introduction of the neuronavigation, accuracy and reliability of the coil positioning are still strongly dependent on the operator skills [58]. Very recently, robot-aided TMS systems have been proposed to improve the accuracy and the repeatability of coil positioning, and to make the procedure more comfortable for both the participant and the operator, while potentially reducing the duration of the experimental session [59], [60], [61], [62], [63], [64]. Although a few systems for robot-aided TMS have been proposed [65], [66], [67], the research on robotic platforms for TMS is still an open topic to be investigated. In particular the few devices commercially available are much expensive and do not allow to implement custom protocols; standard procedure both for the calibration and the stimulation of robotic TMS platforms are missing, making harder the comparison of results from different studies; control strategies proposed so far often use force or hybrid control, linked to stability and safety issues that affect the safety as well as the robot performance in compensating the head movements.

The study presented in this chapter aims to develop and validate a new robot-aided TMS system, characterized by a new control approach and to propose a calibration procedure tailored on the specific application. The robot-aided TMS platform is based on the integration of a 7 degrees of freedom (dof) robotic manipulator and a stereotaxic neuronavigation system. The control approach is based on impedance control, which guarantees to achieve both high coil positioning accuracy and high safety of interaction.

The innovative approach relies on an ad-hoc method for system calibration, needed to align the data coming from the neuronavigation system to the robot base reference frame.

In robotics the calibration between a camera-based system and a robotic manipulator is a well-known problem, called tool-flange and robot-world calibration [68], [69], [70],[71], [72], [73], [74]. From a mathematical point of view, the problem can be solved by finding a solution to a matrix equation of the type $MX = YN$, where all the matrices are 4x4 homogeneous transformations in the SE(3) space. In particular, M represents the robot end-effector pose expressed in the robot base frame, N is the coil pose expressed in the camera base frame, and X and Y are two unknown transformations between the end-effector and the coil frames, and the robot and camera base frames respectively [75], [76], [77].

Several approaches are effective to solve it for general robotic applications, but none of them takes into account the constraints imposed by our specific target application, i.e. the TMS

(e.g. the specific shape and the limited dimension of the useful workspace) [78], [79], [80]. Conversely, the calibration strategy we developed is specifically devised for TMS application, by constraining the calibration points inside the useful TMS workspace. To validate the novel strategy, we tested three calibration algorithms proposed in literature in different contexts (e.g. aerial vehicle applications, etc.) [75], [76], [80].
The developed system, employing the novel control approach, was then validated in real TMS sessions on healthy subjects, assessing its performance in term of position and orientation error positioning the coil and the amplitude of the elicited Motor Evoked Potentials (MEPs) [81].

4.2 Materials and Methods

4.2.1 Problem statement

Robot-aided TMS platforms can be either ad-hoc designed or devised integrating built devices in a unique system; typically, the integration is made of: robotic manipulator, neuronavigation software with a stereotaxic system, TMS stimulator with coil and a workstation (Fig. 4.1). The aim of a robot-aided TMS platform is to hold and move the coil on the subject's head, compensating for her/his movements to keep the stimulation point constant, with the correct coil orientation. To achieve this objective, we need to address two problems: i) calibrating the camera-based neuronavigation system (the gold standard to identify the stimulation point and to monitor the coil position so far) and the robot to obtain a common reference system; ii) controlling the robot to follow the stimulation point on the scalp, while guaranteeing subjects safety.

4.2.1.1 Hand-eye and robot-world calibration

The calibration of the robot-aided TMS system, composed of a robot holding the coil and a stereotaxic system for neuronavigation, can be addressed as a two-frame sensor calibration problem, also called hand-eye and robot-world calibration. The hand-eye and robot-world calibration results in a single reference system for all the devices integrated in the platform (i.e. robot, coil and camera). Thus, it allows to control the robot even when the coil is not visible by the camera: for example, when the target is located in posterior areas. The main disadvantage is the need to keep the camera and robot base fixed, conversely to alternative approaches (i.e. the one employed by Axilum) that simultaneously neuronavigate all the items, with the possibility to move the system's elements without affecting the control. We selected the first approach to achieve better online control performance; the need to keep

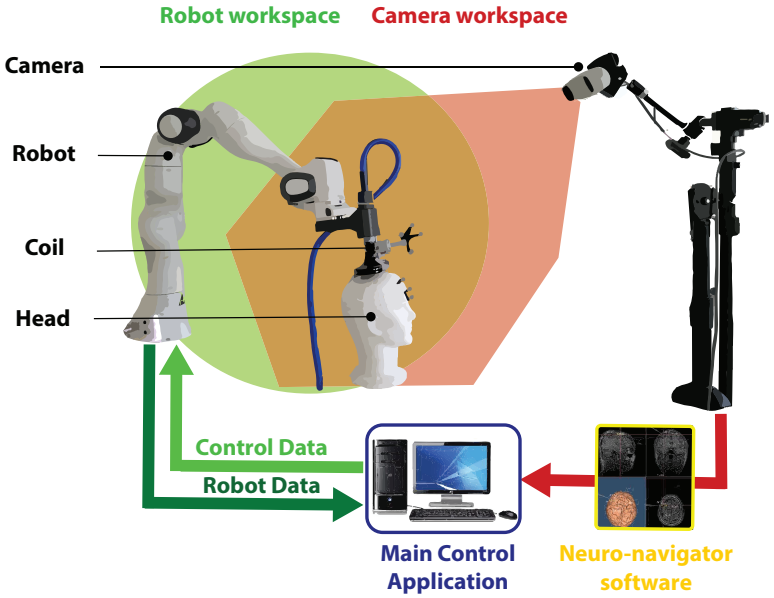

Fig. 4.1 Scheme of the proposed robot-aided TMS system: on the left side the robot holds and moves the attached coil on the subject's head; the head and the coil are tracked by the camera thanks to the markers placed on them. On the right side the camera is placed so that its volume of capture overlaps the robot workspace. In the center, the main control application receives data from the robot and from the camera, through the neuronavigation software, and sends to the robot the computed motor commands, to keep the coil in the right pose with respect to the head, according to the stimulation point set in the neuronavigator.

the items fixed is negligible since the robot base is usually already fixed and, thanks to the possibility to control the system even with the coil not visible, the camera movement is unnecessary during the stimulation session.

Referring to Fig. 4.2, the equation relating the coil pose measured in camera frame (${}^{bC}T_c$) and the robot end-effector pose measured in robot frame (${}^{bR}T_{EE}$), can be expressed as:

$$ {}^{bR}T_{EE}\,{}^{EE}T_c = {}^{bR}T_{bC}\,{}^{bC}T_c \tag{4.1} $$

and it could be generalized in the aforementioned equation $MX = YN$, where M represents the end-effector pose with respect to the base frame (${}^{bR}T_{EE}$); X is the transformation ${}^{EE}T_c$ between the robot end-effector and the attached coil reference frames; Y represents the transformation ${}^{bR}T_{bC}$ between the robot base and camera base reference frames; N is the coil pose expressed with respect to the camera base frame (${}^{bC}T_c$). All the aforementioned matrices are 4x4 homogeneous transformation matrices in the SE(3) space. Solving that problem means to compute the unknown transformation matrices X and Y.

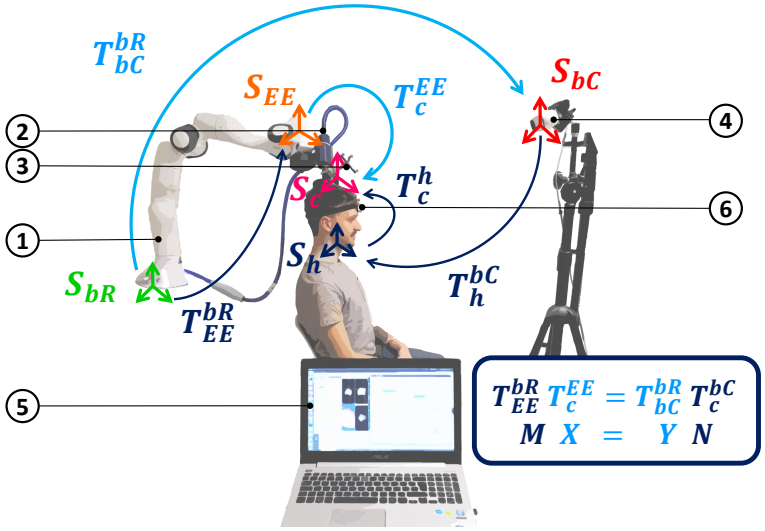

Fig. 4.2 Experimental setup and scheme of the system reference frames: on the left side the Panda robot (1) with the 3D printed flange and the coil (2) attached and connected to the *coil* item (3); on the right side the Polaris Vicra camera (4). The camera and the robot are connected to a PC (5) through an USB and an Ethernet cable, respectively. Subject's head (6) with the *head reference* item attached and visible to the camera allows the SofTaxic Optic software to work. S_{bR}, S_{EE}, S_c, S_h and S_{bC} are the reference frames of the robot base, end-effector, coil, head and camera base, respectively. ${}^jT_i$ is a 4x4 homogeneous transformation matrix between the j and i reference frames. The equation representing the system could be synthetically expressed as an hand-eye and robot-world calibration problem: $MX = YN$.

4.2.1.2 Robot control

Regarding the robotic platform (scheme in Fig. 4.1), once the stimulation point is selected, the aim of the control is to move the coil keeping it on the target regardless to possible head movements, which means to keep the coil pose constant with respect to the head. The constant relative pose between head and coil in the target is mathematically defined as:

$$ {}^hT_c|_{target} = const \tag{4.2}$$

where T is a 4x4 homogeneous transformation in the SE(3) space between the head (h) and the coil (c) reference frames (see Fig. 4.2). To make the stimulation effective, the coil should be always tangent to the scalp upon the stimulation point [54], [82]. Moreover, the control approach needs to employ several constraints to guarantee the subject safety, e.g. to keep the contact force under the safety threshold [83].

4.2.2 Calibration Algorithms

A typical approach to solve the hand-eye and robot-world calibration problem is a mathematical regression to find the unknown homogeneous transformation matrices X and Y that best fit a set of equations of the type

$$M_i X = Y N_i \quad i = 1, ..., n. \tag{4.3}$$

acquired moving the robot with the attached coil on n different poses. We implemented and tested three algorithms -hereafter briefly described- available in literature to solve a similar problem in different contexts.

4.2.2.1 Stochastic Global Optimization (*SGO*)

The Stochastic Global Optimization (*SGO*) method [75], is a two-phase stochastic geometric optimization algorithm, based on the minimization of the last-squares criterion

$$\frac{1}{2}\sum_{i=1}^{n} \|M_i X - Y N_i\|^2, \tag{4.4}$$

where the $\|\cdot\|^2$ is defined as $\|P-Q\|^2 = \|R_P - R_Q\|_F^2 + \zeta \|p_P - p_Q\|_C^2$. $P, Q \in SE(3)$ are 4x4 homogeneous transformation matrices, $R_P, R_Q \in SO(3)$ are the rotation matrices representing the rotation part of P, Q and $p_P, p_Q \in \mathbb{R}^3$ are the translations of the same transformations; the $\|\cdot\|_F$ is the Frobenius norm, $\|\cdot\|_C$ is the Cartesian norm, and $\zeta \in \mathbb{R}_+$ is a weighting factor for the translation component.

This method aim This approach allows the localization of the optimal local minimum, achieving the best performance with noisy data. More details on implementation and characteristics of the *SGO* method can be found elsewhere [75].

4.2.2.2 Non-Orthogonal Method (*QR24*)

The *QR24* method, based on a least-squares approach, let us to simultaneously compute the rotational and translational part, allowing for non-orthogonal calibration matrices in order to deal with real-world localization devices and imperfect robots [80]. Expressing the equation (4.3) as a system of linear equations:

$$A_i w = b_i, \quad i = 1, ...n. \tag{4.5}$$

with $A_i \in \mathbb{R}^{12nX24}$, $b_i \in \mathbb{R}^{12n}$ and $w \in \mathbb{R}^{24}$ composed of the non-trivial elements of X, Y, M and N, the aforementioned system (eq. (4.5)) is solved minimizing the Frobenius

norm, through a least-squares approach by means of QR-factorization. Because of the adopted approach and the number of unknown variables that have to be estimated, the method is also called *QR24 calibration algorithm*. Details on how to transform the eq. (4.3) into the system of equations in (4.5) are described in [80].

4.2.2.3 Quaternion approach (*QUAT*)

The quaternion approach addresses the problem decomposing the Eq. (4.3) in the rotation and position equations as follows:

$$R_M \cdot R_X = R_Y \cdot R_N \tag{4.6}$$

$$R_M \cdot t_X + t_M = R_Y \cdot t_N + t_Y \tag{4.7}$$

where R_j is the 3x3 rotation matrix and t_j is the 3x1 translational vector of the j_{th} 4x4 homogeneous transformation matrix. Since Eq. (4.6) could be expressed in a unit quaternion form

$$q_M * q_X = q_Y * q_N, \tag{4.8}$$

this method attempts to simultaneously solve for the rotation and translation parts through a Levenberg-Marquardt nonlinear constrained minimization. The error function to minimize is:

$$\begin{aligned} f(R_X, R_Y, t_X, t_Y) = \mu_1 \sum_{i=1}^{n} \|R_{Mi} R_X - R_{Ni} R_Y\|^2 \\ + \mu_2 \sum_{i=1}^{n} \|R_{Mi} t_X + t_{Mi} - R_Y t_{Ni} - t_Y\|^2 \\ + \mu_3 \|R_X R_X^T - I\|^2 + \mu_4 \|R_Y R_Y^T - I\|^2 \end{aligned} \tag{4.9}$$

where the four μ are real positive weight coefficients and $\|.\|^2$ is an Euclidean norm. The last two terms of the equation represent the constraint for R_X and R_Y to be rotation matrices, i.e. matrices that verify $RR^T = I$, with I identity matrix. Deeper details on the implementation and features of the quaternion approach can be found in [76].

4.2.3 Selection of the Useful Workspace

Although some of those calibration methods have been employed in robotic TMS systems, no specific constraints have been set for their application, which is quite different from other generic robotic tasks.

Typically, in a TMS session, the subject is asked to stay still. Even though the use of a robot allows for small head movements, thanks to the motion compensation, they are still limited. Indeed, the subject is usually sat in the back seat, thus the possible movements are small rotation of the head and limited displacements of the neck. Furthermore, the coil is always placed over the scalp, thus we can assume that the effective workspace of robot movements for this specific application is restricted to a head-centered spherical shell (see Fig. 4.3a). Usually the calibration is performed moving the robot on different equally spaced-out points in a cube or a sphere, involving the specific workspace [80], [84].
The spherical shell constituting the useful TMS workspace can be identified as the volume between two concentric semi-spheres with radii of 0.1 m and 0.15 m (see Fig. 4.3c). These dimensions derive from the average size of the human head and its possible movements during the TMS [85], [86], [87]. On the other hand, a typical calibration workspace in a general application is the volume of an entire sphere with radius of 0.2 m [69], [80].

Thus, as shown in Fig. 4.3b, seven concentric spheres with radii varying between 0.05 m and 0.2 m, with 500 equally spaced-out points on each surface, were identified to create a discrete representation of the two workspaces (i.e. the entire sphere and the spherical shell). Among this pool of data, three datasets were selected:

1) Dataset for calibration in the entire sphere;

2) Dataset for calibration in the spherical shell;

3) Dataset for error assessment.

Each dataset was composed of 250 points randomly picked in the above mentioned pool of predefined points, considering only those into the spherical shell for the second and third dataset (i.e. for the assessment we only considered those points in the useful TMS workspace, since for this specific application a good accuracy is required only in that region). In particular, the first and second group of data were used to perform the calibration considering the two different workspaces, while the third set was used to assess the calibration performance. Each dataset was different from the others, being the points randomly selected. We tested our proposed methodology with the three different calibration algorithms presented in section 4.2.2, assessing the performance on the third dataset, in term of position and orientation error and duration. Thus, the overall dataset, acquired using the described platform, is composed by 3500 points, 500 on each sphere surface. Among this pool of data, the above mentioned 3 datasets were selected by randomly picking the points 5 times. The three algorithms were tested on the same data, with the translational part represented in meter, without using scaling factors. Preliminary tests were conducted to select the best

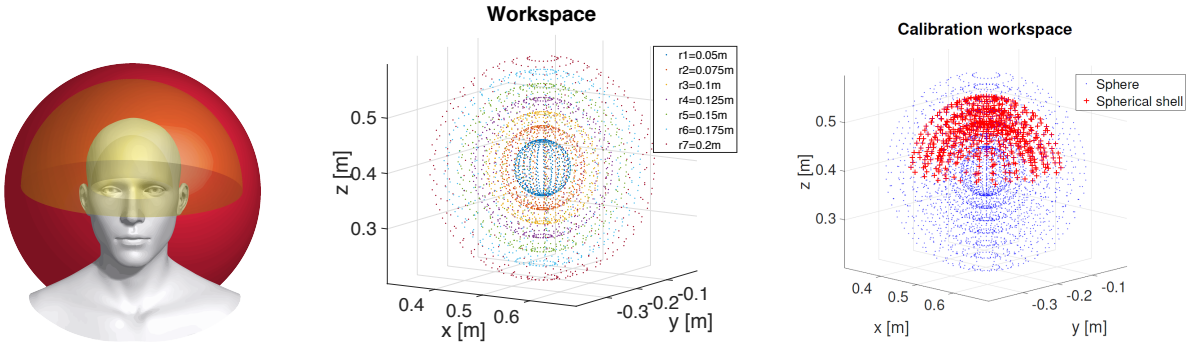

(a) (b) (c)

Fig. 4.3 (a) Sphere workspace concentric to the head, with in yellow the spherical shell useful to the TMS, that takes into account physiological head movements. The bottom and inner parts of the sphere (in red) are excluded. (b) Seven concentric spheres with radii varying from r1=0.05 m and r7=0.2 m with 500 equally spaced-out points selected per sphere surface. All measures are referred to the robot base reference frame. (c) In red the 250 points that belong to the useful TMS workspace (spherical shell), picked among the entire sphere dataset (in blue). Coordinates are referred to the robot base reference frame.

weight coefficients (i.e. unitary values). Also, the same approach was implemented to assess the calibration errors for all the algorithms. Referring to Eq. (4.3), the 4x4 homogeneous transformation matrix $E = (M_i X)^{-1} Y N_i, i = 1,...,m$ was computed. From this matrix the position and orientation errors were obtained as the average of the norm of the E translational part and of the norm in the $SO(3)$ space of the E rotational part, respectively.

4.2.4 Robot-aided TMS: platform and control approach

The developed robot-aided TMS platform (Fig. 4.1) is composed of a 7 dof robotic manipulator (Panda by Franka Emika GmbH), a Polaris Vicra infrared camera (by Northern Digital Inc.) and the SofTaxic Optic neuronavigation software (by E.M.S. srl).

The robot holds and moves the coil, which is attached to its end-effector by a custom-designed and 3D printed flange. Since the coil cable is usually heavy and it can affect the contact force estimation as well as the center of mass and the gravity compensation of the flange-coil system, we designed the flange to fix the coil cable on its side; then we estimated the coil-flange inertial parameters to set the payload of the robot. This solution allowed to avoid artifact perturbation in the contact force due to the coil cable, at least for stimulation protocols limited in one hemisphere. In case of protocols covering the whole scalp (i.e. extended cortical mapping) the force artifacts due to the cable could not be completely removed, but they still remain negligible with respect to the flange-coil contribute.

An infrared camera is placed in front of the robot and it is positioned in order to maximize the

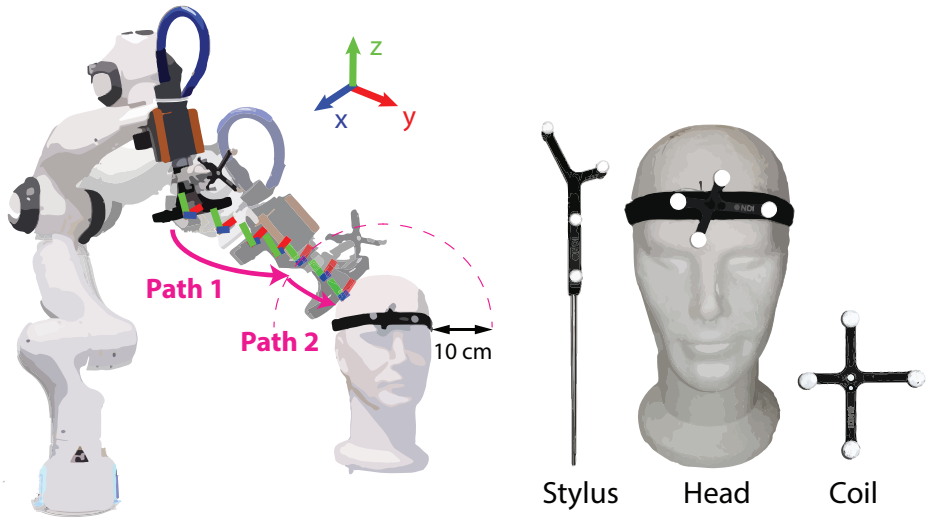

(a) (b)

Fig. 4.4 (a) The robot moves on the stimulation point following a minimum jerk trajectory split in 2 paths: 1) to reach, with the right orientation, the point 10 cm above the scalp; 2) to slowly move on the head. The coil reference frame trajectory is highlighted on the two paths. (b) Marker items equipped with four passive reflective markers: *stylus item* used to point the scalp points and reconstruct the head 3D model; *head item* attached on a velcro band to be fixed on the subject's forehead, *coil item*.

overlap between its working volume and the robot workspace. Two sets of passive reflective markers are fixed on the handle of the coil and on the subject's head (using a headband), in order to allow the camera to track both head and coil pose during the TMS procedure.

The data streamed from the camera (i.e. the coil and head positions and orientations) are directly received by the neuronavigator, which reconstructs the 3D model of the subject's scalp and brain, in order to select the stimulation point that allows to elicit a stimulation of a specific cortical area [88].

The main control application processes both the data acquired from the camera through the neuronavigator, and the data recorded from the robot sensors; then the application sends commands to the robot motors in order to keep the coil on the selected stimulation point.

Once the stimulation point is selected, the robot is controlled to move and hold the coil on the target according to the head pose tracked by the camera, keeping the transformation between the head and the coil constant (Eq. 4.2). Once the system is calibrated, the coil pose is directly acquired through the robot data regardless of the coil pose measured by the cameras. Indeed, since the coil is rigidly linked to the robot end-effector, and the end-effector pose referred to the robot base frame is computed using the forward kinematics, we can derive the coil pose even when the coil markers are not visible by the camera, as it could happen when stimulating posterior brain areas.

Adopting that solution, the equation (4.2) is expanded as follows:

$$ {}^{h}T_c|_{target} = {}^{h}T_{bC}\,{}^{bC}T_{bR}\,{}^{bR}T_{EE}\,{}^{EE}T_c = const \tag{4.10} $$

where ${}^{h}T_{bC}$ is the transformation between the head and the camera base frame (bC), recorded by the camera-based tracking system; ${}^{bC}T_{bR}$ and ${}^{EE}T_c$ are the two constant calibration matrices representing the robot base frame (bR) with respect to the camera base frame, and the coil pose with respect to the end-effector (EE) reference frame, respectively; ${}^{bR}T_{EE}$ is the end-effector pose with respect to the robot base frame that can be modified by the robot controller.

In order to set the target position for the robot controller (${}^{bR}T_{EE}|_{target}$), the following constant transformations, obtained through the calibration, are needed (see Fig. 4.2):

- ${}^{EE}T_c$: transformation between the robot end-effector and the coil
- ${}^{bR}T_{bC}$: transformation between the robot and the camera base frames

so that the desired robot pose can be calculated as:

$$ {}^{bR}T_{EE}|_{target} = {}^{bR}T_{bC}\,{}^{bC}T_h\,{}^{h}T_c|_{target}\,{}^{c}T_{EE} \tag{4.11} $$

In eq. (4.11), ${}^{h}T_c|_{target}$ is the above mentioned stimulation target (see eq. (4.10)) and ${}^{bC}T_h$ is the head pose with respect to the camera base frame, acquired through the neuronavigator software. Since the desired pose is usually expressed in a vector representation, in the control law it is useful to express the target as:

$$ {}^{bR}T_{EE}|_{target} = \begin{bmatrix} R_d & p_d \\ 0 & 1 \end{bmatrix}; \quad x_d = \begin{bmatrix} p_d \\ \phi_d \end{bmatrix} \tag{4.12} $$

where x_d is the 6x1 vector representing the desired robot pose and it is composed of the 3x1 position vector p_d and the 3x1 vector of Euler angles ϕ_d computed from the rotation matrix R_d. Given a selected stimulation point, the robot moves the coil on the target 10 cm above the scalp (see Fig. 4.4a), then it proceeds slowly towards the head, keeping the correct orientation (i.e. if the head moves, the control adapts in real time to keep the stimulation face tangent to the scalp). Splitting the trajectory in this way is useful to reduce the risk to collide with the subject, especially when sequential stimulation points are on opposite sides of the head [89]. In this case, the coil first moves far from the head backward on the second path and then it starts the predefined 2-paths trajectory (Fig. 4.4a). Moreover, we ensure that the path is collision-free thanks to the head tracking. Any unexpected collision, both at the tip of the

coil or along the robotic arm, can be detected trough the torques measured at the joints level and the forces estimated at the end-effector (coil), leading to emergency stop and improving the safety not only for the subject but also for the operators. The collision detection was implemented using the SDK libraries provided by the manufacturer (FCI libraries by Franka Emika), which includes a collision detection routine. Both the path segments are planned as minimum jerk trajectories on a linear path, to avoid acceleration discontinuities that badly affect the robot control resulting in emergency stop; when new data are available from the camera, the robot pose is updated according to the head's current pose, as described by eq. (4.11).

Given the mechanical interaction -between coil and head- required in this application, we implemented an impedance control to enhance safety. Indeed a system controlled in motion or force can become unstable when coupled to an environment that is itself stable [90]. The controller stiffness and damping values have been set to allow obtaining a good accuracy in coil positioning while minimizing interaction forces. To identify those values, preliminary tests have been conducted performing TMS sessions on the mock-up head (i.e. styrofoam head in Fig. 4.4b), moved by another Panda robot to simulate the subject's movements. Tests have been conducted varying the control parameters and recording the performance in term of accuracy and interaction forces.

The impedance control was implemented by commanding torques to each robot joint according to the following equation:

$$\tau = J^T\left(K(x_d - x) - D(J \cdot \dot{q})\right) + C\dot{q} + G \tag{4.13}$$

where τ is the 7x1 vector of the joint torques, J is the 6x7 robot Jacobian matrix, x_d and x are respectively the desired and actual robot pose in the cartesian space (i.e. the end-effector pose with respect to the base reference frame, expressed as 6x1 vectors as in eq. (4.12)), $\dot{q}$ is the 7x1 vector of the joint velocities, K and D are the stiffness and damping matrices; C represents the centrifugal and Coriolis forces contribute, whereas G is the 7x1 vector of the gravity forces [1]. The desired pose x_d is the vector representation of the end-effector desired pose, which depends on the coil target pose (${}^{h}T_c|_{target}$) and the head pose (${}^{bC}T_h$), as computed in eq. (4.11) and eq. (4.12).

In our implementation of the impedance control in eq. (4.13), the two matrices K and D are 6x6 diagonal matrices defined as:

$$K = diag(Kx, Ky, Kz, Krx, Kry, Krz) \tag{4.14}$$

$$D = diag(Dx, Dy, Dz, Drx, Dry, Drz) \tag{4.15}$$

The robot employed in our platform is a 7 dof manipulator with torque sensors at each joint, that allows to smoothly implement the torque-based impedance controller in eq. (4.13), allowing to safely regulate the interaction at the tip of the coil. Indeed the embedded torque sensors allow to estimate the interaction force and to adjust the cartesian impedance, using the libraries provided with the Franka Control Interface (FCI), through which the joint torques can be commanded. Moreover, the kinematic redundancy of the robot could be exploited in further applications such as a TMS session with two coils held by two manipulators. Indeed, in this case the redundant dof allows to avoid collision between two robot arms, keeping the desired end-effector poses.
Several safety constraints have been implemented in the control algorithm, so that the robot stops its movement, instead of carrying on with the tracking, when:

- the contact forces on the robot measured by the torque sensors (not only at the coil but also along the whole robotic arm) exceed safety thresholds [83].
- the participant moves the head too fast (as could happen for patients fainting out).
- the markers on the head becomes not visible for a long time, or the head moves too much while the markers are not visible to the camera.

This control aims to follow a target position, but it is implemented through impedance control, which guarantees the stability during interaction tasks by setting a desired mechanical impedance at the interface. This means that even though the controlled variable is the coil position, there is a constraint on the robot mechanical impedance. The proposed control allows indeed to reduce the position error, maintaining the contact on the scalp, without direct regulation of the contact force but regulating the impedance between the robot and the environment in order to not harm the subject during the interaction. An eventual air layer between the coil and the scalp would affect the TMS effectiveness; except for this, smaller or larger contact forces would not influence the stimulation efficacy, but only the subject comfort [82]. After initial validation on a mock-up head, the procedure was performed on six healthy subjects. The assessment of the system with the proposed calibration methodology was performed considering both the accuracy in coil positioning and its usability in a real TMS procedure. As concerns the accuracy, the performance was evaluated in terms of error between the target and actual coil pose, using data acquired from the camera. Specifically, the evaluated errors are:

- the Cartesian norm of the position error, on the stimulation plane.
- the norm, in the $SO(3)$ space, of the orientation error.

Additionally, during real sessions on healthy participants, we evaluated the amplitude of the MEPs, i.e. the peak-to-peak value of the EMG muscular activity evoked by a single pulse of TMS stimulation in the primary motor cortex [49], [81], and compared the results with a similar procedure performed by two expert operators.

The software application and the 3D model of the flange are available at https://github.com/ANoccaro/Robot-aidedTMS.

4.3 Experimental Validation

4.3.1 Experimental Setup

A set of passive reflective markers (named *coil item*) was attached to an eight-shaped coil (Alpha D40 by Magstim). The item had a peculiar geometry that can be recognized by the neuronavigation system. The coil was fixed to the robot end-effector using a 3D printed flange. The flange was printed with the Ultimaker2+ 3D printer using PLA material, with a filling percentage of 70%. The inertial parameters of the flange -together with the screws, the markers and the coil- were set as payload in the robot's settings and considered in the robot control law (i.e. gravity compensation, etc.). The coil's cable was fixed to the side of the flange in order to minimize variations in the center of mass, that was estimated, together with the inertia matrix, by means of a linear regression on the robot forces and torques at the end-effector in different configurations (with the flange-coil system attached).

The coil was registered in the system before starting the calibration; an additional *stylus* item (Fig. 4.4b), provided with the Polaris system, was used to point three points on the coil stimulation surface (focus, left wing and back point), collected by the neuronavigation software to align the predefined item reference frame to the actual *coil* reference frame, centered in the focus and aligned with the electric field (Fig. 4.4a). The coil registration was performed with the coil fixed on the robot, to avoid eventual marker displacements during its mounting.

The camera was roughly placed pointing towards the robot in order to have the camera capture volume maximally overlapping with the robot workspace, with the *coil item* visible to the camera (Fig. 4.1 and Fig. 4.2). After this first manual alignment the calibration procedures allows to properly transform data from the camera reference frame to the robot one.

The robot controller was connected to a pc running on the O.S. Ubuntu 16.04 with real-time kernel. A customized version of the neuronavigation software was employed to stream the camera data to the main control application developed in c++ language, using the Qt

libraries. This customized version of the SofTaxic is equal to the commercial one except for the feature of streaming data of the coil and head marker to third-party software via UDP communication.
This application connects all the system's components, elaborates data read from the camera and the robot, and sends commands to the robot in order to move the coil on the target point. The robot was controlled with a 1 kHz control rate by means of the Franka Control Interface (FCI), whereas the camera sampling rate was 20 Hz. As regards the robot control, the stiffness and damping values defined in section 4.2.4 were set as:

- $K_t = 3000\frac{N}{m}$; $D_t = 80\frac{Ns}{m}$
- $K_r = 80\frac{Nm}{rad}$; $D_r = 10\frac{Nms}{rad}$

with $K_x = K_y = K_z = K_t$, $K_{rx} = K_{ry} = K_{rz} = K_r$ and $D_x = D_y = D_z = D_t$, $D_{rx} = D_{ry} = D_{rz} = D_r$.

The control torque vector (Eq. 4.13) was computed by the implemented control algorithm, using the FCI features to estimate the robot state only (i.e. J, $\dot{q}$, C and G) [91]. Then the torque vector was sent to the robot controller.

4.3.2 Experimental Protocol

In order to test the performance of our calibration procedure, and to validate the whole system during real TMS operations, we ran two main experimental sessions:

1 Calibration session: to collect the points dataset and test the hand-eye and robot-world algorithms.

2 Stimulation session: to test healthy volunteers while recording coil position and orientation errors and MEP responses to TMS stimuli.

4.3.2.1 Calibration Session

In the calibration session the robot moved the attached coil to n different poses, while data from the robot and the camera were acquired at the camera frequency (i.e. 20 Hz); the acquired data were then processed off-line in Matlab 2017, through the three previously described calibration algorithms (see section 4.2.2.1, 4.2.2.2 and 4.2.2.3).
The calibration points were identified as the robot end-effector positions with respect to the robot base frame. The center of the sphere (Fig. 4.3a) was defined so as to roughly correspond to the center of the subject's head, when he/she is seated on a chair at a distance

of 60 cm from the robot base and considering an average subject height of 170 cm. Once the starting point was identified, the rest of the sphere was built in the robot base reference frame, moving the end-effector on the sphere surface as described in Fig 4.3.
The parameters that allow to achieve the best results (i.e. 150 calibration points on the spherical shell using the *SGO* approach, see section 4.4 for details) were adopted to calibrate the system for the TMS procedure on healthy subjects, and to compute the calibration matrices used into the main control application.

4.3.2.2 Stimulation Session

The subject head was placed in the center of the two workspaces (Fig. 4.1 and Fig. 4.2). The head tracker -*head reference item*- was placed on the participant's forehead using a velcro headband (Fig. 4.4b). The head tracker, as well as the coil one, is a rigid-body marker equipped with four passive markers, disposed with a peculiar geometry recognizable by the camera. The headband was placed in order to be as more fixed as possible, avoiding any degree of freedom with respect to the head.
The neuronavigation software was employed to build the 3D model of the brain and the scalp of the subjects, allowing to register the stimulation point. The latter was selected as the area of the left primary motor cortex (M1) that elicits the MEP in the contralateral First Dorsal Interosseus (FDI) muscle with the lowest stimulator intensity (FDI Hotspot) [92].

The target -motor hot-spot- was manually picked by an expert operator gradually moving the coil over the motor cortex to find the location that evokes the largest EMG responses, while applying a series of pulses at a relatively high intensity [93], [94].

The selected target of stimulation, characterized as a coil position and orientation (i.e. tangent to the scalp and rotated in order to induce a postero-anterior current perpendicular to the main dimension parallel to the Central Rolandic Sulcus) with respect to the head, was streamed to the main control application, together with the head and coil poses with respect to the camera base frame. Once the stimulation session started, the robot moved the coil on the stimulation point over the scalp.
The stimulation trigger was automatically provided after at least 5 seconds from the previous one, only if the error between the current coil pose and the hot-spot was under a threshold set by the experimenter (5 mm and 5 deg in the presented validation [60]). The error threshold constraint was present both during the robot-aided session and the manual session, with the trigger automatically provided by the implemented control interface (as done in the robot-aided session). To do this, the software controlling the robot sends a trigger to the magnetic stimulator (Magstim BiStim), via a dedicated electronic board connected through a

serial port, only when the conditions on the errors are satisfied. The trigger consists in a 5 V square-wave signal with a 10 ms duration.

MEPs were collected by measuring the EMG response to a single TMS pulse delivered on M1 over the FDI hotspot. EMG was recorded from the FDI of the right hand, using surface Ag/Cl electrodes. Electromyographic signals were acquired and processed using the Digitimer D360 amplifier, the Power1401-3A interface (CED) and the Signal software. The resting Motor Threshold (rMT) was established as the lowest percentage of the Maximal Stimulator Output (MSO) required to produce at least 5 out of 10 MEPs greater than 50 μV in the right FDI. The FDI hotspot, i.e. the site over the left M1 scalp that has the lowest rMT in the FDI muscle was chosen as the stimulation point and selected in the neuronavigation software.

Six right-handed healthy participants were tested. Participants were enrolled after having signed a written informed consent and experimental procedures were approved by the Ethics Committee of the Università Campus Bio-Medico di Roma (EMBODY protocol) and carried out according to the Declaration of Helsinki. Each participant underwent four experimental sessions. In the first two, the experimenter manually administered over the FDI hotspot 30 TMS pulses with the intensity set at 100% of the rMT (session 1) and 30 pulses with the intensity set at 120% of the rMT (session 2), respectively. The minimum interstimuli interval was set to 5 s. The expert operators used the neuronavigator as visual guide moving the coil upon the head. It is worth to notice that the trigger to the stimulator was provided automatically using the electronic board even during the manual session, relieving the operator from pressing a pedal or a button. This choice led to avoid the slight movements usually done by the operator to deliver the stimulation, intrinsically improving his performance. The third and the fourth sessions were administered using the robot-aided TMS platform, handing out the same number of stimuli as delivered in the first two sessions with the same parameters (i.e. 30 stimuli at 100% rMT in session 3 and at 120% rMT in session 4).

4.3.3 Data Analysis

We ran a statistical analysis both on the calibration data and on the comparison between robot and human experimenters performance. In particular, we run a Kruskal-Wallis test on the calibration errors data, with "method" and "workspace" as main factors (a non-parametric test was used due to the non-normality of the data, checked by Shapiro-Wilks test). We selected to test the datasets with more than 70 calibration points. Considering the stability of the outcomes for these datasets, the number of calibration points was not treated as factor in statistical analysis.

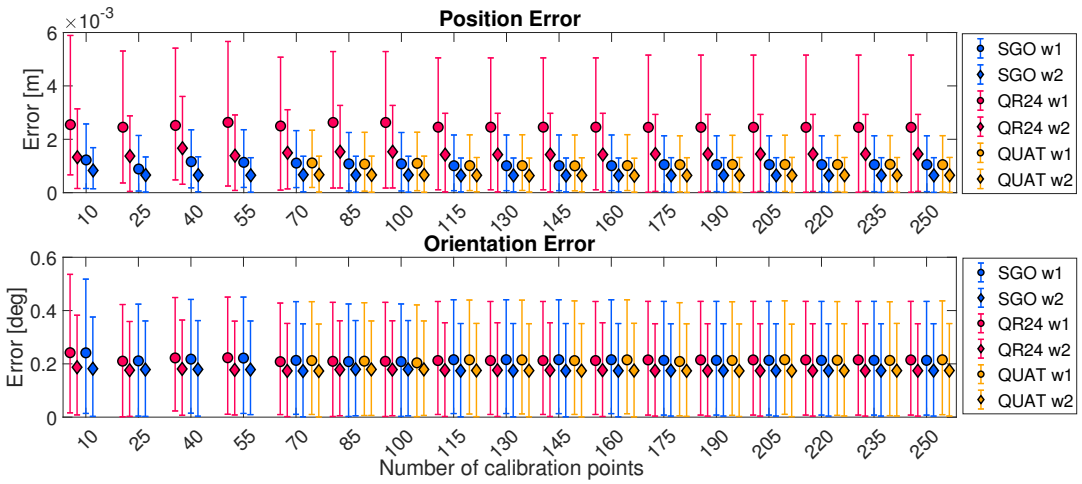

Fig. 4.5 Position and orientation errors using the *SGO*, *QR24* and *QUAT* calibration method. Errors are evaluated in the useful TMS workspace, selecting the calibration points in the whole sphere workspace (w_1) or in the useful one (w_2). The dots represent the median value and the extreme points of the bars represent the $25^{th}$and 75^{th} percentile, computed on 5 different datasets.

Before running the analysis, data were grouped in 5 datasets, taking the median value of each group (out of five) randomly created. Mann-Whitney tests were used as the post-hoc tests to compare the effect among the three algorithms, using Bonferroni correction.

The coil positioning errors during the robot-aided and manual TMS sessions were analyzed using a Mann-Whitney test. In the validation on healthy subjects we considered only the errors measured when the stimulation was provided (at the instant triggered by the TMS stimulator), since they are the only which matter for the efficacy of the stimulation.

The comparison between the MEPs elicited in the manual session and the ones elicited in the robot-aided session, was conducted using the Generalized Estimating Equation.

4.4 Results

In Fig. 4.5 the position and orientation errors obtained using the *SGO*, *QR24* and *QUAT* algorithm are shown, respectively. Each graphic depicts the median value and the 25^{th} and 75^{th} percentile of the position and orientation error obtained among the evaluation dataset, varying the number of points taken into account to estimate the calibration matrices. Points involved into the calibration were selected from two different workspaces, as explained in section 4.2.3:

- w_1: the entire sphere (workspace for a general application)
- w_2: the spherical shell (specific workspace readapted for robot-aided TMS)

As visible from the plots, both for the position and orientation, the error is higher for small values of the number of calibration points, whereas it settles when more than 70 calibration points are employed. Of note, employing less than 70 points, the *QUAT* method resulted in a lack of convergence of the algorithm in both w_1 and w_2, thus exhibiting errors some orders of magnitude bigger than other methods/number of points; for this reason these datapoints were not displayed in Fig. 4.5.
The general trend of the error as function of the number of calibration points confirmed the preliminary results obtained in the previous work [84]. The statistical analysis revealed a main effect of the workspace selection on both the position ($p < 0.001$) and orientation error ($p < 0.001$): all the calibration algorithms result in errors for the w_2 lower than the w_1 with a 34% reduction for the position errors and a 18% decrease for the orientation ones.
Conversely, the use of different calibration algorithms affects the position errors ($p < 0.001$), but not the orientation ones ($p = 0.995$). Mann-Whitney test, corrected for three comparisons, revealed that the *QR24* method is significantly worse ($p < 0.001$) than the *SGO* and *QUAT* ones, regardless the workspace selection; conversely, there is no difference between the errors obtained with the *SGO* and *QUAT* methods, except for the convergence problem of the *QUAT* approach for small number of calibration points.
Table 4.1 reports the duration of the calibration session depending on the number of collected points: from less than one minute for 10 points to 11 minutes for 250 points. The computational time needed to run the calibration algorithms is negligible with respect to the collecting data procedure (tens of seconds vs few minutes), therefore it was not reported.
Summing up, among all the different configurations and parameters adopted, the calibration procedures that guarantees lower errors is the one taking more than 150 points on the spherical shell, using the *SGO* algorithm (average errors lower than 0.5 mm and 0.2 deg).
Concerning the assessment of the robot-aided TMS system on healthy participants, Fig. 4.6 shows the distribution of coil positioning errors during the TMS stimuli administration, comparing the manual (red) and robotic (blue) stimulation sessions. When the robot administered the stimuli, the coil position error is not significantly different ($p = 0.982$) compared to the manual session, even though the distribution is slightly less spread and the median value decreases by 6%. On the other hand, the robotic platform achieved significantly lower orientation errors than the expert operators ($p < 0.001$), reducing the median value by 46%.

The amplitudes of the MEPs elicited in the robot-aided and manual session at 100% and 120% of the rMT intensity, respectively, were compared using a Generalized Estimating Equation (GEE) through the SPSS Statistics software, with the experimenter (robot or human) and the intensity of stimulation (100% of rMT or 120% of rMT) as factors. No significant differences were found between the robotic and manual stimulations ($p = 0.94$).

Table 4.1 Duration of calibration session

Number of Calibration Points	10	25	40	55	70	85	100	115	130	145	160	175	190	205	220	235	250
Duration [min]	0.69	1.37	2.02	2.69	3.32	3.97	4.62	5.27	5.89	6.54	7.19	7.82	8.47	9.09	9.74	10.37	11.02

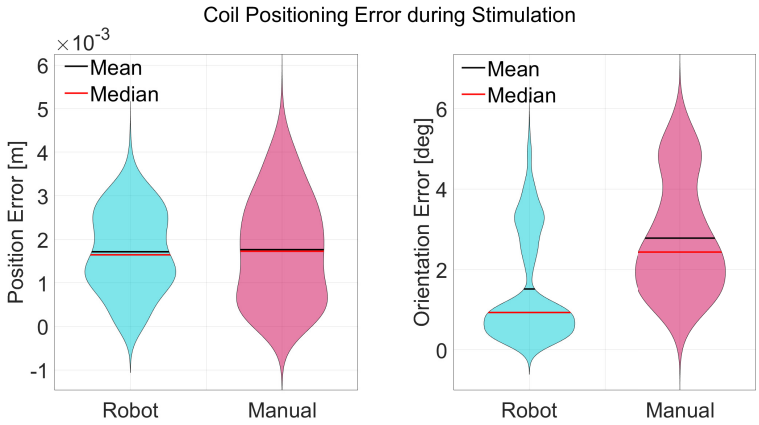

Fig. 4.6 Coil positioning errors (position [m] and orientation [deg]) recorded during the stimuli administration provided by the robotic platform or manually by the expert operators.

4.5 Discussion

The approach presented in this chapter can be employed by the scientific community working on TMS, even using different devices. The proposed control (as well as the calibration) can be adapted to any robotic manipulator with at least six degree of freedom and joint torque sensors; any neuronavigator -e.g. an open-source one [95]- able to provide to thirdy-parts software the pose of the coil, head and the hot-spot data. Likely, the stimulator can be replaced with any stimulator provided with an external triggering module, thanks to the electronic board integrated in our system.

While systems previously developed used non-orthogonal or laser-based methods for calibrating the system [78], [96], we proposed three different algorithms (*SGO*, *QR24* and *QUAT*), presented in [75], [80] and [76] for different applications, customizing the calibration workspace according to the one required by the TMS.

Experimental results showed an improvement of the calibration performance for all the tested algorithms, suggesting that constraining the calibration dataset to the TMS useful workspace is a good practice, regardless to the specific mathematical approach implemented. Compared to generic approaches, our TMS robotic platform decreases calibration errors by 34% and by 19% for the position and orientation, respectively. It is worth noting that while reducing the calibration workspace usually implies limitations in the effective use of the system (i.e. limited workspace), this is not the case for this specific application, since the

excluded workspace can not be used anyway due to the presence of the subject's head. Moreover, we found in the present scenario that a global optimization method (*SGO*) minimizes the positional calibration errors significantly better than non-orthogonal approaches (*QR24*) influenced by scaling factors [97]. Even though there are no differences between the *SGO* and *QUAT* algorithms in term of errors, the *SGO* algorithms shows stable performance also for small number of calibration points, revealing its feature to obtain good results even with noisy data.

As regards the control of the robotic arm, we implemented an impedance controller that exploited the torque sensors embedded in robot joints, achieving high accuracy in keeping the coil on the hot-spot, limiting the interaction force between the coil and the head. We indeed convert motion errors into robot torque commands (via Jacobian transform) in order to compensate head movements while controlling interaction impedance (for safety reasons). Moreover, our control algorithm allows to adapt in real time the trajectory while approaching to the head, compensating the head movements occurred during the first phase of the planned movement, conversely to the systems previously proposed [98], that use position and/or force control [53], [79], dealing with stability issues during contact/non-contact transitions (thus reducing the safety of the subjects) [99].

Our torque control allows to efficiently follow the target both for slow and fast movements, not exceeding the maximum contact force between the coil and the head. Going beyond simulations and tests with mock-up, we tested the whole platform during a real TMS procedure involving six healthy volunteers, proving that it allows to elicit MEPs not different in amplitude to the ones evoked by two expert users during a manual TMS session that benefits of the neuronavigator. This is the first evidence that the system could be effectively employed in TMS studies. Furthermore, the presented platform -intended as the integration of the robot, the cameras and the neuronavigation software in a single system controlled through the presented control strategy- achieved a better rotational accuracy and a comparable positional one, with respect to the experimenters. Our platform yielded a coil positioning accuracy lower than 2 mm, equivalent to the one declared by Axilum for his TMS-Cobot system [66] and lower than the one obtained by Matthäus and colleagues which is lower than 3 mm [89]. Moreover, the platform allows to achieve 1.5 ± 1.3 deg of accuracy, significantly reducing the orientation error by 46% ($p < 0.001$) with respect to the stimulation provided by the human operators. Although there is no clear evidence that 1 mm and 1 deg variations in the position and in the orientation hugely affect the efficacy of TMS procedures [100], de Goede and colleagues [55] showed that "at the subject level significant effects on MEP amplitude, TEP, and LICI were found for changes in coil location or orientation". After testing position variations of 2-5 mm and 10 deg, author concludes that "This study indicates

that a high accuracy in coil positioning is especially required to measure cortical excitability reliably in individual subjects using single or paired pulse TMS". This is another evidence that providing a tool capable to constantly maintain errors below that thresholds can be beneficial for TMS-based protocols. The experimental session was carried out testing the lowest stiffness values allowing to have an effective stimulation, keeping the contact with the head as more comfortable as possible. Hence, the subjects referred to feel the coil less uncomfortable and to experience the whole robot-aided session more pleasant than the manual one. The use of an automatic stimulation trigger even in the manual session was to force the stimulation to be within the error margin set on the neuronavigation system; without this further control, the human operator could have triggered a stimulus even if the target was not in the correct spot (within the preset tolerance), and this could have strongly biased our results in favor of the robotic system. We think our experimental choice is more conservative and strengthens the obtained results.

4.6 Conclusions

Results showed that, using the presented approach rather than a general one, the position and orientation errors significantly decrease ($p < 0.001$) by 35% and 19% respectively, regardless to the implemented algorithm; the *SGO* algorithm showed significant better results than the *QR24* method and more stable performance than the *QUAT* one, confirming its best performance, as assessed in the previous work. It is worth noting that the presented method, used here to optimize the overall error, can be employed in other techniques where a higher accuracy is needed, e.g. ultrasound stimulation.
The system was validated in a real TMS session on six healthy subjects, leading to higher accuracy than the experimenters -guided by the neuronavigation software- in term of orientation errors, that significantly decreased by 46%, while obtaining a slight 6% reduction for the position errors.
Furthermore, by adapting the workspace of the calibration methodology, the proposed system can extend the use of current TMS procedures to implement TMS protocols while the subjects are performing a functional task. Future perspectives would include dynamic error assessment during functional tasks and the involvement of two robots for a double-coil stimulation, fully exploiting the redundancy of the robotic manipulators in avoiding conflicts in the joint space while keeping the coil in the right hot-spot.

Chapter 5

Human performance in three-hands tasks

In this chapter I analyze human performance in three-handed tasks. In particular I focuse on the difference among tasks including different number of goals and/or mechanical constraints and on the difference between one subject controlling three limbs at the same time and two people working together and sharing the control. The aim is to understand if and in which scenarios humans are able to perform three-handed operations.

5.1 Background

Recent years have seen an increasing interest in human augmentation. Researchers have attempted to go beyond the restoration of lost abilities, giving humans the possibilities to execute actions impossible to perform with their natural motor capabilities [6].
The use of a supernumerary limb to perform three-handed tasks, for example, opens a new wide range of possibilities in industrial and medical scenarios. The need of three hands is, indeed, typical in surgery operations, where the surgeon needs the help of an assistant (human or robotic) in order to hold the several instruments -and the camera in case of laparoscopic surgery. The communication between the surgeon and the assistant, as well as the assistant's skills, are crucial to successfully conduct the operations [101]. Assistants are often affected by fatigue, that leads to unexpected movement of the instrument; also novice assistants may be unfamiliar with the surgeons and misunderstand their needs [102].
Robotic assistants directly controlled by the surgeon may overcome these issues; however, their control needs to be intuitive and accurate. The surgeon must keep their focus on the surgery and cannot be distracted by the control of the robotic device.

Beyond surgery, this argument is still valid for everyday life tasks. People often need the help of someone else to move a table, to nail down a sliding surface, etc. The recent development of supernumerary robotic limbs tried to address these needs; many different devices have been proposed, from supernumerary fingers to industrial devices that lift heavy objects [103],[104].
Regardless of the specific device or its application, the use of the robotic system must be intuitive and should not affect the user's performance during the task. This issue has been addressed in the literature: several studies focused on control strategies, employing EMG or BMI interfaces, or on feedback approaches to improve the control intuitiveness [105].
However, little has been provided on the main question "Are humans able to reliably make use of three hands in task augmentation scenarios?". Abdi and colleagues investigated the use of a third hand in a demanding task, assessing that participants achieved better performance using three virtual hands (controlled by the hands and one foot) rather than two [106]. That study represents a starting point to further investigate the field of three-handed task. While they compared the same task performed with two or three hands, we want to focus on tasks that a priori require three hands, assessing how subjects manage the control of three limbs simultaneously compared with how they manage the cooperation with another person.
Thus, the objective of this chapter is to assess the performance of people using three-hands in demanding tasks, and also to investigate how this performance varies across different scenarios -tasks with mechanical constraints such as moving a sheet with an object placed on it or tasks with different sub-goals as when you drive a car and you have to push the pedal while operating on the transmission and the steering wheel.

We also consider how the demand of the three handed control by the same person compares to two people working together and sharing the control (as in the case of a human assistant).
The two main questions we want to address in this chapter are: i) Are humans able to reliably make use of three hands in task augmentation scenarios? ii) How does the performance of a single subject controlling all three hands compare with that of two subjects performing the tasks together?
Additionally, for each question, how does the answer vary across different scenarios?

5.2 Methods

We used the dominant foot as a "third" hand, as mostly done in surgery, and also to have a direct comparison with previous studies on three-hands tasks [107], [106].
We selected three different scenarios (Fig. 5.1) to study human performance: i) three

independent hands, uncoupled, with three different goals; ii) two hands mechanically coupled plus an independent hand, with two different tasks; iii) three hands mechanically coupled with one task. The tasks are all 2D, employing only 2 translational directions and no rotations. A visual feedback simulating a haptic interaction renders clear the mechanical coupling, that is achieved only in the virtual environment through a visually-simulated elastic membrane connecting the virtual hands. No physical springs connect the participants' hands or their hands and the foot; instead the virtual hands are coupled by means of a virtual elastic band. An additional task is employed to allow the participants to get acquainted with the setup and the videogames; this familiarization task requires the hands to move independently and one hand at a time. The purpose of the familiarization phase is to ensure that the subjects become confident with the mapping between each device and its respective virtual hand.
A detailed description of the familiarization and the other tasks is provided in the following sections.

5.3 Experimental Setup

The hands and foot position are acquired using three sensors from the electromagnetic tracking system Polhemus Liberty (Fig. 5.2). The sensors are placed on the wrists and on the dominant foot using a 3D printed holder with a layer of foam and velcro straps. The Polhemus Liberty tracker is placed behind the participants; the tracker has the x-axis pointing towards the screen and the z-axis pointing up.
A projector is used to project the game on a vertical screen. The participants are seated on two chairs in front of the screen projector. To rule out the chair position from having effect on the selection of targets on one side of the screen, especially during the foot control, subjects kept the same chair during all the sessions (Fig. 5.3). The distance threshold to consider the cursor on the target is 1 cm in the virtual environment.
The game is developed in the C# language using the Unity3D development environment.

5.3.1 Control

In order to downsize the complexity of the task, focusing on the use of "three hands" in different scenarios, we selected 2D tasks, considering only planar movements and no rotations. The virtual cursors are controlled through the movements of the participant's right and left hands and the dominant foot. Movements in the horizontal plane are mapped on a vertical screen. Lateral movements correspond to the x-axis movements on the screen, whereas movements towards the body or far from it are mapped as vertical movements on the screen.

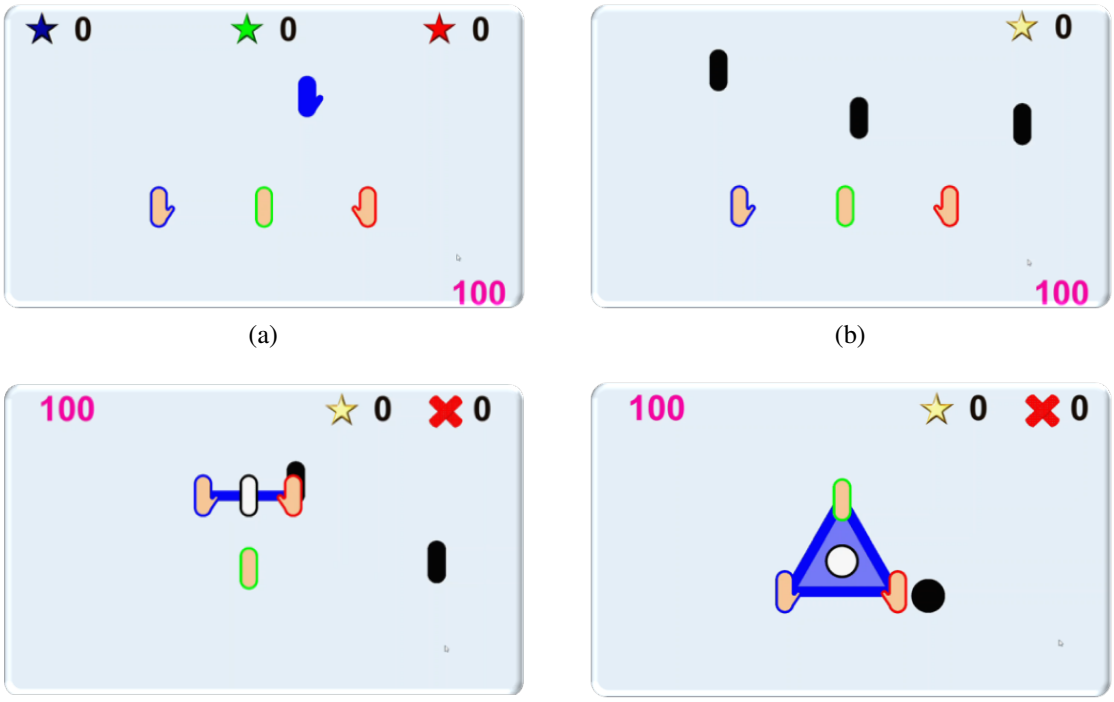

Fig. 5.1 Representation of the virtual environment for the different tasks: a) Familiarization: one target appears at a time, with the same color and shape of the limb that has to reach it; b) Independent Task 1: three black targets appear at a time, each cursor has to reach a different target; c) 2-coupled Task 2: the two hand are virtually coupled by means of a blue spring. Two targets appear at a time. The hands have to move the center of mass of the spring, i.e. the white cursors, on one target without overstretching or overcompressing the springs, while the foot moves on the other target; d) 3-coupled Task 3: one black target appear at a time. The three hands are coupled by means of three blue springs. The area within the springs has a triangle shape and the white cursor represents its center of mass. The hands have to put the white cursor on the target without overstretching or overcompressing the springs, keeping the cursor inside the triangle.

The hands are not constrained and can also move in the up-down direction; however these movements, as well as the rotations, do not affect the cursor's position on the screen.
To avoid fatigue, participants can slide the foot on the ground - a slippery shoe liner is fixed under the foot using velcro straps and allows to reduce the friction with the ground, in turn covered with a slippery surface. The position of each hand (or foot) is computed with respect to the position at time zero. The real displacement along the horizontal plane is mapped to the virtual environment through scaling factors (sh for the hands and sf for the foot), in order to allow each subject to cover the whole workspace with small and comfortable limbs movements. The scaling factors are computed as follows:

$$sh = [\frac{1}{8} * (0.129 + 0.186) * h]/SD; \tag{5.1}$$

$$sf = [\frac{1}{8} * (0.285 - 0.039) * h]/SD. \tag{5.2}$$

These equations estimate the limb's range of motion of each participant depending on the their height h [108]; this workspace is then scaled with a factor ($\frac{1}{8}$) and compared to the minimum dimension of the screen SD. The virtual hands position are obtained by multiplying the sensor's measures by those scaling factor. These positions represent the desired ones in the virtual force control used to move the cursors.
Cursors are controlled by a virtual force and they are represented as smoothed rectangles with a colored contour -red for the right hand, blue for the left hand and green for the foot- and a thumb that recalls the shape of right and left hand (Fig. 5.1). The virtual environment is built in Unity, which helps to simulate physics and ensures that the virtual objects correctly accelerate and respond to collisions, gravity, and various other forces. In the present case we used the 2D physics engine implementation. The force applied to each cursor (provided with a unitary mass) is:

$$F = k_{sg} * (p_d - p) - k_{dg} * v; \tag{5.3}$$

where p_d and p represent the desired and actual cursors position; v is the current cursor velocity; k_{sg} and k_{dg} are the proportional and derivative stiffness values computed as follows:

$$\begin{aligned} k_{sg} &= k_p * g; \\ k_{dg} &= (k_d + k_p * dt) * g; \\ g &= 1/(1 + k_d * dt + k_p * dt^2); \end{aligned} \tag{5.4}$$

with $kp = 500$ N/m, $kd = 1.5 * \sqrt{kp}$ and dt the time between two following frames.

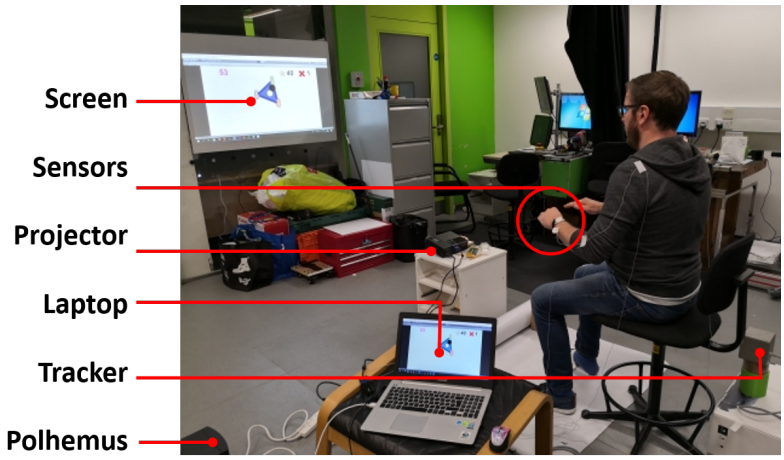

Fig. 5.2 Experimental setup: Hands and Foot movements tracked using a motion tracking system (Polhemus Liberty). Sensors are placed on the wrists and dominant foot. Only the movements in the horizontal plane are mapped into movements on a vertical screen. The Polhemus tracker is placed behind participants, with the x-axis pointing towards the screen and the z-axis up. A projector is used to project the game on a vertical screen.

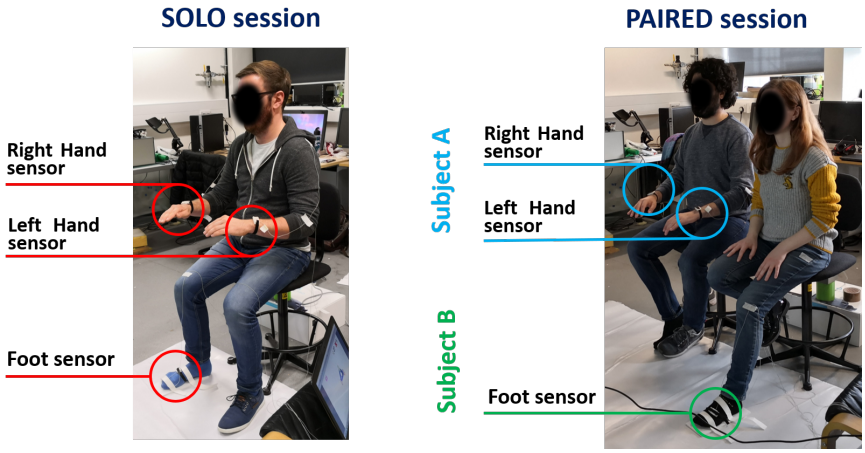

Fig. 5.3 Experimental setup: on the left side a participant performing the solo session controlling the three limbs; on the right side a dyad performing the first part of the paired session, one subject controls the two hands while the other control the foot. People are seated on the same chair during all the sessions.

5.3.2 Familiarization

In the familiarization phase there is no mechanical coupling between any limb (hands or foot) and one target at a time appears on the screen. The target has the same color and shape of the hand that has to reach it (Fig. 5.1a). The aim of the task is to reach as many targets as possible with the corresponding hand in 100 s. As for the other tasks, there is timeout condition, so that if a target is not reached within 3 s, it disappears and a new target appears on the screen. The score is computed by summing the number of targets reached with each hand.

5.3.3 Task 1: Independent

In the independent task the hands can move independently from each other. Similarly to the familiarization, the aim is to reach as many targets as possible in the allowed time of 100 s. Three black targets are presented simultaneously (Fig. 5.1b) and the subject can arbitrary choose the hand associated to each of the three targets. The core increases when each cursor is located close enough to a different target at the same instant of time. After 3 s, the targets reset and new targets appear in different positions. Each hand has an independent goal, i.e. has to reach a different target, but the overall task is collaborative, requiring to reach the three goals.

5.3.4 Task 2: 2-coupled

The 2-coupled hands task includes a virtual spring connecting the two virtual hands (corresponding to the participant's left and right hands). The center of the spring is highlighted with a white cursor (Fig. 5.1c). Two black targets appear on the screen.
In this task: i) one target has to be reached by the cursor in the center of mass of the elastic band moved by the two hands; ii) the other target has to be reached by the virtual foot. The first sub-task requires also to avoid the band overstretching or overcompressing.
If any of the goals is not completed within 3 s, the two targets disappear and other two targets appear on the screen.

As for the independent task, there is no cue on which cursor has to reach which target, but to get the score point, the cursors (i.e. virtual foot and white cursor) need to be close enough to the respective target at the same time.
Each band breaking due to stretch or compression is counted as a fail. The final score is given by the difference of the positive score (target reached) and the number of fails.
A pseudo-haptic feedback is provided at the spring: the virtual band changes color and width

depending on the distance between the two connected hands (o cursors). In order to best render the elastic force effect, the cursors are controlled using virtual force control. The virtual environment allows to set a mass on the cursors and to use the laws of physics on the virtual objects, e.g. providing the cursors with mass and inertia and applying forces.
The position of each virtual cursor -with unitary mass- is computed applying the force needed to move the cursors in the desired position (computed mapping the real hand position to the screen environment). In case the hands are connected through an elastic band, with a given stiffness K_e, the force applied on each cursor is the sum of the driving force (given by the real hand movement) and the elastic force provided by the band. This control results in a mismatched position between the real and virtual hand, when the elastic force reaches high values. However the limited workspace makes this mismatch negligible. On the other hand, the force control results in the best pseudo-haptic feedback rendering.

5.3.5 Task 3: 3-coupled

In the three-coupled task the three virtual hands are all mechanically coupled to each other through an elastic band (Fig. 5.1d). Each hand holds one corner of the elastic band.
The aim of task is to put the center of mass of the triangle (highlighted with a white cursor) on the target. The triangle is defined by the area within the three springs that connect respectively the two virtual hands, the right hand and the foot, the left and the foot. The three springs must preserve, within a defined range, their initial lengths to avoid a fail in the task.
Moreover, the hands must keep the white cursor -i.e. the center of mass of the elastic band- into the elastic area.
Pseudo-haptic feedback is provided through the triangle in the sense that the force in the spring for each length is shown by the coloring and the width of each spring.

5.4 Experimental Protocol

Thirty subjects, organized in fifteen dyads or pairs participated in the experiment. Before starting the experimental session, they filled an informed consent approved by the Imperial College Research Ethics Committee. Dyads are recruited to address the question: "how the performance of a single subject doing trimanual task compares to two subjects doing the same task together". Dyads were created randomly, without paying attention to match the gender or the dominant foot. The dyad performs 3 sessions in a random order (Fig. 5.4):

- Solo Session: Subject A controlling the hands and the foot; Subject B controlling the hands and the foot.

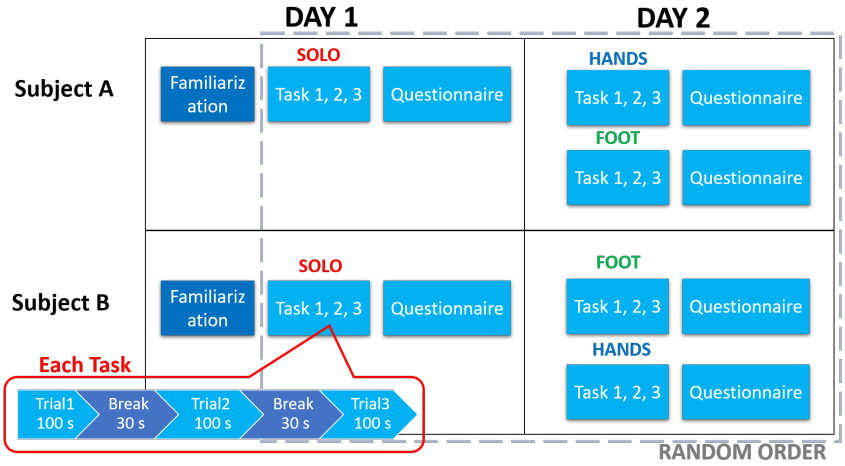

Fig. 5.4 Experimental protocol: Each subject (A and B) performs three sessions in two different days. Familiarization is always performed during the first day, then Solo and Paired sessions order are randomized. Each session considers the three tasks (independent, 2-coupled and 3-coupled) arranged in a random order, except for the independent task that is always performed first. Each task is repeated three times (three trials of 100 s each) with a break of 30 s between following repetitions.

- Paired session 1: Subject A controlling the hands and B the foot.
- Paired session 2: Subject B controlling the hands and A the foot.

Each session considers the three tasks (independent, 2-coupled and 3-coupled) arranged in a random order, except for the independent task that is always performed first, in order to not bias people with coupled movements required in the other tasks before executing the independent task.

In turn, each task is performed three times (three trials, each one of 100 seconds followed by a 30 seconds break). Participants cannot communicate during the experiment. The three sessions are conducted on two different days in a random order: at day 1 subjects perform the solo session, on another day (2) they perform the two paired sessions. At the end of each session subjects fill a questionnaire. The familiarization phase is always performed at the beginning of the first day, one subject at a time controlling all the three virtual limbs.
The virtual hands can move inside the whole rectangular screen, whereas the targets appear only in a centered square (Fig. 5.1). The task duration for each trial is 100 s. The maximum amount of time allowed to reach the target is 3 s. Each score point is followed by a “coin" sound reward, whereas each fail is followed by a “buzzer" sound effect.

5.5 Data Analysis

Performance is evaluated using the following indexes:

- Score: the number of completed sub-trials minus the number of fails (fails only apply in 2-coupled and 3-coupled tasks). We also evaluated separately the positive number of completed sub-trials, without considering fails.
- Normalized Sub-Trial Time: average of the time required to complete a sub-trial divided by the initial distance between cursor and target.
- Normalized Traveled Distance: the average distance traveled by each virtual cursor on the screen, divided by the total number of sub-trials.
- Limb Speed Correlation: the correlation coefficient of the speed profile (absolute value) between cursor pairs: dominant-hand / non-dominant hand; dominant hand / dominant foot; dominant foot / non-dominant hand.
- Smoothness: the spectral arc length [109] of the speed magnitude of each cursor.
- Spring Length Variation: the root mean square of the length variation of the connecting spring (in the 2-coupled) or the root mean square of the length variation of the three connecting springs (in the 3-coupled task).
- The percentage time distribution combined cursor movements: the percentage amount of time the cursors are moving simultaneously or one/two at a time; we consider a cursor moving when its speed is higher than 1.5 cm/s.
- Number of conflicts: number of times more than one cursor is close to the same target, divided by the number of total sub-goals and number of cursors that can conflict. The distance threshold used to compute the conflicts is 2 cm (two times the one used to compute the score).

From the questionnaire we compute a preference, difficulty and perceived effort rank both for the three tasks and for the three sessions (solo, hands control, foot control). The data were analyzed in Matlab 2020.
A statistical analysis was computed using the Jasp Statistics software. A 2-way RM ANOVA was used to analyze the measures of the score, the average time needed to reach the targets and the movement combinations; the factor analyzed were the Task Task 1, Task 2, Task 3 and the Control Solo, Couple. A 3-way RM ANOVA was used to analyze the Speed correlation, adding the Limb Combination as factor (3 levels: Dominant Hand-Non Dominant Hand

(DH-NDH), Dominant Hand-Dominant Foot (DH-DF), Non Dominand Hand-Dominant Foot (NDH-DF)). Mauchly's test was used to check data sphericity, eventually corrected using the Greenhouse-Geisser correction. Score, Spring Length Variation, Number of conflicts, Smoothness, Normalized Traveled Distance and Limb Speed Correlation were analyzed with a Durbin test, after checking their non-normal distributions by means of Shapiro-Wilks test. Post-Hoc tests were corrected with Bonferroni correction. In case of non-normal data post-hoc analysis was performed using Wilcoxon test.

5.6 Results

The results show that couples perform better than solo subjects in term of score ($p<0.001$). Participants perform significantly better in Task 3 (3-coupled task) than in Task 1 ($p<0.001$) and Task 2 ($p=0.03$); the 3-coupled task shows also a smaller difference between Solo and Couple than the two-coupled tasks ($p=0.024$). These results are confirmed also looking at the Target reached (Fig. 5.6), not considering the amount of fails: Task 3 shows values significantly higher than Task 2, in turn better than Task 1 (all p values lower than 0.001); in all the tasks solo subjects reached less target than couples ($p<0.001$). This means that in general people controlling three limbs perform better in the 3-coupled task than in the others. The same result is confirmed looking at the average time needed to reach the targets (Fig. 5.7); in this case lower values correspond to better performance. As showed by the score, subjects need less time to complete the sub-trials when working in couples rather than alone ($p<0.001$) and they perform better in the 3-coupled task than in the other two ($p<0.001$), especially in the solo session.
The distance traveled by single cursors during the trials is higher for the foot than for the hands ($p<0.001$) (Fig. 5.8); the distance covered by the Dominant Hand is the lowest one ($p<0.001$). Couples again perform better than solo subjects: the distance traveled by the cursors on the screen (divided by the number of total sub-goals) is in all cases lower for the coupled session than for the solo one ($p<0.001$).
We analyzed the absolute value of the speed profile for each virtual limb. The correlation among these speed profiles reveals higher values in the tasks with mechanical coupling, as expected, with Task 1 lower than Task 2 ($p<0.001$), in turn lower than Task 3 ($p<0.001$) (Fig. 5.9); also, the more the virtual springs, the higher this correlation is, i.e. Task 3 has significantly higher correlations than Task 2, with the exception of the correlation between dominant and non-dominant hand, which exhibits the highest values in Task 2.
The two hands movements are significantly more correlated than the movements of one hand and the foot; there is no difference between either hand considered together with the foot.

Regardless to the tasks and the limbs combinations, dyads' movements are more correlated than solo subjects movements ($p<0.001$).
Similar results occur considering the limbs' smoothness. Movements are less smooth in the solo sessions (Fig. 5.10) than in the dyad ones ($p<0.001$), whereas they are significantly smoother in Task 2 and Task 3 rather than in Task 1. The foot movements exhibit lowest smoothness ($p<0.001$).
Two opposite behaviors emerge from the length variation of the elastic band. Both solo and paired subjects tend to move the hands close to each other in the two-coupled task, compressing the elastic band (values lower than one); on the contrary, in the three-coupled task the band is almost always overstretched, both in solo and dyad conditions (values higher than one). Considering the variation rate, there is no difference between solo and dyad conditions, considering the average rate of all the springs. However, if we look only at the variation rate of the spring connecting the hands, solo subjects performed worse than dyads ($p=0.002$), whereas Task 3 reveals significantly worse performance than Task 2 ($p<0.001$). In Task 3 only, the variation rate of the springs connecting the foot with the hands is higher than the value of the spring connecting the hands ($p<0.001$).
Most of the time the three limbs move simultaneously; the percentage is higher the more they are mechanically coupled -Task 1 percentage is significantly lower than Task 2, that in turn shows values significantly lower than Task 3- and in the coupled sessions more than in the solo ones ($p<0.001$) (Fig. 5.12). The two hands move together more than single hand movements and more than hand-foot movements. The dominant-non-dominant hand percentage of simultaneous movements in the 2-coupled task is significantly higher than in the independent but also than the 3-coupled task. While the movements of the three limbs together occur more frequently for couples than for solo subjects, the simultaneous movement of two limbs or the movement of one hand at a time occurs much more frequently in solo than in paired sessions (DH-NDH $p<0.001$; DH-DF $p<0.001$; NDH-DF $p=0.002$; DH $p=0.005$; NDH: $p=0.003$). No significant differences have been found among solo and dyad sessions, as well as between Task 1 and Task 2, for the percentage of time with only the foot or no limbs moving, that shows small values; whereas in both cases Task 3 shows lower values than Task 1 and Task 2 ($p<0.001$)
Intuitively, the number of conflicts is significantly higher for the paired sessions and in the independent task (Fig. 5.13).
The questionnaires reveal that most of the subjects prefer the three-coupled task, even tough they find it difficult in the paired sessions (either controlling the hands and the foot). On the opposite the independent task is the least preferred in any case - solo, hands and foot session (Fig. 5.14 and 5.15). People prefer to work in dyads rather than alone and the foot control is

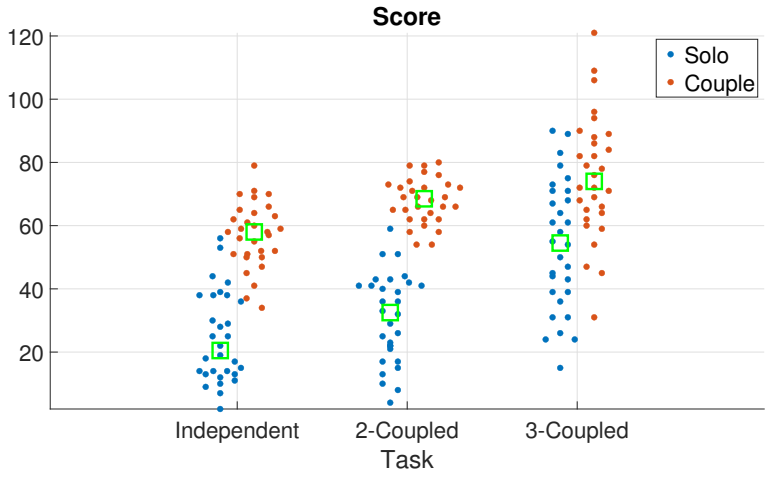

Fig. 5.5 Score for Task 1, Task 2 and Task 3. Each dot represents the value of the last trial. Blue dots correspond to solo sessions; red dots correspond to paired sessions.

perceived as more difficult the less the task is independent (from independent to 3-coupled). In contrast hands control is perceived less difficult the less the task is independent (from independent to 3-coupled). There is no clear preference for the foot control (rather than the hands) and it is perceived as difficult even though it is the one requiring "less" effort (Figs. 5.16, 5.17 and 5.18).

Looking at single subject (solo or coupled) sessions, the workspace distribution among the three cursors changes for each task (see Fig. 5.19). The three cursors move in the same overlapped workspace when performing the independent task, completely sharing the task area. In the two-coupled task the mechanical coupling between right and left hands arises also in the workspace distribution: the right and left hand's areas are well defined and distinct, partially overlapping with the foot motion region. The workspace distribution in the three-coupled task recalls the triangle shape of the elastic band connecting the three cursors; the three areas covered by the right hand, left hand and foot motion, respectively, are separated and organized in a triangle shape with the foot at the top corner, as in the task representation (Fig. 5.20 AB session). Only subject 12 revealed a different behavior: the subject switched the right and left hand's workspaces, keeping the virtual left cursor on the right side of the screen and the virtual right hand cursor on the left side of the screen (Fig. 5.20 BA session). This unconventional behavior is evident in the three-coupled task, where the subject changed the original triangle shape moving the foot from the top to one side or bottom corner. Even though the triangle corners position vary among the trials, the subject kept the same strategy for the whole trial duration.

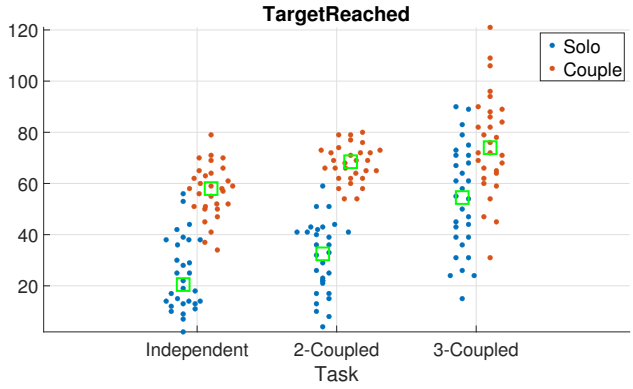

Fig. 5.6 Target Reached for Task 1, Task 2 and Task 3. Each dot represents the value of the last trial. Blue dots correspond to solo sessions; red dots correspond to paired sessions.

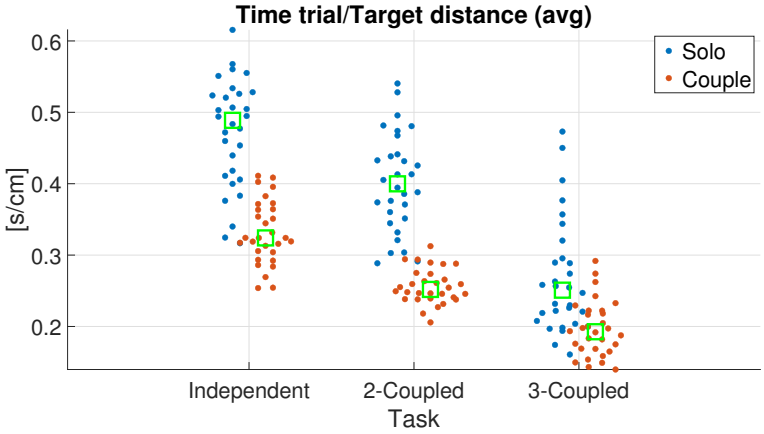

Fig. 5.7 Time needed to reach the targets divided by the number of total targets, for Task 1, Task 2 and Task 3. Each dot represents the value of the last trial. Blue dots correspond to solo sessions; red dots correspond to paired sessions.

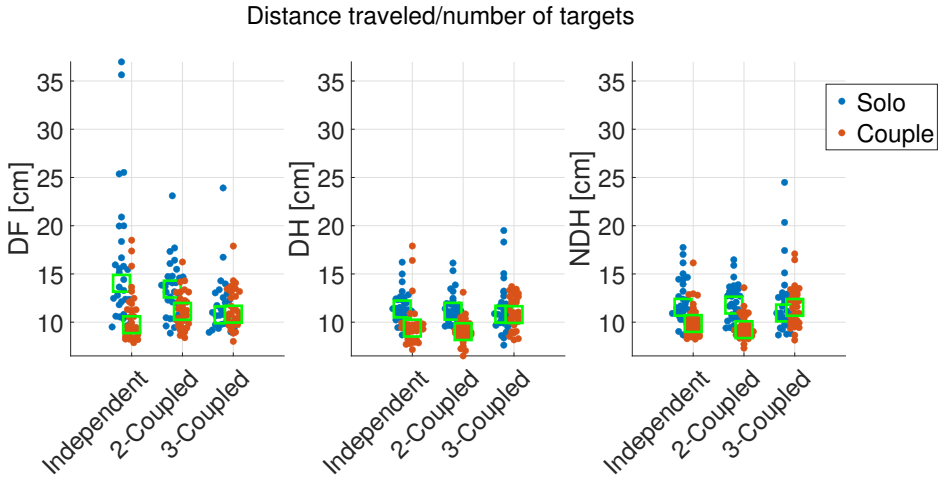

Fig. 5.8 Distance traveled by the limbs (DF-Dominant Foot, DH-Dominant Hand and NDH-Non-Domimant Hand) divided by the number of total targets, for Task 1, Task 2 and Task 3. Each dot represents the value of the last trial. Blue dots correspond to solo sessions; red dots correspond to paired sessions.

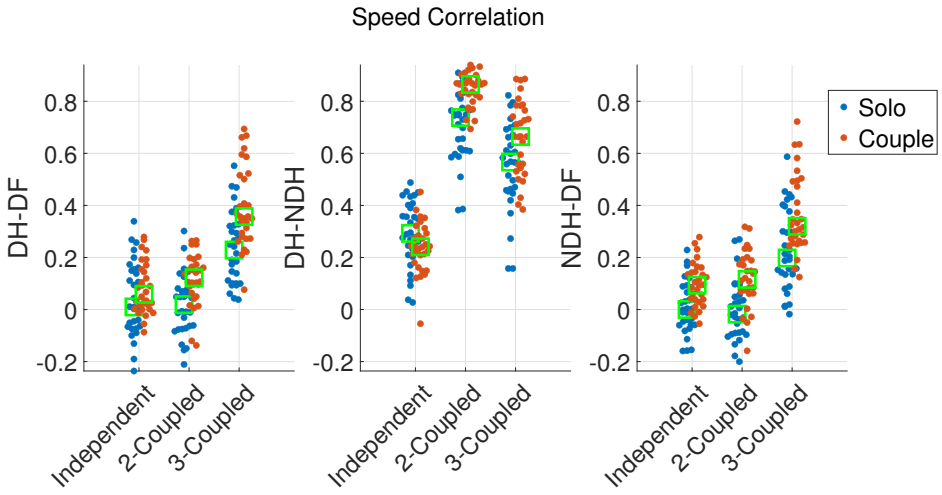

Fig. 5.9 Correlation of limb's speed between dominant and non-dominant hand and each hand and the foot, for Task 1, Task 2 and Task 3 (DF-Dominant Foot, DH-Dominant Hand and NDH-Non-Domimant Hand). Each dot represents the value of the last trial. Blue dots correspond to solo sessions; red dots correspond to paired sessions.

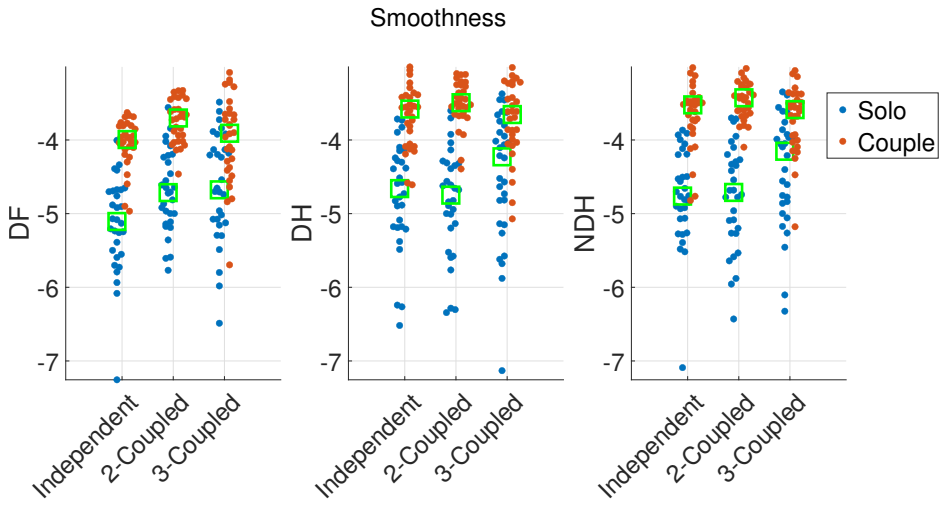

Fig. 5.10 Limb's Smoothness (spectral arc length) for Task 1, Task 2 and Task 3 (DF-Dominant Foot, DH-Dominant Hand and NDH-Non-Domimant Hand). Each dot represents the value of the last trial. Blue dots correspond to solo sessions; red dots correspond to paired sessions.

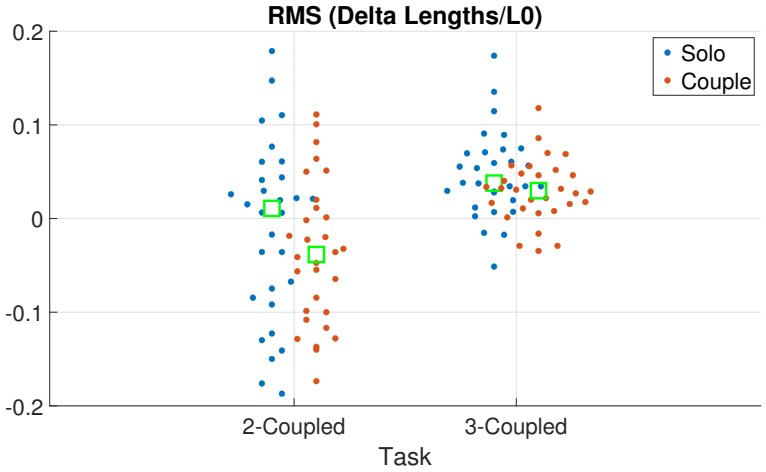

Fig. 5.11 Spring length variation (L/L0) for Task 2 and Task 3. Each dot represents the value of the last trial. Blue dots correspond to solo sessions; red dots correspond to paired sessions.

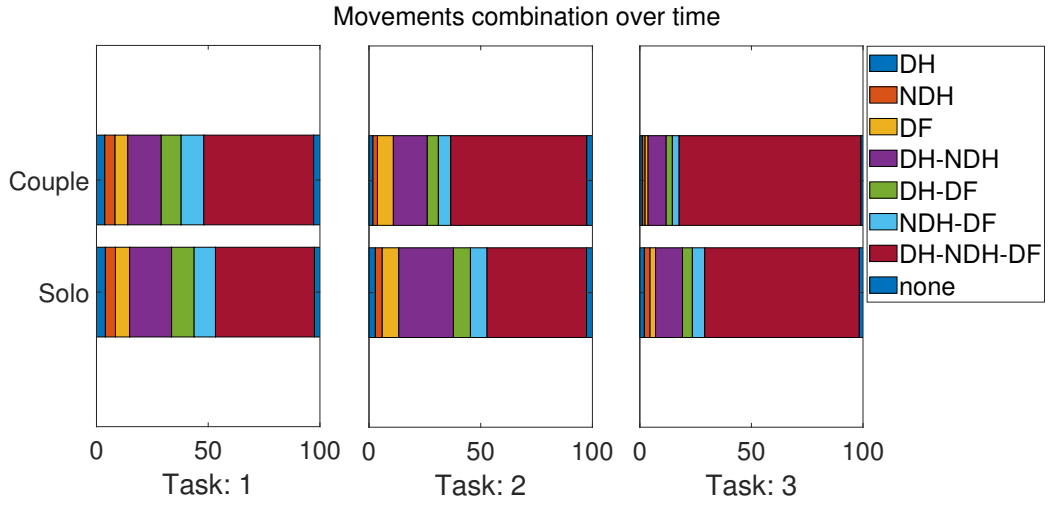

Fig. 5.12 Time percentage of simultaneous movements for Task 1, Task 2 and Task 3. The top raw correspond to the paired sessions, the bottom one to the solo sessions.

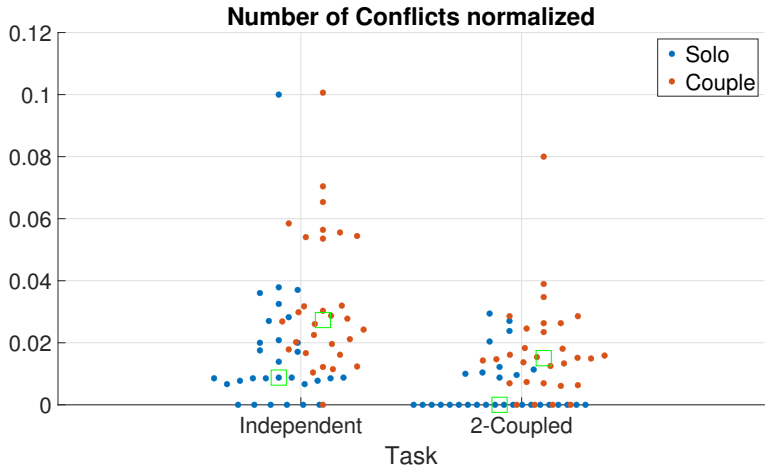

Fig. 5.13 Number of conflicts divided by the number of total targets and the number of cursors that can collide, for Task 1 and Task 2.Each dot represents the value of the last trial. Blue dots correspond to solo sessions; red dots correspond to paired sessions.

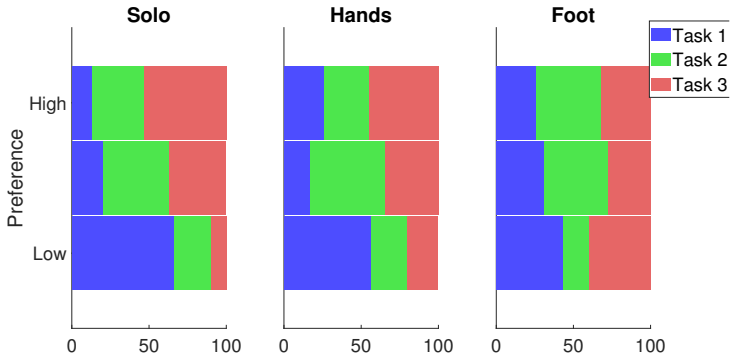

Fig. 5.14 Questionnaire results: Preference rank among the tasks for the Solo and paired (hands-foot) sessions.

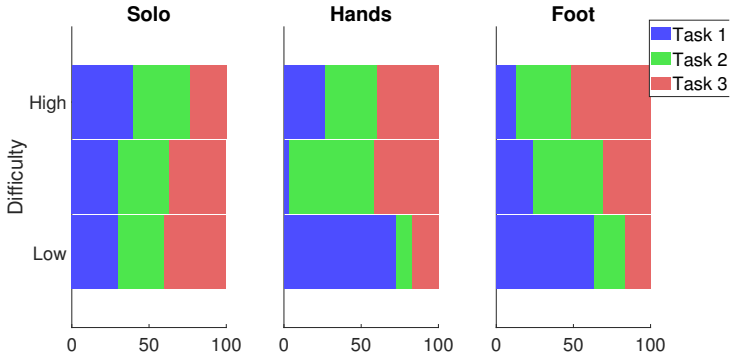

Fig. 5.15 Questionnaire results: Difficulty rank among the tasks for the Solo and paired (hands-foot) sessions.

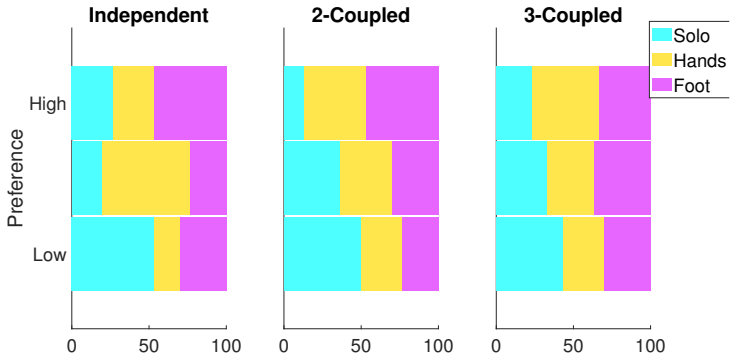

Fig. 5.16 Questionnaire results: Preference rank among the sessions for the three tasks.

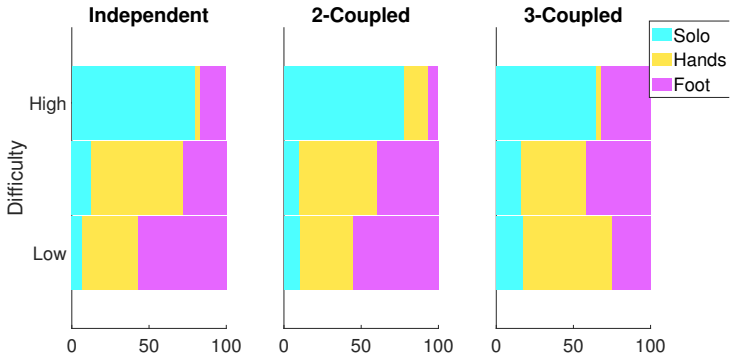

Fig. 5.17 Questionnaire results: Difficulty rank among the sessions for the three tasks.

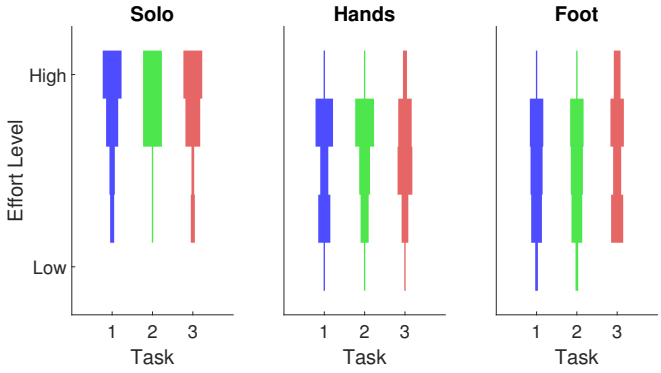

Fig. 5.18 Questionnaire results: Perceived effort rank among the tasks for the Solo and paired (hands-foot) sessions.

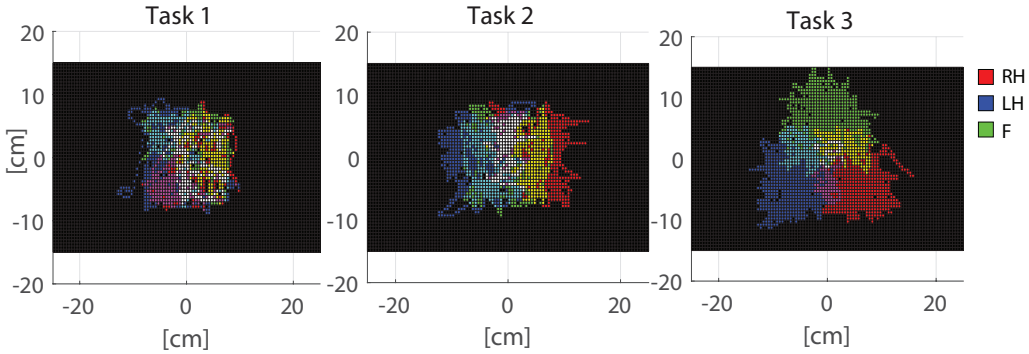

Fig. 5.19 Example of Workspace distribution for Right hand, Left hand and Foot movements in Task 1,2 and 3 in paired Session.

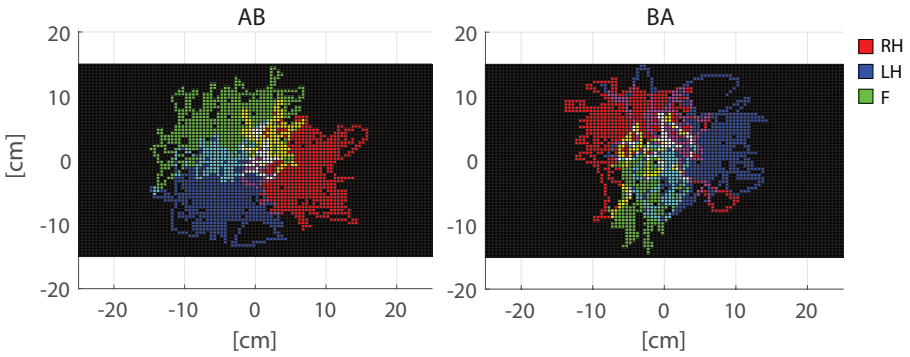

Fig. 5.20 Workspace distribution for Right hand, Left hand and Foot movements in Task 3 -last trial- for subjects 11 and 12 in the paired Session. AB: subject 11 controls the hands and subject 12 the foot; BA: subject 12 controls the hands and subject 11 the foot.

5.7 Discussion

Regardless to the task comparison, most measures exhibited better performance for people working in a dyad rather than alone. Regarding the distance traveled by the virtual cursors, the different scaling used for the hands and for the foot could have affected this result but does not change the difference between solo and couple. This means that dyads move the cursors in a target oriented motion more than solo subjects and are more inclined to exploring and failing movements.

Furthermore the results show that people controlling three limbs perform better in the 3-coupled task than in the others. This may be due to the mental load: the 3-coupled task requires to focus on one goal at a time (one target). This requires a mental effort lower than solving two or three sub-tasks at the same time. The mechanical coupling, that requires much more coordination than the other tasks, seems to have less effect with respect to mental load related to the task.

The speed correlation results confirmed an expected behavior: the more the limbs are coupled together, the more their movements are correlated. What is unexpected is the higher correlation in dyads than in solo subjects. While this could be reasonable in the 2-coupled task because of the mental load -one person focusing at the same time on two different sub-tasks can lose the hands coordination while controlling the foot- is unexpected in the three-coupled task. The smoothness results are coherent with the lower dexterity of the foot compared to the hands, eventually increased by the different scaling factor. We expected one person to coordinate better the three hands than two people not allowed to communicate to each other; indeed coordination requires a common motion strategy, that is difficult to be

commonly established due to the forbidden communication (this happens also in surgery [102]). On the contrary, dyads perform better than solo even in term of coordination.
Regarding the spring lengths variation, the worse performance revealed in Task 3 are obtained comparing the average variations of all the three springs (connecting the two hands and each hand with the foot). This overall value could have hidden the differences due to the foot behavior (Fig. 5.11).
The workspace distribution of the limb's movements is a qualitative result, but well conveys the tasks definition: indeed, looking at figure 5.19 it is possible to identify if there was a mechanical coupling between the limbs and which ones were constrained.
The people preference of working in dyads rather than alone fits with the performance results and can be explained by the highest effort level required to perform the task alone. The perception of the foot control as more difficult the more the task is independent, can be explained by the need of keep the coordination between the foot and the other cursors.
Summing up, the aim of this study was to understand on one hand if people are able to reliably perform three-hands tasks and how their performance vary across different scenarios; on the other hand if demanding the control of three limbs to one person leads to better or worse performance than sharing the limbs control between two subjects and if the results vary with different tasks. The results show that people are able to perform three-hands tasks (since they completed all the tasks with good performance) and they achieved the best performance in the task with one objective and a mechanical constraints among the three limbs. The mechanical coupling indeed helps the coordination and the motion of the limbs in parallel.
Moreover, two people working together achieved better results than people working alone almost in every respect. This represents a converse founding compared to the surgery studies results [101]. However, the surgery operations, as well as the required accuracy, are much more demanding and specific compared to the ones required in the present tasks. This could have made the difference in the comparison between solo and paired sessions performance. In fact, in the present study also smoothness and speed limbs correlation are higher for dyads than solo subjects, suggesting that -at least in the examined tasks- one person is less able to move three limbs in parallel than to coordinate with another person.
Further studies will investigate tasks that require higher accuracy and that present different combination of mechanical coupling and sub-tasks, e.g. splitting the mechanical coupling and the unique goal of Task 3 in two different tasks, to understand which aspect is more affecting the results.

Chapter 6

2dof Control using High Density EMG grid on the leg

This chapter focuses on the development of an EMG-based interface to control a supernumerary limb in augmentation tasks. Chapter 5 presented the analysis of human performance in three-hands tasks; that study focused on the tasks and protocol constraints, employing the same position control device on the participants' hands and the foot. As stated earlier, the main requirement for a third-arm control interface is to be intuitive and to not affect the users' performance in the task. Here, we want to develop an EMG control interface to control a supernumerary limb in three-hands tasks in a more intuitive way.

6.1 Background

The increasing development of supernumerary limbs (SLs) opens several new possibilities, making humans able to perform tasks otherwise not possible.
The systems proposed so far are mainly wearable robots, either not-actuated or fully autonomous [104]. Most of those devices are limited to specialized tasks and several of them are controlled using the motion of other limbs [110].
However, to make the use of the extra limb an actual advantage, not interfering with the normal skills, we need to minimize the cognitive and physical effort needed to control the tool, not interfering with the natural limb movements. Arguably, a control strategy similar to the human's one should achieve better performance when the supernumerary limb closely interact with the natural ones [4]. An EMG-based control meets all those requirements. The EMG interface can be placed in different body regions, not interfering with the natural arm movements and with the possibility to control many degrees of freedom. Also, it may allow

regulating the impedance of the extra limb through muscle cocontraction, in the same way the brain does with natural limbs.
In literature there are several studies on EMG control interfaces, particularly for prostheses [111]. Most of those controls are based on pattern recognition, that however prevents the possibility of combined movements [112], [113]. Conversely, we aim to develop an interface that allows to achieve a control the more intuitive and close to the natural one as possible, so that the user can move the third arm without losing their focus on other task, as while biking or driving. For this reason we selected a regression approach to identify from the EMG signal the amount of all the engaged degree of freedom.
High Density EMG grids well suits to control several degrees of freedom, although in the present study we downsized the complexity of the problem using only 2 dofs.
In the perspective of a three-hands task involving the two arms plus the supernumerary limb, we placed the interface on the foot, using the leg muscles involved in the ankle joint motions. This choice permits indeed a direct comparison with previous works that employed the foot as third arm in trimanual tasks [107], [114], [102], [106]. Then, further studies would address the localization of the optimal target muscles and body region to place the interface.

6.2 Methods

The use of High Density EMG grids (provided by OT Bioelettronica s.r.l.), besides the possibilities to extend the control to many degrees of freedom, permits also to have a robust and reliable setup. Indeed, the high number of channels on each grid allows to achieve a good signal from the desired muscles even with a "rougher" placement of the electrodes; on the other side the high density of electrodes leads to a robust control, given the inherent redundancy of signals from the same muscle.
Deeper studying the ankle joint movements, the dorsiflexion/plantarflexion and the inversion/eversion seem to be the best candidates for our 2 dof control (see Fig. 6.1).

Hence, the muscles mainly responsible for those movements are the tibialis anterior and the gastrocnemius lateral and medial heads, all easily accessible for the surface electrode positioning [115].
In order to achieve an intuitive and robust control, we adapted to our setup a proportional myoelectric control previously proposed for the upper limb [116]. The control is based on the non-negative matrix factorization approach, described hereafter [117].

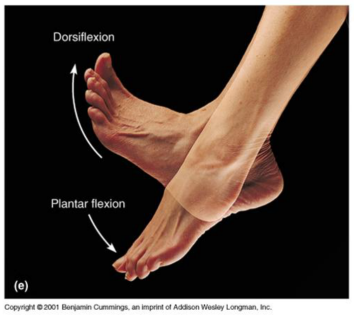

Fig. 6.1 Ankle joint movement used for the 2DoF control: a) Dorsiflexion-Plantarflexion; b) Inversion-Eversion.

6.2.1 NNMF

The advantage of the factorization is the feasibility to compute the synergy matrix without any kinematic reference or sample-by-sample labeled data. The algorithm is based on the representation of the surface EMG data as the product between a synergy matrix and a control signal:

$$Z(t) = W \cdot C(t) \tag{6.1}$$

where $Z(t)$ is the vector of elaborated EMG signal of the N electrode signals; W is the Nx2M synergy matrix and $C(t)$ is the 2M vector of control signals, with M number of dof [117]. The right part of Eq. 6.1 is unknown, but we can treat all the elements as non negative. With this non-negative assumption, the control signal of each DoF can be represented through two non negative components: c_i^p for the positive direction and c_i^n for the negative one. Equation 6.1 becomes:

$$[\ z_1(t), z_2(t), \ldots z_N(t)\ ] = [W_1^p, W_1^n, \ldots W_M^p, W_M^n] \cdot \begin{bmatrix} c_1^p(t) \\ c_1^n(t) \\ \ldots \\ c_M^p(t) \\ c_M^n(t) \end{bmatrix} \tag{6.2}$$

At this point we still have infinite solutions to the equation above. It is possible to limit the number of solutions to only one using a specific experimental protocol. This means to perform calibration stages considering one DoF at a time. Hence, if only the ith DoF is activated, all the elements in the control vector $C(t)$ should be zero but the ones related to

that DoF, i.e. c_i^p and c_i^n. Equation 6.2 can be reduced to:

$$Z_{[i]}(t) = [W_i^p, W_i^n] \cdot \begin{bmatrix} c_i^p(t) \\ c_i^n(t) \end{bmatrix} \tag{6.3}$$

$Z_{[i]}$ is the EMG signals vector related to the activation of the ith DOF.
Thanks to this approach, the synergy matrix W can be computed on a DOF-wise fashion, column by column.
To make the algorithm even more robust, a number of NNMF algorithms can be concatenated, using the output of the first iteration as input of the second one, and so on. This concatenation is called multilayer NNMF procedure. The number of iterations needed to achieve optimal results was estimated through preliminary tests.

6.2.2 Calibration

The calibration is a crucial phase to achieve good results, given the chosen factorization method. As above explained, we need to record the EMG signal selectively activating each DoF.
During the calibration the subject is asked to move the foot in the positive direction of the first DoF, to keep that position for 3 seconds and then to return to the neutral pose. This movement is repeated 5 times for the positive direction and 5 times for the negative one. The separation of the positive and negative movements, with a pause in the neutral pose, is just a good practice to record a clear signal and improve the regression outcomes, since the signal is recorded and elaborated as a single trace corresponding to one degree of freedom. Then the procedure is repeated for all the other DoF. At the end 5 seconds of resting are acquired; the subject is asked to be relaxed, to avoid any muscle contraction.
The output of this initial stage is one N-channels EMG signal per Dof plus one N-channels resting signal.
The rest signal is used as threshold to segment the other signals, removing the part corresponding to the neutral pose. The resulting signal corresponds to the emg activation both during the movement and during static position at the maximum range of motion values. The movement part is included in the signal used to calibrate the NNMF algorithm, since it represents the dynamic part that will occur even during the control.
Once the signal has been segmented, it can be used to compute the synergy matrix.

6.2.3 Control

Through the inverse model, the control signal $C(t)$ can be estimated:

$$C(t) = W^{\dagger} \cdot Z(t) \tag{6.4}$$

where $W^{\dagger}$ is the pseudo-inverse of the synergy matrix and it is computed using the Moore-Penrose formula:

$$W^{\dagger} = (W^T W)^{-1} W^T \tag{6.5}$$

In the present case, using 2 DoF, the control signal $C(t)$ is a 4x1 vector composed of the positive and negative component of each DoF, as defined in Eq. 6.2. To obtain the final signals, the positive and negative elements are combined as follow:

$$\begin{aligned} c_1(t) &= \tau_{11} \cdot c_1^p(t) - \tau_{12} \cdot c_1^n(t) \\ c_2(t) &= \tau_{21} \cdot c_2^p(t) - \tau_{22} \cdot c_2^n(t) \end{aligned} \tag{6.6}$$

where τ_{ij} are scalar factors used to match the range and the direction of joint angles in the respective DoF. Their values are estimated at the end of the calibration phase, asking the subject to move at the limits of the selected degrees of freedom and recording the computed control value. τ_{ij} is set to obtain $c = 1$ at the dof extremities.

Finally, the estimated is signal is employed in a proportional velocity control:

$$v(t) = \frac{c_M(t)}{c_{max}} v_{max} \tag{6.7}$$

where $v(t)$ is the output velocity, $c_M(t)$ is the mean of the control signal over 62.5 ms, c_{max} is a percentage of the maximum control value reached during the calibration phase and v_{max} is the maximum allowed velocity, arbitrary set.
Equation 6.7 is valid only if $c_M(t)$ is included in the range $c_{min} \div c_{max}$, otherwise:

$$\begin{aligned} if \quad c_M(t) <= c_{min}, \quad v(t) = 0; \\ if \quad c_M(t) >= c_{max}, \quad v(t) = v_{max}. \end{aligned} \tag{6.8}$$

The limit values for the control signal, c_{min} and c_{max}, are computed as 0.1 and 0.9 times the maximum value recorded during the calibration stage.

6.2.4 Experimental protocol

The presented control approach has been developed to control a third arm in a trimanual task. The application previously implemented for 2D trimanual tasks (see section 5.1) has been adapted to get the third arm (i.e. foot) input from the emg control here presented.
The control was validated on the training session -the first stage of the trimanual experiment that aims to let the subject be confident with the control, moving one arm at a time. In this case the training was focused on the foot only.
The task consists in a 2D reaching task: the subject controls the virtual foot movement by means of his own foot; he has to reach with the virtual foot the target that appears on the screen. There is a maximum time to reach each target before it disappears and a new target pop-up. The target positions are random in a squared window on the screen. The subject has 150 seconds to catch as many targets as possible.
The performance are measured with the following parameters:

- Score: number of target reached
- Trial time: the average time needed to catch one target

The trial time $\bar{t}$ was also normalized by the maximum time allowed to reach each target t_{max} and by the distance d_i from the target:

$$\bar{t} = \frac{1}{N_t} \sum_{i=1}^{N_t} \left(\frac{t_i}{t_{max} \cdot d_i} \right) \tag{6.9}$$

with N_t number of trials.

6.3 Experimental Setup

Three High Density EMG grids (GR10MM0808 by OT Bioelettronica s.r.l.) were used. Each grid has 64 channels organized in a 8x8 matrix, equally spaced each 10 mm. Conductive cream was spread on electrodes by means of a foam layer, which was provided with an adhesive surface to be fix on the skin. Each electrode matrix was connected to an AD64 adapter (by OT Bioelettronica s.r.l.), in turn connected to the EMG-USB2+ amplifier by means of a flat cable. The amplifier gain was set to 500.
The signal was recorded online on Matlab 2017a, using the OT Comm libraries, with a sampling frequency of 2048 Hz. The EMG signal was online processed with a 4th order band-pass filter between 20 Hz and 500 Hz and then enveloped with a RMS each 125 ms (see Fig. 6.2).

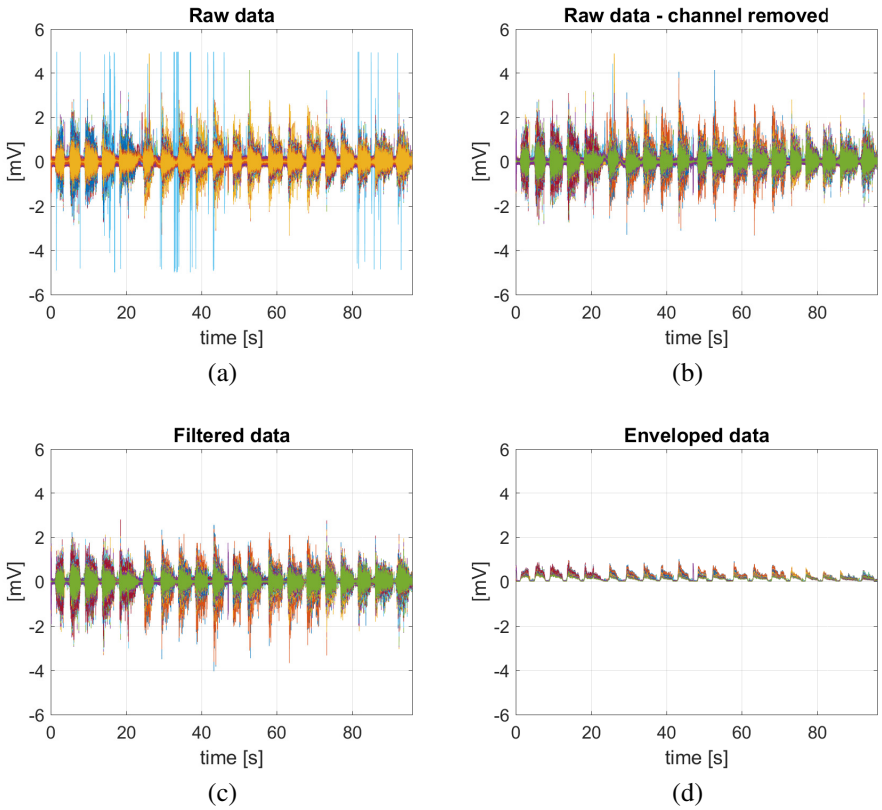

Fig. 6.2 EMG signal processing: a) Raw data; b) Raw data without noisy channels, removed after visual inspection on the raw signal; c) Data filtered with a 4th order band-pass filter between 20 Hz and 500 Hz; d) Signal enveloped using RMS on a 125 ms window.

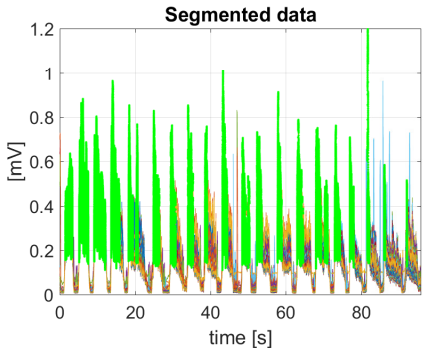

Fig. 6.3 EMG processed signal recorded during the calibration phase. The rest signal is used as threshold to discard the neutral pose contribute. The resultant segmented signal is highlighted in green.

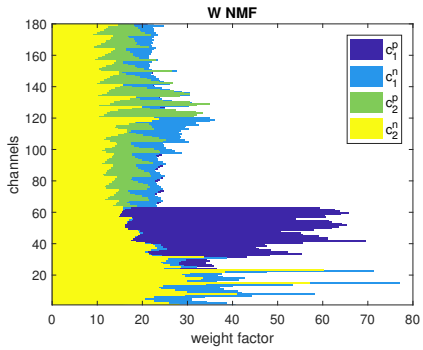

Fig. 6.4 Sinergy matrix W computed from the non-negative matrix factorization.

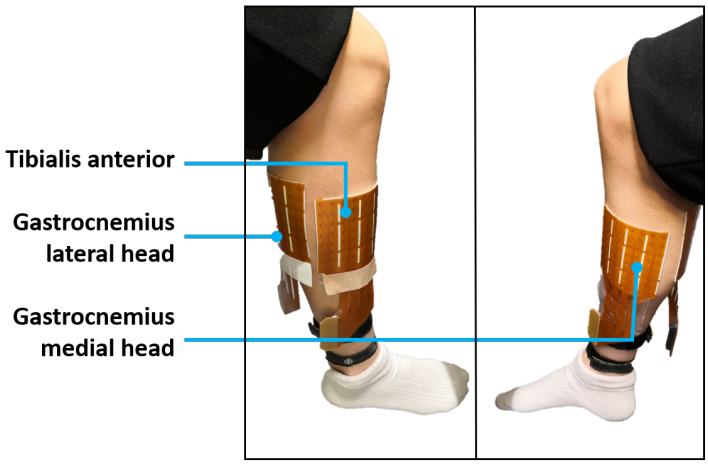

Fig. 6.5 High density emg matrices positioning on the tibialis anterior, gastrocnemius lateral head and gastrocnemius medial head.

After the calibration signals have been recorded, the noisy channels - identified as the ones with signals flat or orders of magnitude higher than the surrounding channels- were removed by visual inspection of the raw emg signal. The signal was then segmented to discard the rest contribute (Fi. 6.3); the resultant signal was used to compute the synergy matrix using the nnmf Matlab function nested 100 times (see Fig. 6.4).
The matrices were placed on the tibialis anterior, gastrocnemius lateral head and gastrocnemius medial head (see Fig. 6.5).

All the matrices were connected to a common reference placed on the ankle using a wet band. The subject reference, i.e. the ground reference, was connected to the ankle using another wet band, more distal with respect to the common reference (see Fig. 6.6). The two bands did not touch each other.
The subject was seated on a high chair, having the foot floating, not touching the floor. After preliminary tests, this experimental setup was found as the best to record clear signals

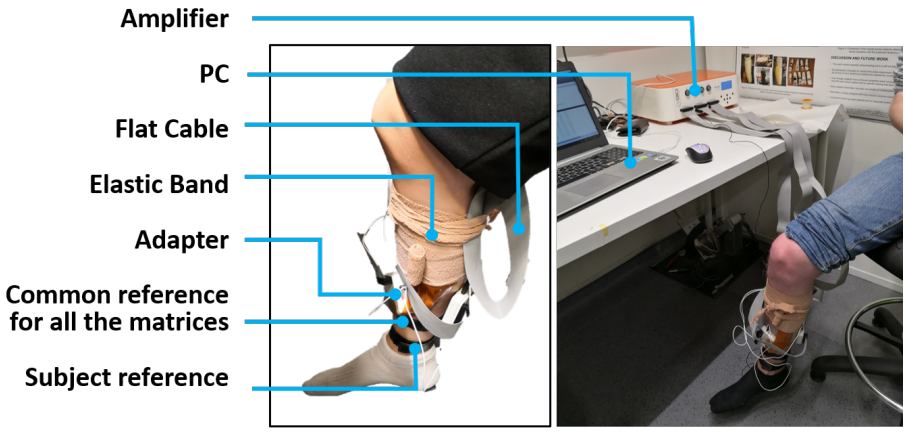

Fig. 6.6 Experimental setup: The subject is seated on a high chair; three high density EMG matrices are placed on the subject's leg; each matrix is connected to the amplifier through an adapter and a flat cable; an elastic band wrapped around the matrices and the flat cables helps keeping the elements fixed on leg; two wet bands on the ankle are connected to the common and ground references; the amplifier is connected to the pc where the experimental application runs.

performing all the movements, in particular as regards the plantar-flexion movement.
The control was first tested in Matlab 2017a and then the experimental protocol was run using a 2D game developed on Unity3D platform.
The calibration was run offline in Matlab, even though the signal was acquired and processed online. Once the synergy matrix has been computed, the emg signal was acquired and processed online using Matlab, then converted into a control signal (i.e. velocity) and sent through UDP communication to the final application developed in Unity.
Into the application the velocity data was used to move the foot cursor on the screen. One subject was tested, performing one calibration phase and three task trials.

6.4 Results

Results showed that after 3 training sessions the subject learned the control, increasing his performance.
The score increases with sessions, while the average time needed to catch the targets decreases with sessions (Fig. 6.7). The same trend is visible even looking at the normalized time. This means that the performance is improving regardless to the difficulty of the trial.

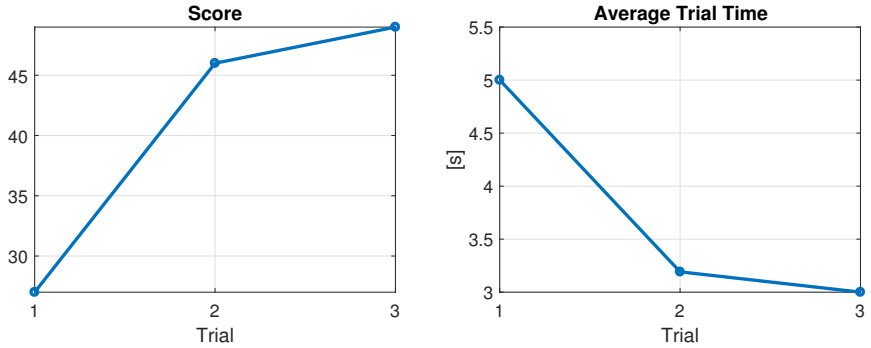

(a)

(b)

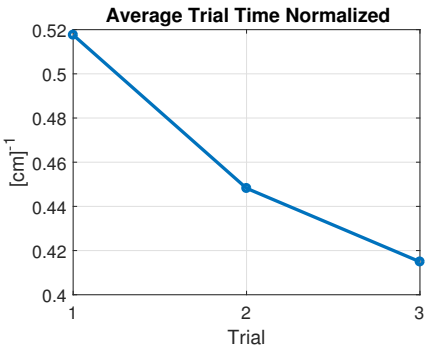

(c)

Fig. 6.7 a) Score performed by the subject in three following trials. One score point corresponds to one target reached; b) Average time needed to catch a single target, during three following trials; c) Average time needed to catch a single target, divided by the maximum allowed time and the distance from the target, over three following trials.

6.5 Discussion

The experimental validation, although it was conducted on one subject only, assessed the efficacy of the control and its easiness.
Thanks to high number of electrodes, the control results robust and reliable, both in term of setup and in term of outcomes. The high emg density allows to achieve a good calibration with only 5 repetitions per DoF. This avoids to waist time and also to tire the subject, possibly compromising his performance.
Moreover, given the selected DoF and muscles, the high density of electrodes leads to an intrinsic redundancy of the signal, improving the robustness of the control output.

Further works should test more subjects and compare the trimanual tasks performance using the kinematic or the emg control. Moreover, future perspectives could address how providing a proprioceptive feedback affects the performance in the control of a third arm (in this case a virtual foot controlled using the real foot by means of emg signals).

Chapter 7

A Novel Proprioceptive Feedback System for Supernumerary Robotic Limb

This chapter focuses on the other aspect of supernumerary limb control, i.e. the feedback needed to close the control loop and establish a bi-directional communication. In particular the author proposes here the development and validation of a vibrotactile interface to provide proprioceptive feedback of a supernumerary robotic arm, investigating two different strategies to convey the robot state.

7.1 Background

Researchers and artists have investigated the human and robot integration for generations. Robotic devices have been used not only for replacing lost limbs or overcoming disabilities, but also for enhancing physical performance [118]. This augmentation concept was early presented by the artist Stelarc, which controlled an additional body-worn robotic hand in his work "Third Hand" [119].
Recently, that idea has captured researchers' attention and Supernumerary Robotics Limbs (SRL) have became a new research area in the field of human robotics [6]. The SRL prototypes presented so far are mainly designed to help users in manual works, supporting the human body and minimizing the human load [120], [121], thus allowing to perform tasks safely and stably while the robotic system sustains the user's body by leaning against walls and surrounding structures [122]. These systems are characterized by a task-oriented and wearable design and the robotic devices present at most six degrees of freedom (dof).
A debated aspect of this topic is the integration of the SRL system into the body schema. Indeed, it is demonstrated that integrating non-corporeal objects into the existing body

schema increases the intuitiveness in their control [123]. Beside trying to emulate human's arm shape and dynamics [124], little effort has been put into research and implementation of other factors favoring SRL embodiment, such as a closed loop control.
Establishing a bi-directional communication through the addition of a sensory feedback could allow to close the control loop and achieve a better human-robot interaction (see Fig. 7.1). Some studies investigated the role of the sensory feedback in improving the control of external tools, demonstrating an increase in accuracy during visuospatial reaching and stabilization task. In the absence of visual feedback, supplemental vibrotactile stimulation induced improvement of motor learning compared to normal proprioception [125], [126], [127]. Along this line few attempts have already been tested in SRL, such as a wearable feet-controlled double arms system relying on haptic feedback related to the grasping force [104].

However, to favor the adaptation of the body schema and consequently the robot control, it might be relevant to convey to the user also the position of the robot in the space, before its potential interaction force.
The human brain estimates the position of the body through both visual and proprioceptive information. The latter becomes especially important in the depth direction where the estimate relies more on proprioception than on vision [128]. Rich proprioceptive feedback may also relieve the user from focusing their gaze continuously on the robot. Nevertheless, as far as we know, there are no studies that tried to implement proprioceptive feedback for a supernumerary robotic arm.

In this chapter we present the development and validation of a system to inform the user about the posture of a supernumerary robotic arm. Proprioceptive feedback was provided through a vibrotactile stimulation device, hereafter called ViPro.

7.2 Materials and Methods

7.2.1 System Design

Vibrotactile stimulation was chosen among several possible stimulations because it is a non-invasive, low-cost and widely investigated solution [129]. To control up to eight pairs of eccentric motors (Model: 307-103 by Precision Microdrives Inc.), we designed a Printed Circuit Board, which drives the stimulation on the basis of the sensory data read in real time by the robot.
In the present validation, we employed only two pairs vibrators. Each couple of vibrators refers to a single dof and, within the couple, one vibrator is used to represent positive encoded

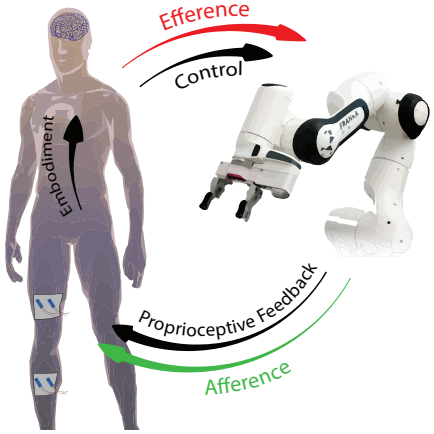

Fig. 7.1 SRL loop scheme: the robot control represents the efferent part (red); the proprioceptive feedback represents the afferent part (green) required to close the loop. Vibrotactile stimulation can be used to provide the feedback through vibrators placed on the human skin. The sensory feedback also improves the SRL embodiment in the body schema.

values and the other one to convey negative values. The logical schematic of the ViPro board is presented in Fig. 7.2. The frequency and the vibration intensity of the stimulators are coupled, and they are controlled by the embedded micrcontroller (STM32F446 by STMicroelectronics Inc.), which generates a Pulse Width Modulation (PWM) signal in order to define the supply voltage of the vibrators according to the following relationship:

$$V_i(t) = \frac{\delta_i(t)}{T} V_A, \tag{7.1}$$

in which T is the period of the PWM signal and it is equal to 1 ms, while V_A is the maximal supply voltage of the vibrators and it is equal to 3.6 V. The parameter $\delta_i(t)$ is the duty cycle of the vibrators control signal (computed for each i dof considered) which is proportional to the specific information provided to the user. The δ range of variation depends on the type of feedback implemented. Thus, to summarize, the amplitude of the stimulator is proportional to the robot state information to be provided.

Since the robot represents an additional arm to be used in three-handed manipulation tasks [106], we opted to place the feedback device on the subject's leg which is not involved in the task, in order not to contaminate the natural proprioceptive feedback coming from the arms.

We studied a planar task involving two degrees of freedom (and consequently two joints of the robot) to reduce the complexity of the problem in a preliminary study.
We placed the vibrators distant enough from the bones and from each other so that the user could easily identify which motors are vibrating and clearly perceive the vibration amplitude;

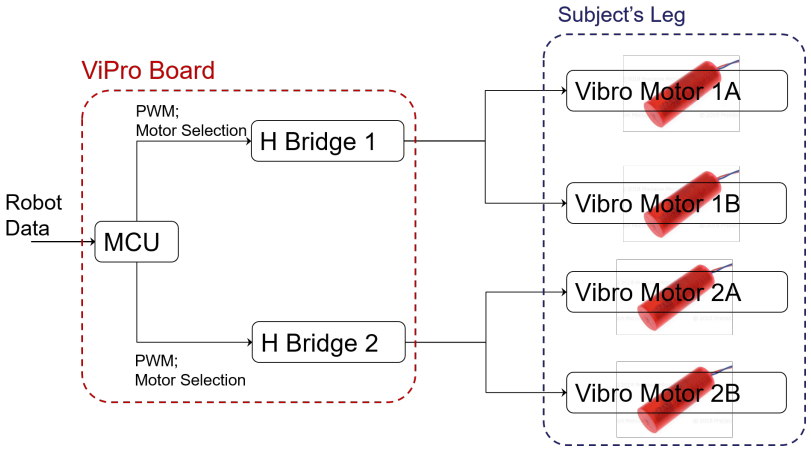

Fig. 7.2 Logical Schematic of the ViPro system for two couples of motors. The instantaneous supply voltage of the vibrators, thus their vibration, is controlled by the MCU through two independent motor drivers (L293DD by STMicroelectronics Inc.). Each motor driver refers to a dof and controls a couple of vibrators. Then, according to the sign of the information to be provided, the MCU selects which one of the two vibrators has to be turned on (A for positive values and B for negative ones).

this resulted in placing one couple of motors on the vastus lateralis (1A) and the biceps femoris (1B), and the other one on the gastrocnemius lateralis (2A) and medialis (2B) (see Fig. 7.3). In both cases, motors labeled with A refer to positive values of the feedback, while the ones labeled with B refer to negative values.

7.2.2 Feedback Approaches

The sensory feedback has been investigated in many studies, encoding different information, such as the device end-point position, the joint velocity, the interaction force, the error meant

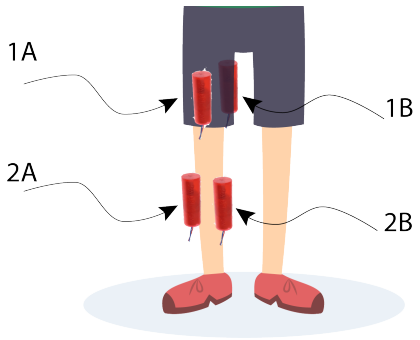

Fig. 7.3 Eccentric motor placement on the subject's leg: 1A) Vastus lateralis; 1B) Biceps Femoris; 2A) Gastrocnemius lateralis; 2B) Gastrocnemius medialis

as the distance from the target position, etc., but none of these studies involved SRL [126], [130], [131].
To perform a preliminary validation of the system, we selected two different approaches to represent the robot state: a kinematic approach and a dynamic one. The first method represents the state of the robot as the position of the robot end-effector in the workspace, expressed in the cartesian space (i.e. (x_{EE}, y_{EE}) in Fig. 7.4); whereas the latter conveys the torques which are applied to the active joints of the robot (i.e. J_2 and J_4 in Fig. 7.4).
We expected the kinematic approach to be the easiest to understand, since it is a linear mapping; conversely, the dynamic one requires the learning of a non-linear mapping to understand the feedforward model of the robotic arm, but may perform better in case of external disturbs such as obstacles or force fields.

Referring to the motor placement (Fig. 7.3), motors 1A-1B drive the x_{EE} value and motors 2A-2B the y_{EE} information, in case the kinematic approach is used; otherwise, if the dynamic method is employed, J_2 value is driven by the motors couple 1A-1B and J_4 by the couple 2A-2B.

7.3 Experimental Validation

7.3.1 Experimental Setup

A 7 dof robotic manipulator, the Panda robot by Franka Emika GmbH, is used as SRL. Only two robot dof (second and fourth joint) are enabled (see section 7.2.1). The robot is controlled through an interface developed in c++ language, using the Qt libraries, running on a computer with Ubuntu 16.04 O.S.
The robot moves the end-effector on a plane, 30 cm above a table. Robot motions are planned to be human-like, i.e. implementing minimum jerk trajectories. In particular, each movement from the center point to the target one has a linear path and the same duration, i.e. four seconds.

The workspace consists of a 30 cm x 50 cm rectangle upon a table, clearly highlighted with adhesive tape.

As shown in Fig. 7.4 and Fig. 7.5, the subject is seated on a chair in front of the robot, close enough to the table to comfortably reach with the hand every point of the workspace. Subject's right shoulder is aligned with the center of the workspace. Twenty equally-spaced points within the workspace represent the target positions (blue dots in Fig. 7.4).
Subjects and robot move on two parallel planes so that they do not collide. The subject moves his arm onto the table's plane, holding a plastic handle with spherical wheels, whereas

the robot moves onto an upper plane (Fig. 7.5). To ensure planar movements, the subject is asked to keep his back close to the chair and the handle touching the table during the whole experiment.
A Polaris Vicra Camera (by Northern Digital Incorporated) was used to detect the position of the end-effector and the subject's hand, using passive reflective markers attached to the robot and the plastic handle.
The robot end-effector is provided with an additional handle to simplify the placement of the motion tracking markers. The infrared camera is placed sideways so that it has both markers within its field of view (see Fig. 7.4).
The vibrators are manually placed on the subject's right leg, as show in Fig. 7.3, adjusting their position so that the subject can clearly perceive the full frequency range of the stimulation and easily discriminate which vibrator is delivering the stimulation [132].

7.3.2 Experimental Protocol

Three subjects (two right-handed and one left-handed, aged from 23 to 25 years old) naive to the aim of the study, were recruited to run a pilot experiment in order to validate the system.

The robot performs planar movements starting from the center of the workspace (highlighted with the red dot in Fig. 7.4). While the robot is moving the subject receives the vibrotactile stimulation and, after the robot movement, subject is asked to move the handle on the table, reaching the same in-plane position of the robot end-effector. No cue on the feedback encoding or how it was mapped on the motors was given to the subject. To be able to assess even subtle advantages given by the proprioceptive feedback, subjects executed the task blindfolded. Ear muffs and eye mask were used to suppress auditory and visual feedback.
The experimental protocol was composed of three phases (see Fig. 7.6): i) Familiarization; ii) Learning; iii) Test. Each subject performed the two conditions (type of feedback), in a randomized order in two different days.

The protocol steps are described as follow:

Familiarization

The familiarization phase allows the subject to understand the task. During this phase the subject has a visual feedback (not wearing eye mask), but no vibrotactile feedback is given. The robot reaches five random points in the workspace. At the end of each robot movement, the subject is asked to move the handle on the table, reach the in-plane position of the end-effector and then return to the starting position.

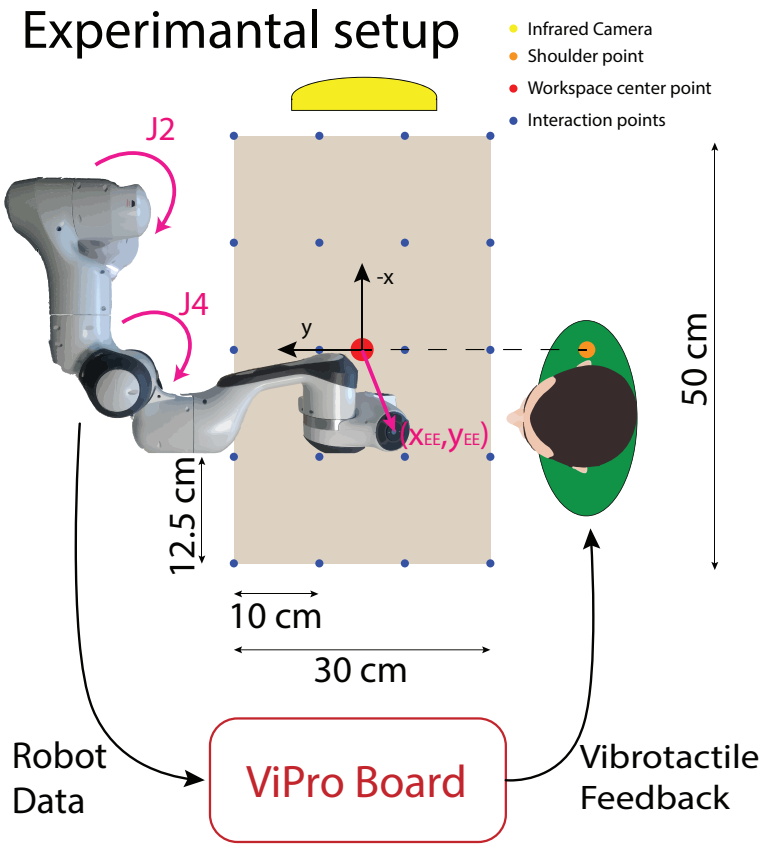

Fig. 7.4 Experimental setup scheme: a 7 dof anthropomorphic manipulator is employed as SRL; the subject is seated in front of the robot, with the right shoulder (orange dot) aligned with the center of the workspace (red dot); the workspace is a 30x50 cm rectangle subdivided into 20 equally spaced target points (blue dots). Robot state data are sent through serial communication to the ViPro board, that converts them into vibration controlling four eccentric motors placed on the user's leg skin. Robot state is represented using the end-effector position in the cartesian space (x_{EE}, y_{EE}) or the torques applied to the two active joints J_2 and J_4.

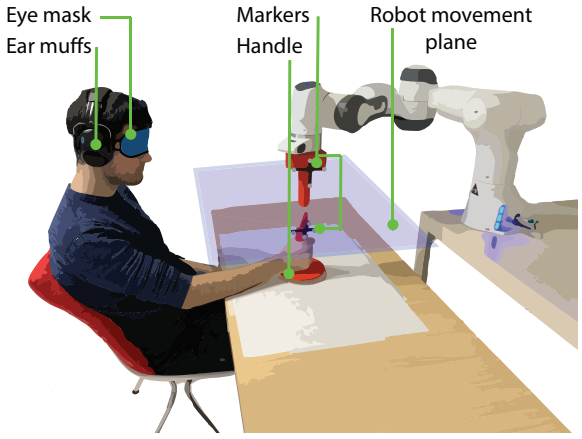

Fig. 7.5 Experimental setup with a subject seated in front of the robot. The subject holds with his right hand a plastic handle. Another plastic tool is attached to the robot end-effector. Passive markers are attached on both the handles to track them using an infrared camera. The subject moves the handle on the table; the robot tool is moved on a parallel plane. The subject wears ear muffs and eye mask to suppress auditory and visual feedback.

Learning

The learning phase is subdivided into two steps:

a. During the first step the subject has only to observe and associate the vibrotactile stimulus on the leg with the spatial motion of the robot without performing any movement. Auditory feedback is suppressed by ear muffs, as in all the other phases. The robot performs three series of 20 movements, randomly selected among the points highlighted on the workspace (see Fig. 7.4). The aim of this phase is to allow the subject to correlate the vibrotactile feedback to the position reached by the robot end-effector.

b. In the second learning step the robot performs again three series of 20 random movements. The subject perceives the proprioceptive feedback but is blindfolded. At the end of each robot movement (when the motors stop vibrating) the subject has to reach the point of the workspace corresponding to the position of the robot. Once the subject completed the reaching movement, the subject is allowed to see robot to understand if he reached the right position or to estimate the error magnitude. At the end of the movement, both robot and subject return to the starting position.

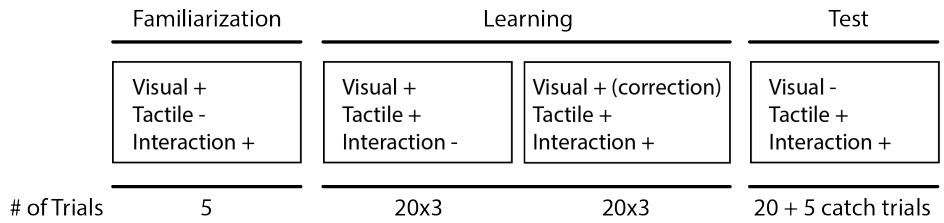

Fig. 7.6 Experimental Protocol phases: 1) Familiarization: the subject familiarizes with the experimental setup performing the task and receiving no vibrotactile feedback; 2a) Learning: the subject can see the robot motion and perceive the vibration but he does not perform the task; 2b) Learning: the subject receives the feedback and he executes the task blindfolded, looking at the actual robot position only at the end of the trial to estimate the error magnitude; 3) Test: the subject performs the task blindfolded, receiving the vibrotactile feedback with informative content 20 times and without it 5 times (catch trials).

Test

In the test phase the robot executes a series of 25 random movements. Twenty of them are associated with an informative vibrotactile feedback, whereas five movements are "catch trials" (or "control points") and provide a non-informative feedback with a sinusoidal vibration pattern (with random phase shift), in order to confirm that an eventual improvement in the performance is due to the information provided through the motors and not to the vibration itself. Subjects are blindfolded for the whole phase and they are asked to reach the correct position, depending on the received feedback.

7.3.3 Data Analysis

The robot end-effector and the handle position were tracked using the infrared camera and processed in Matlab 2017. Since the handles could also rotate during the task, two constant homogeneous transformation matrices were taken into account in the data analysis to compute the actual position of the handle centers, since the tracked markers were placed on their side, according to the equation:

$$^{b}T_{h} = ^{b}T_{m}\,^{m}T_{h} \tag{7.2}$$

where $^{b}T_{h}$ is the 4x4 homogeneous transformation matrix that represents the handle pose (h) in the base reference frame (b); $^{b}T_{m}$ is the tracked marker pose and $^{m}T_{h}$ is the constant transformation between the handle center and the attached marker. Equation 7.2 was applied to both the hand and robot handles, using the corresponding constant matrix $^{m}T_{h}$.

Performance were evaluated measuring two indexes:

- Position error, normalized with respect to the distance between the starting and target points;
- Time needed to execute the task;

The position error was computed as the cartesian norm between the handle and end-effector position on the plane, at the end of the task. The error was then normalized, dividing it by the distance between the starting and target points. This is a measure of the trial difficulty, considering that far target required higher duration to be reached, and/or higher velocity which results in less accuracy. We did not consider the accuracy to be strictly related to the proprioception, which is known not to be homogeneous in space (the accuracy in locating the hand is higher if the hand is closer to the body) [133], because the task did not rely on proprioception only, even though the subject was blind-folded. Indeed, active movements and somatosensory information derived from the interaction between hand, handle and table were always present.
The task started when the robot and the vibrotactile feedback stopped and it ended when the subject reached the target. Also the time measure was then divided by the distance between the starting and target points, used as index of the trial difficulty.
Considering the low size of the population enrolled, in order to check whether there was a within subject difference between the two feedback provided, we evaluated the effect size by computing the Cohen's d [134], [135].

7.4 Results

The average errors among the three subjects, during the test trials, are respectively $89.5 \pm 37.2mm$ using the position feedback and $194.8 \pm 88.5mm$ employing the torque feedback. These are absolute values, not normalized, and are spatially distributed as depicted in Fig. 7.7.

Taking into account the trial difficulty (represented by the distance between the starting and target points, as presented in section 7.3.3) the average error value became $48\% \pm 12\%$ in the kinematic approach and $118\% \pm 72\%$ in the dynamic one. Especially in the latter method, the worst errors are the targets close to the center, i.e. the easiest ones (as visible in Fig. 7.8); whereas the error values employing the position feedback are approximately equally distributed in the workspace.

Fig. 7.9 shows the distribution of the error and the trial duration, both divided by the target distance, for the two feedback types (computed among the 20 test trials) and for the control trials for the three subjects.

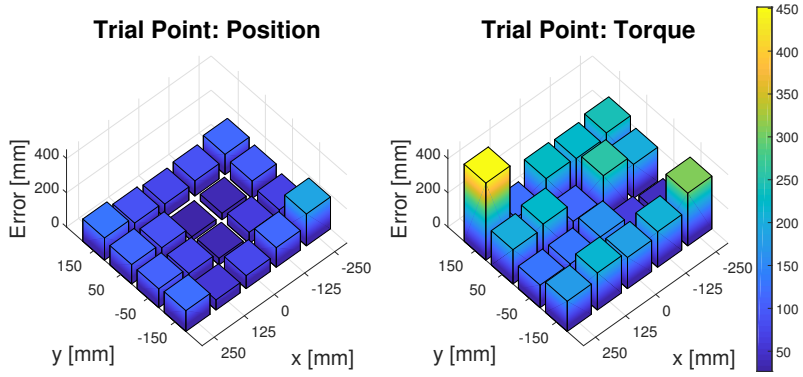

Fig. 7.7 Spatial distribution of the average error over the workspace using the position and torque feedback encoding. Each bar represents a target point. The bar height is the average error value for all the subjects corresponding to that point.

The normalized position errors, using the cartesian position feedback, are smaller than the ones recorded providing the joint torque encoding, with a huge difference between the two ($d = 4.278$) [134]. On the other hand, if we look at the control points, there is a small difference between the errors obtained with the non-informative feedback and the ones achieved with the dynamic feedback approach ($d = 0.313$). On the contrary, the kinematic encoding approach allows to achieve performance hugely better ($d = 2.826$) than the control trials, in term of errors.

Very large differences occur among the two feedback approaches in term of task duration ($d = 1.682$); the mean duration of each trial (corresponding to one target point) is $9.10s \pm 1.68s$ and $7.26s \pm 1.46s$ for the torque and position feedback respectively. The same trend is found also taking into account the trial difficulty, i.e. diving the value by the distance to be traveled ($d = 2.239$).

7.5 Discussion

The comparison with the catch trials results suggests that the position encoding is an effective feedback to let the user understand the position of the supernumerary limb, even without visual feedback. Conversely, providing the torque feedback leads to the same outcomes of a non-informative vibrotactile stimulation. Moreover, this approach achieved the worse performance in the easiest targets (see Fig. 7.8).

However, these results could have been affected by the trajectory implemented to control the robot. Indeed, the robot movement duration was always the same, i.e. four seconds, even for small distances. The torques required to slowly move the two active joints, especially

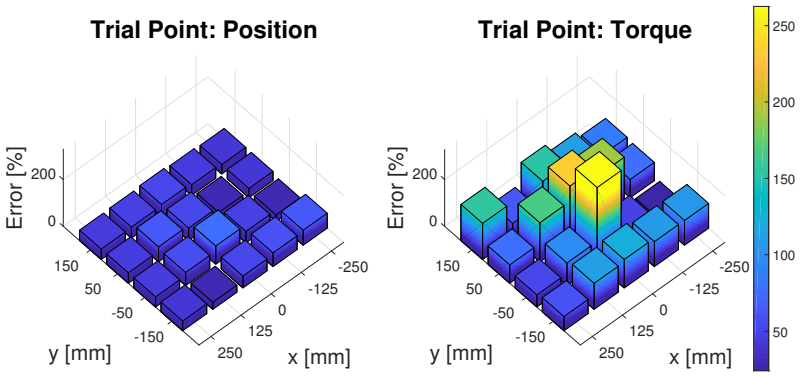

Fig. 7.8 Spatial distribution of the average normalized error over the workspace using the position and torque feedback encoding. Each bar represents a target point. The bar height is the average error value (divided by the starting-target points distance) for all the subjects corresponding to that point.

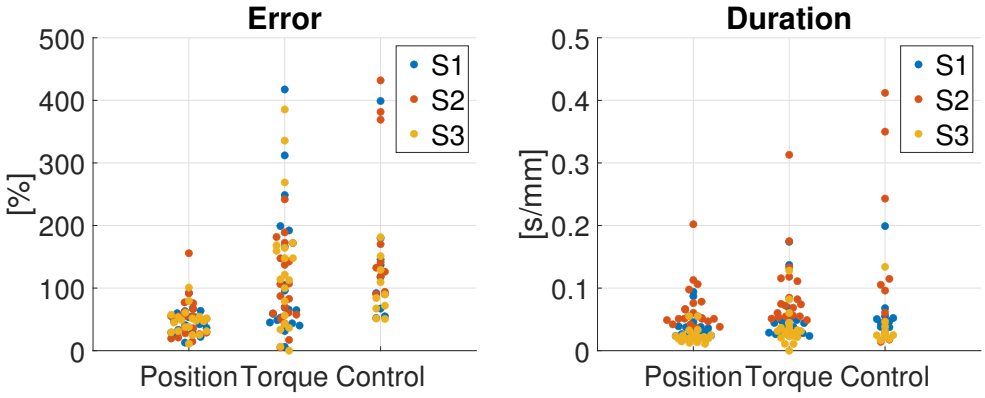

Fig. 7.9 Left: Normalized position error during the test phase (twenty trials per subject) for subjects S1, S2 and S3, using the Position and Torque feedback or in the Control trials. Right: Trial duration during the test phase (twenty trials per subject), for subjects S1, S2 and S3, using the Position and Torque feedback or during the Catch trials, all divided by the distance from the target.

because of the robot configuration that has been adapted to the planar task, probably present no perceivable differences among the selected workspace, even though the δ variability range (Eq. 7.1) was in each case adjusted according to the minimum and maximum values achievable with the employed feedback. In order to better understand the effectiveness of that feedback an additional, more complex, task should be tested.

The results prove the validity of the proposed system which seems effective in converting the state of a supernumerary robotic arm, coded using position feedback, into vibrotactile stimulation easily understandable by subjects. The huge difference between the performance achieved employing the position feedback and the ones obtained in the catch trials is an evidence of that validation.

Moreover, the learning time is not a negligible aspect. The choice of sixty trials for the two learning phases allowed to complete the whole experiment in a short span, i.e. less than one hour and half.

Such short time could have been enough to learn how to benefit from the simpler feedback (cartesian position), but too short for the more complex dynamic feedback.
It is worth noting also that the error magnitude is partially due to the inaccuracies of human beings in identifying the position of their own arm when blind-folded.
A weakness of this protocol could have been the use of the right arm and right leg instead of the dominant ones for each subject. Nevertheless, since each subject was tested with the same hand (and leg) on both the conditions, this choice may have affected the error magnitude, but not the overall comparison results.

7.6 Conclusions

The proposed platform overcomes the lack of a proprioceptive feedback, meant as the state of the entire device, in the use of SRL.

The results proved the effectiveness of the proprioceptive feedback system for a SRL using the position approach, showing clearly better performance ($d = 2.826$) compared to catch trials (providing non-informative feedback).

On the other hand, the torques approach outcomes seem significantly worse. Nevertheless, those results could be affected by the choice of a planar task and the trajectory planning implemented for the robot motions.

Besides possible limitations of the protocol employed (the lack of dynamic interactions with the environment, the use of right limbs instead of dominant ones), the proposed system showed to be a valid test-bed to implement future more complex and refined tasks to investigate the encoding of supernumerary limbs proprioceptive feedback.

Future plans will consider tasks with external disturbs, such as obstacles to avoid, or additional force fields and trimanual tasks. Furthermore, the system can be employed in studies focused on the SRL control strategies, assessing how the proprioceptive feedback affects the performance in controlling the robot.

Chapter 8

Conclusions

This work investigated the use of robotic technologies, in particular anthropomorphic manipulator, for human enhancement, both through substitution and augmentation.
A typical case of substitution, i.e. telerobotics, was addressed in the first chapter. The human arm was used as master to control a robotic manipulator using magneto-inertial sensors. The redundancy of the robot, with 7 dof, was exploited to implement anthropomorphic constraints on the robot motion. Results assessed that constraining the robot elbow configuration to be as close as possible to the human elbow one improves the control performance in reaching tasks. This means that people can better control a robotic manipulator if its movements are human-like.
A similar teleoperation approach was employed to control a human avatar in a virtual reality platform, presented in chapter 3. The platform was designed to integrate in a single setup the most relevant measures and stimulation protocols to study the multisensory integration. The validation confirmed the cross-modal congruency effect: although the small correlation coefficient, people seem to react faster to tactile stimuli on their hand if visual stimuli are simultaneously presented near the same hand. The main value of the platform is on one hand the possibility to study several multisensory integration cases with the same setup; on the other hand, thanks to the virtual reality environment, the platform allows to investigate this phenomena also in amputees. This opens many possibilities in the understanding of the embodiment mechanisms useful both for prostheses and supernumerary limbs.
Going further in the human substitution, we presented a robot-aided TMS platform in chapter 4. On one side we proposed a calibration method -constraining the workpace to a spherical shell centered in the head- to optimize and improve the calibration errors in TMS application, regardless to the mathematical implementation. On the other side, the robotic system was validated in real TMS sessions, assessing its efficacy in coil positioning and in evoking motor potentials, comparable to human operators, showing also better accuracy in achieving the

correct coil orientation. The robotic system was controlled by using impedance control that allows to maintain the right coil position, compensating for head's movements, while guaranteeing the subjects comfort and safety. The TMS is a painless technique useful to investigate the brain mechanisms and increase our knowledge on the body schema, the embodiment and the use of extra-limbs. The platform represents a powerful tool to automatize the procedure and provide a low-cost and reproducible alternative to the few available commercial devices.
Going beyond the development of robotic platforms for the study of the human enhancement, we studied the augmentation in term of human performance in three-hands tasks, control of extra-limb through EMG and vibrotactile interface for providing feedback of supernumerary robotic limbs.
From the investigation of three-hands tasks it resulted that people perform better in task with a single target, compared with different sub-tasks, even though their limbs are mechanically coupled, thus requiring greater coordination. Moreover, people perform better in dyads than alone in all the tasks, but the performance difference decreases in the three-coupled-hands task (with one single target), suggesting that the use of an extra limb controlled by the same person could be preferable to a human assistant only in specific scenarios.
Going further in the supernumerary limb topic, the author implemented a High Density EMG interface for the leg to control the 2 dof of a virtual cursor. The interface represents an attempt to make the control of an extra-limb as intuitive and similar to the natural control as possible, with the possibilities to control many degrees of freedom without affecting the natural arms movement. Preliminary results show the efficacy of the control after few minutes of training.
Finally, since the bidirectional communication is a key factor in the use of extra robotic limbs, we developed and validated a vibrotactile interface to provide the proprioceptive feedback of a robotic arm. After a training session, people were able to identify the position of the robot end-effector on a table only through the vibrotactile information, without the vision. In particular, the best way to convey the feedback was providing a vibration intensity proportional to the end-effector cartesian coordinates.

Author's contribution

Summing up, this work presented several representative examples of how robotic technologies can be used to enhance humans, both substituting and augmenting their limbs. Furthermore, the substitution cases provided results -and useful instruments- to increase the knowledge on the human brain mechanisms involved in the embodiment of external tools: a key factor for the prosthesis and supernumerary limbs evolution.
The main findings are summarized as follows:

Part I

In the first part different teleoperation strategies are presented, validated both on real system and in virtual environment, using M-IMU sensors and stereotaxic systems. Also, an optimization calibration method and an impedance-based control approach of an automatic TMS system is proposed.
Besides proposing useful a reproducible implementation, this thesis also presented the validation of the proposed solutions, whose main results can be resumed as follows:

- **Teleoperation and Anthropomorphism**: the use of arm movements as input, thanks to the M-IMU sensors, allows the user to control the robot more easily and intuitively than traditional master interfaces. Although the three control approaches has comparable performance in term of inverse kinematics errors, the Elastic Potential method shows the lowest position errors reaching the targets. This suggests its easier use with respect to the other methods.

- **Virtual Reality and Multisensory Integration**: the main advantage of the proposed platform is the possibility to test different protocols, acquiring several measures with high accuracy and using one single system. The validation experiment confirms the existence of an hand-centered peripersonal space, revealing lower reaction times to tactile stimuli if visual stimuli are simultaneously presented near the subject's hand.

- **Robot-aided TMS platform**: the platform presented in chapter 4 represents a low-cost and reproducible alternative to the few robotic TMS systems commercially available and it was used to validate an optimization method for the hand-eye and robot-world calibration. The optimization approach allows to significantly reduce the calibration errors (by 35% for the position and 19% for the orientation) regardless to the mathematical implementation. The platform with the proposed impedance control reduces the coil orientation error by 46% with respect to the expert operators. The coil position and the amplitude of the MEP result comparable to the ones measured in the manual sessions, confirming the efficacy of the proposed platform in administering TMS.

Part II

The second part focused on the augmentation topic, investigated from three points of view: human performance in three-hands tasks, control and feedback of supernumerary limb. The main results of the three aspects are here reported:

- **Trimanual Tasks**: results shows that having one target, in the three-coupled task, is easier and leads to better performance, compared to the independent and 2-coupled task, regardless to the harder mechanical coupling. Unexpectedly, people perform better in dyads than controlling three limbs alone, not only in term of score, but also in term of limbs coordination and smoothness.

- **EMG Control of a Supernumerary Limb**: the preliminary validation assesses the efficacy of the EMG leg interface to control with good accuracy a cursor on a screen, improving the user performance with only few minutes of training. The validation proves the system easiness of use.
- **Proprioceptive Feedback of a Supernumerary Limb**: the vibtotactile system, positioned on the leg, allows to effectively identify the robot end-effector position on a table using the position feedback (i.e. conveying the end-effector position through vibration amplitude), whereas the use of the torque feedback (i.e. conveying the joint torques through vibration amplitude) leads to performance comparable to a non-informative feedback.

References

[1] B. Siciliano, L. Sciavicco, L. Villani, and G. Oriolo, *Robotics: modelling, planning and control*. Springer Science & Business Media, 2010.

[2] R. M. Murray, Z. Li, S. S. Sastry, and S. S. Sastry, *A mathematical introduction to robotic manipulation*. CRC press, 1994.

[3] F. Wu and H. Asada, "Supernumerary robotic fingers: an alternative upper-limb prosthesis," in *ASME 2014 Dynamic Systems and Control Conference*. American Society of Mechanical Engineers Digital Collection, 2014.

[4] I. Hussain, G. Spagnoletti, G. Salvietti, and D. Prattichizzo, "An emg interface for the control of motion and compliance of a supernumerary robotic finger," *Frontiers in neurorobotics*, vol. 10, p. 18, 2016.

[5] B. Llorens-Bonilla, F. Parietti, and H. H. Asada, "based control of supernumerary robotic limbs," in *2012 IEEE/RSJ International Conference on Intelligent Robots and Systems*. IEEE, 2012, pp. 3936–3942.

[6] G. Di Pino, A. Maravita, L. Zollo, E. Guglielmelli, and V. Di Lazzaro, "Augmentation-related brain plasticity," *Frontiers in systems neuroscience*, vol. 8, p. 109, 2014.

[7] G. Di Pino, E. Guglielmelli, and P. M. Rossini, "Neuroplasticity in amputees: main implications on bidirectional interfacing of cybernetic hand prostheses," *Progress in neurobiology*, vol. 88, no. 2, pp. 114–126, 2009.

[8] G. Di Pino, D. Romano, C. Spaccasassi, A. Mioli, M. D'Alonzo, R. Sacchetti, E. Guglielmelli, L. Zollo, V. Di Lazzaro, V. Denaro *et al.*, "Sensory-and action-oriented embodiment of neurally-interfaced robotic hand prostheses," *Frontiers in Neuroscience*, vol. 14, 2020.

[9] T. B. Sheridan, "Telerobotics," *Automatica*, vol. 25, no. 4, pp. 487–507, 1989.

[10] B. Siciliano and O. Khatib, *Springer handbook of robotics*. Springer, 2016.

[11] [Online]. Available: "http://www.davincisurgery.com"

[12] J. Cui, S. Tosunoglu, R. Roberts, C. Moore, and D. W. Repperger, "A review of teleoperation system control," in *Proceedings of the Florida Conference on Recent Advances in Robotics*. Florida Atlantic University Boca Raton, FL, 2003, pp. 1–12.

[13] Y. Wang and P. Artemiadis, "Closed-form inverse kinematic solution for anthropomorphic motion in redundant robot arms," *Adv Robot Autom*, vol. 2, no. 110, p. 2, 2013.

[14] M. Liarokapis, C. P. Bechlioulis, P. K. Artemiadis, and K. J. Kyriakopoulos, "Deriving humanlike arm hand system poses," *Journal of Mechanisms and Robotics*, vol. 9, no. 1, 2017.

[15] P. K. Artemiadis, P. T. Katsiaris, and K. J. Kyriakopoulos, "A biomimetic approach to inverse kinematics for a redundant robot arm," *Autonomous Robots*, vol. 29, no. 3-4, pp. 293–308, 2010.

[16] J. M. Hollerbach and S. C. Jacobsen, "Anthropomorphic robots and human interactions," in *Proc. of the 1st International Symposium on Humanoid Robots*. Citeseer, 1996, pp. 83–91.

[17] F. Cordella, L. Zollo, and E. Guglielmelli, "A rgb-d camera-based approach for robot arm-hand teleoperated control," in *20th IMEKO TC-4 International Symposium Measurement of Electrical Quantities, Special Session on Transducers for robot autonomous navigation*, 2014.

[18] C. Lauretti, F. Cordella, F. S. di Luzio, S. Saccucci, A. Davalli, R. Sacchetti, and L. Zollo, "Comparative performance analysis of m-imu/emg and voice user interfaces for assistive robots," in *2017 International Conference on Rehabilitation Robotics (ICORR)*. IEEE, 2017, pp. 1001–1006.

[19] M. V. Liarokapis, P. K. Artemiadis, and K. J. Kyriakopoulos, "Functional anthropomorphism for human to robot motion mapping," in *2012 IEEE RO-MAN: The 21st IEEE International Symposium on Robot and Human Interactive Communication*. IEEE, 2012, pp. 31–36.

[20] M. V. Liarokapis, P. K. Artemiadis, C. P. Bechlioulis, and K. J. Kyriakopoulos, "Directions, methods and metrics for mapping human to robot motion with functional anthropomorphism: A review," *School of Mechanical Engineering, National Technical University of Athens*, vol. 10, 2013.

[21] R. N. Rohling, J. M. Hollerbach, and S. C. Jacobsen, "Optimized fingertip mapping: a general algorithm for robotic hand teleoperation," *Presence: Teleoperators & Virtual Environments*, vol. 2, no. 3, pp. 203–220, 1993.

[22] E. Papaleo, L. Zollo, N. Garcia-Aracil, F. J. Badesa, R. Morales, S. Mazzoleni, S. Sterzi, and E. Guglielmelli, "Upper-limb kinematic reconstruction during stroke robot-aided therapy," *Medical & biological engineering & computing*, vol. 53, no. 9, pp. 815–828, 2015.

[23] J. Koenemann, F. Burget, and M. Bennewitz, "Real-time imitation of human whole-body motions by humanoids," in *2014 IEEE International Conference on Robotics and Automation (ICRA)*. IEEE, 2014, pp. 2806–2812.

[24] T. Asfour and R. Dillmann, "Human-like motion of a humanoid robot arm based on a closed-form solution of the inverse kinematics problem," in *Proceedings 2003 IEEE/RSJ International Conference on Intelligent Robots and Systems (IROS 2003)(Cat. No. 03CH37453)*, vol. 2. IEEE, 2003, pp. 1407–1412.

[25] R. Bischoff, J. Kurth, G. Schreiber, R. Koeppe, A. Albu-Schäffer, A. Beyer, O. Eiberger, S. Haddadin, A. Stemmer, G. Grunwald *et al.*, "The kuka-dlr lightweight robot arm-a new reference platform for robotics research and manufacturing," in *ISR 2010 (41st international symposium on robotics) and ROBOTIK 2010 (6th German conference on robotics)*. VDE, 2010, pp. 1–8.

[26] X. Technologies. [Online]. Available: "http://www.xsens.com"

[27] C. Lauretti, F. Cordella, E. Guglielmelli, and L. Zollo, "Learning by demonstration for planning activities of daily living in rehabilitation and assistive robotics," *IEEE Robotics and Automation Letters*, vol. 2, no. 3, pp. 1375–1382, 2017.

[28] G. Bellusci, F. Dijkstra, and P. Slycke, "Xsens mtw: Miniature wireless inertial motion tracker for highly accurate 3d kinematic applications," *Xsens Technologies*, 2013.

[29] L. Ricci, D. Formica, L. Sparaci, F. R. Lasorsa, F. Taffoni, E. Tamilia, and E. Guglielmelli, "A new calibration methodology for thorax and upper limbs motion capture in children using magneto and inertial sensors," *Sensors*, vol. 14, no. 1, pp. 1057–1072, 2014.

[30] S. Girard, M. Pelland, F. Lepore, and O. Collignon, "Impact of the spatial congruence of redundant targets on within-modal and cross-modal integration," *Experimental brain research*, vol. 224, no. 2, pp. 275–285, 2013.

[31] M. A. Meredith and B. E. Stein, "Visual, auditory, and somatosensory convergence on cells in superior colliculus results in multisensory integration," *Journal of neurophysiology*, vol. 56, no. 3, pp. 640–662, 1986.

[32] N. P. Holmes and C. Spence, "The body schema and multisensory representation (s) of peripersonal space," *Cognitive processing*, vol. 5, no. 2, pp. 94–105, 2004.

[33] M. Tsakiris, L. Carpenter, D. James, and A. Fotopoulou, "Hands only illusion: multisensory integration elicits sense of ownership for body parts but not for non-corporeal objects," *Experimental Brain Research*, vol. 204, no. 3, pp. 343–352, 2010.

[34] C. Spence, F. Pavani, and J. Driver, "Spatial constraints on visual-tactile cross-modal distractor congruency effects," *Cognitive, Affective, & Behavioral Neuroscience*, vol. 4, no. 2, pp. 148–169, 2004.

[35] M. Botvinick and J. Cohen, "Rubber hands 'feel'touch that eyes see," *Nature*, vol. 391, no. 6669, pp. 756–756, 1998.

[36] M. D'Alonzo, A. Mioli, D. Formica, L. Vollero, and G. Di Pino, "Different level of virtualization of sight and touch produces the uncanny valley of avatar's hand embodiment," *Scientific reports*, vol. 9, no. 1, pp. 1–11, 2019.

[37] M. Bassolino, M. Franza, J. Bello Ruiz, M. Pinardi, T. Schmidlin, M. Stephan, M. Solcà, A. Serino, and O. Blanke, "Non-invasive brain stimulation of motor cortex induces embodiment when integrated with virtual reality feedback," *European Journal of Neuroscience*, vol. 47, no. 7, pp. 790–799, 2018.

[38] A. Serino, "Peripersonal space (pps) as a multisensory interface between the individual and the environment, defining the space of the self," *Neuroscience & Biobehavioral Reviews*, 2019.

[39] T. R. Makin, N. P. Holmes, and E. Zohary, "Is that near my hand? multisensory representation of peripersonal space in human intraparietal sulcus," *Journal of Neuroscience*, vol. 27, no. 4, pp. 731–740, 2007.

[40] J. B. Mattingley, J. Driver, N. Beschin, and I. H. Robertson, "Attentional competition between modalities: extinction between touch and vision after right hemisphere damage," *Neuropsychologia*, vol. 35, no. 6, pp. 867–880, 1997.

[41] M. B. Bender and D. S. Feldman, "Extinction of taste sensation on double simultaneous stimulation." *Neurology*, vol. 2, no. 3, pp. 195–202, 1952.

[42] M. S. Graziano and D. F. Cooke, "Parieto-frontal interactions, personal space, and defensive behavior," *Neuropsychologia*, vol. 44, no. 6, pp. 845–859, 2006.

[43] J. Cléry, O. Guipponi, C. Wardak, and S. B. Hamed, "Neuronal bases of peripersonal and extrapersonal spaces, their plasticity and their dynamics: knowns and unknowns," *Neuropsychologia*, vol. 70, pp. 313–326, 2015.

[44] M. Avillac, S. B. Hamed, and J.-R. Duhamel, "Multisensory integration in the ventral intraparietal area of the macaque monkey," *Journal of Neuroscience*, vol. 27, no. 8, pp. 1922–1932, 2007.

[45] E. Làdavas and A. Serino, "Action-dependent plasticity in peripersonal space representations," *Cognitive neuropsychology*, vol. 25, no. 7-8, pp. 1099–1113, 2008.

[46] E. Canzoneri, E. Magosso, and A. Serino, "Dynamic sounds capture the boundaries of peripersonal space representation in humans," *PloS one*, vol. 7, no. 9, 2012.

[47] A. Zangrandi, A. Mioli, M. D'Alonzo, D. Formica, G. Pellegrino, and G. Di Pino, "Conditioning transcranial magnetic stimulation of ventral premotor cortex shortens simple reaction time," *Cortex*, vol. 121, pp. 322–331, 2019.

[48] G. J. Ettinger, M. E. Leventon, W. E. L. Grimson, R. Kikinis, V. Gugino, W. Cote, L. Sprung, L. Aglio, M. Shenton, G. Potts *et al.*, "Experimentation with a transcranial magnetic stimulation system for functional brain mapping," in *CVRMed-MRCAS'97*. Springer, 1997, pp. 477–486.

[49] C. Hovey and R. Jalinous, "The guide to magnetic stimulation," *Magstim Company Ltd July*, 2006.

[50] M. Cantone, G. Di Pino, F. Capone, M. Piombo, D. Chiarello, B. Cheeran, G. Pennisi, and V. Di Lazzaro, "The contribution of transcranial magnetic stimulation in the diagnosis and in the management of dementia," *Clinical Neurophysiology*, vol. 125, no. 8, pp. 1509–1532, 2014.

[51] G. Di Pino, G. Pellegrino, G. Assenza, F. Capone, F. Ferreri, D. Formica, F. Ranieri, M. Tombini, U. Ziemann, J. C. Rothwell *et al.*, "Modulation of brain plasticity in stroke: a novel model for neurorehabilitation," *Nature Reviews Neurology*, vol. 10, no. 10, p. 597, 2014.

[52] R. Sparing, D. Buelte, I. G. Meister, T. Pauš, and G. R. Fink, "Transcranial magnetic stimulation and the challenge of coil placement: a comparison of conventional and stereotaxic neuronavigational strategies," *Human brain mapping*, vol. 29, no. 1, pp. 82–96, 2008.

[53] W. W. Zakaria, R. Tomari, and R. Ngadengon, "Active head motion compensation of tms robotic system using neuro-fuzzy estimation," in *MATEC Web of Conferences*, vol. 56. EDP Sciences, 2016.

[54] L. Richter, G. Neumann, S. Oung, A. Schweikard, and P. Trillenberg, "Optimal coil orientation for transcranial magnetic stimulation," *PLoS One*, vol. 8, no. 4, p. e60358, 2013.

[55] A. A. de Goede, E. M. Ter Braack, and M. J. van Putten, "Accurate coil positioning is important for single and paired pulse tms on the subject level," *Brain topography*, vol. 31, no. 6, pp. 917–930, 2018.

[56] J. Ruohonen and J. Karhu, "Navigated transcranial magnetic stimulation," *Neurophysiologie clinique/Clinical neurophysiology*, vol. 40, no. 1, pp. 7–17, 2010.

[57] B. Langguth, T. Kleinjung, M. Landgrebe, D. De Ridder, and G. Hajak, "rtms for the treatment of tinnitus: the role of neuronavigation for coil positioning," *Neurophysiologie Clinique/Clinical Neurophysiology*, vol. 40, no. 1, pp. 45–58, 2010.

[58] A. T. Sack, R. Cohen Kadosh, T. Schuhmann, M. Moerel, V. Walsh, and R. Goebel, "Optimizing functional accuracy of tms in cognitive studies: a comparison of methods," *Journal of cognitive neuroscience*, vol. 21, no. 2, pp. 207–221, 2009.

[59] L. Richter, P. Trillenberg, A. Schweikard, and A. Schlaefer, "Stimulus intensity for hand held and robotic transcranial magnetic stimulation," *Brain stimulation*, vol. 6, no. 3, pp. 315–321, 2013.

[60] R. Ginhoux, P. Renaud, L. Zorn, L. Goffin, B. Bayle, J. Foucher, J. Lamy, J.-P. Armspach, and M. de Mathelin, "A custom robot for transcranial magnetic stimulation: first assessment on healthy subjects," in *2013 35th Annual International Conference of the IEEE Engineering in Medicine and Biology Society (EMBC)*. IEEE, 2013, pp. 5352–5355.

[61] J. L. Lancaster, S. Narayana, D. Wenzel, J. Luckemeyer, J. Roby, and P. Fox, "Evaluation of an image-guided, robotically positioned transcranial magnetic stimulation system," *Human brain mapping*, vol. 22, no. 4, pp. 329–340, 2004.

[62] X. Yi and R. Bicker, "Design of a robotic transcranial magnetic stimulation system," Ph.D. dissertation, University of Newcastle upon Tyne, 2012.

[63] J. Meincke, M. Hewitt, G. Batsikadze, and D. Liebetanz, "Automated tms hotspot-hunting using a closed loop threshold-based algorithm," *NeuroImage*, vol. 124, pp. 509–517, 2016.

[64] S. Harquel, J. Diard, E. Raffin, B. Passera, G. Dall'Igna, C. Marendaz, O. David, and A. Chauvin, "Automatized set-up procedure for transcranial magnetic stimulation protocols," *Neuroimage*, vol. 153, pp. 307–318, 2017.

[65] [Online]. Available: "https://www.ant-neuro.com/products/smartmove"

[66] [Online]. Available: "http://www.axilumrobotics.com/en/tms-robot"

[67] [Online]. Available: "http://www.ying-chi.net/en/Product/info.html"

[68] J. Heller, D. Henrion, and T. Pajdla, "Hand-eye and robot-world calibration by global polynomial optimization," in *2014 IEEE international conference on robotics and automation (ICRA)*. IEEE, 2014, pp. 3157–3164.

[69] M. Shah, "Solving the robot-world/hand-eye calibration problem using the kronecker product," *Journal of Mechanisms and Robotics*, vol. 5, no. 3, p. 031007, 2013.

[70] A. Tabb and K. M. A. Yousef, "Parameterizations for reducing camera reprojection error for robot-world hand-eye calibration," in *2015 IEEE/RSJ International Conference on Intelligent Robots and Systems (IROS)*. IEEE, 2015, pp. 3030–3037.

[71] R. Y. Tsai and R. K. Lenz, "A new technique for fully autonomous and efficient 3d robotics hand/eye calibration," *IEEE Transactions on robotics and automation*, vol. 5, no. 3, pp. 345–358, 1989.

[72] H. Li, Q. Ma, T. Wang, and G. S. Chirikjian, "Simultaneous hand-eye and robot-world calibration by solving the $ax = yb$ problem without correspondence," *IEEE Robotics and Automation Letters*, vol. 1, no. 1, pp. 145–152, 2015.

[73] L. Wu, J. Wang, L. Qi, K. Wu, H. Ren, and M. Q.-H. Meng, "Simultaneous hand–eye, tool–flange, and robot–robot calibration for comanipulation by solving the $AXB = YCZ$ problem," *IEEE TRansactions on robotics*, vol. 32, no. 2, pp. 413–428, 2016.

[74] A. Tabb and K. M. A. Yousef, "Solving the robot-world hand-eye (s) calibration problem with iterative methods," *Machine Vision and Applications*, vol. 28, no. 5-6, pp. 569–590, 2017.

[75] J. Ha, D. Kang, and F. C. Park, "A stochastic global optimization algorithm for the two-frame sensor calibration problem," *IEEE Transactions on Industrial Electronics*, vol. 63, no. 4, pp. 2434–2446, 2016.

[76] F. Dornaika and R. Horaud, "Simultaneous robot-world and hand-eye calibration," *IEEE transactions on Robotics and Automation*, vol. 14, no. 4, pp. 617–622, 1998.

[77] H. Zhuang, Z. S. Roth, and R. Sudhakar, "Simultaneous robot/world and tool/flange calibration by solving homogeneous transformation equations of the form ax= yb," *IEEE Transactions on Robotics and Automation*, vol. 10, no. 4, pp. 549–554, 1994.

[78] L. Richter, F. Ernst, A. Schlaefer, and A. Schweikard, "Robust real-time robot–world calibration for robotized transcranial magnetic stimulation," *The International Journal of Medical Robotics and Computer Assisted Surgery*, vol. 7, no. 4, pp. 414–422, 2011.

[79] L. Richter, L. Matthäus, A. Schlaefer, and A. Schweikard, "Fast robotic compensation of spontaneous head motion during transcranial magnetic stimulation (tms)," 2010.

[80] F. Ernst, L. Richter, L. Matthäus, V. Martens, R. Bruder, A. Schlaefer, and A. Schweikard, "Non-orthogonal tool/flange and robot/world calibration," *The International Journal of Medical Robotics and Computer Assisted Surgery*, vol. 8, no. 4, pp. 407–420, 2012.

[81] S. R. Kantelhardt, T. Fadini, M. Finke, K. Kallenberg, J. Siemerkus, V. Bockermann, L. Matthaeus, W. Paulus, A. Schweikard, V. Rohde *et al.*, "Robot-assisted image-guided transcranial magnetic stimulation for somatotopic mapping of the motor cortex: a clinical pilot study," *Acta neurochirurgica*, vol. 152, no. 2, pp. 333–343, 2010.

[82] A. T. Barker, "An introduction to the basic principles of magnetic nerve stimulation." *Journal of clinical neurophysiology: official publication of the American Electroencephalographic Society*, vol. 8, no. 1, pp. 26–37, 1991.

[83] C. Lebossé, P. Renud, B. Bayle, M. de Mathelin, O. Piecin, E. Laroche, and J. Foucher, "Robotic image-guided transcrasial magnetic stimulation," *International Journal of Computer Assisted Radiology and Surgery*, vol. 1, p. 137, 2006.

[84] A. Noccaro, L. Raiano, G. Di Pino, and D. Formica, "Evaluation of hand-eye and robot-world calibration algorithms for tms application," in *2018 7th IEEE International Conference on Biomedical Robotics and Biomechatronics (Biorob)*. IEEE, 2018, pp. 1115–1119.

[85] A. Nguyen, A. Simard-Meilleur, C. Berthiaume, R. Godbout, and L. Mottron, "Head circumference in canadian male adults: development of a normalized chart," *Int. J. Morphol*, vol. 30, no. 4, pp. 1474–1480, 2012.

[86] J. J. Heuring and D. W. Murray, "Modeling and copying human head movements," *IEEE transactions on Robotics and Automation*, vol. 15, no. 6, pp. 1095–1108, 1999.

[87] B. Kristyanto, B. B. Nugraha, A. K. Pamosoaji, and K. A. Nugroho, "Head and neck movement: simulation and kinematics analysis," *Procedia Manufacturing*, vol. 4, pp. 359–372, 2015.

[88] U. Herwig, C. Schönfeldt-Lecuona, A. P. Wunderlich, C. von Tiesenhausen, A. Thielscher, H. Walter, and M. Spitzer, "The navigation of transcranial magnetic stimulation," *Psychiatry Research: Neuroimaging*, vol. 108, no. 2, pp. 123–131, 2001.

[89] L. Matthäus, A. Giese, P. Trillenberg, D. Wertheimer, and A. Schweikard, "Solving the positioning problem in tms," *GMS CURAC*, vol. 1, 2006.

[90] N. Hogan, "Impedance control: An approach to manipulation: Part i—theory," 1985.

[91] [Online]. Available: "https://frankaemika.github.io/libfranka/"

[92] S. Rossi, M. Hallett, P. M. Rossini, A. Pascual-Leone, S. of TMS Consensus Group *et al.*, "Safety, ethical considerations, and application guidelines for the use of transcranial magnetic stimulation in clinical practice and research," *Clinical neurophysiology*, vol. 120, no. 12, pp. 2008–2039, 2009.

[93] P. M. Rossini, A. Barker, A. Berardelli, M. Caramia, G. Caruso, R. Cracco, M. Dimitrijević, M. Hallett, Y. Katayama, C. Lücking *et al.*, "Non-invasive electrical and magnetic stimulation of the brain, spinal cord and roots: basic principles and procedures for routine clinical application. report of an ifcn committee," *Electroencephalography and clinical neurophysiology*, vol. 91, no. 2, pp. 79–92, 1994.

[94] P. M. Rossini, D. Burke, R. Chen, L. Cohen, Z. Daskalakis, R. Di Iorio, V. Di Lazzaro, F. Ferreri, P. Fitzgerald, M. George *et al.*, "Non-invasive electrical and magnetic stimulation of the brain, spinal cord, roots and peripheral nerves: basic principles and procedures for routine clinical and research application. an updated report from an ifcn committee," *Clinical Neurophysiology*, vol. 126, no. 6, pp. 1071–1107, 2015.

[95] J. Rodseth, E. P. Washabaugh, and C. Krishnan, "A novel low-cost approach for navigated transcranial magnetic stimulation," *Restorative neurology and neuroscience*, vol. 35, no. 6, pp. 601–609, 2017.

[96] L. Richter, R. Bruder, A. Schlaefer, and A. Schweikard, "Towards direct head navigation for robot-guided transcranial magnetic stimulation using 3d laserscans: Idea, setup and feasibility," in *2010 Annual International Conference of the IEEE Engineering in Medicine and Biology*. IEEE, 2010, pp. 2283–2286.

[97] H. Wang, J. Jin, X. Wang, Y. Li, Z. Liu, and T. Yin, "Non-orthogonal one-step calibration method for robotized transcranial magnetic stimulation," *Biomedical engineering online*, vol. 17, no. 1, p. 137, 2018.

[98] L. Matthäus, "A robotic assistance system for transcranial magnetic stimulation and its application to motor cortex mapping," 2008.

[99] T.-J. Tarn, Y. Wu, N. Xi, and A. Isidori, "Force regulation and contact transition control," *IEEE Control Systems Magazine*, vol. 16, no. 1, pp. 32–40, 1996.

[100] M. C. Romero, M. Davare, M. Armendariz, and P. Janssen, "Neural effects of transcranial magnetic stimulation at the single-cell level," *Nature communications*, vol. 10, no. 1, pp. 1–11, 2019.

[101] L. Lingard, R. Reznick, S. Espin, G. Regehr, and I. DeVito, "Team communications in the operating room: talk patterns, sites of tension, and implications for novices," *Academic medicine*, vol. 77, no. 3, pp. 232–237, 2002.

[102] E. Abdi, E. Burdet, M. Bouri, and H. Bleuler, "Control of a supernumerary robotic hand by foot: An experimental study in virtual reality," *PloS one*, vol. 10, no. 7, 2015.

[103] F. Y. Wu and H. H. Asada, ""hold-and-manipulate" with a single hand being assisted by wearable extra fingers," in *2015 IEEE International Conference on Robotics and Automation (ICRA)*. IEEE, 2015, pp. 6205–6212.

[104] M. Y. Saraiji, T. Sasaki, K. Kunze, K. Minamizawa, and M. Inami, "Metaarms: Body remapping using feet-controlled artificial arms," in *Proceedings of the 31st Annual ACM Symposium on User Interface Software and Technology*, 2018, pp. 65–74.

[105] C. I. Penaloza and S. Nishio, "Bmi control of a third arm for multitasking," *Science Robotics*, vol. 3, no. 20, p. eaat1228, 2018.

[106] E. Abdi, E. Burdet, M. Bouri, S. Himidan, and H. Bleuler, "In a demanding task, three-handed manipulation is preferred to two-handed manipulation," *Scientific reports*, vol. 6, p. 21758, 2016.

[107] Y. Huang, E. Burdet, L. Cao, P. T. Phan, A. M. H. Tiong, P. Zheng, and S. J. Phee, "Performance evaluation of a foot-controlled human-robot interface," *arXiv preprint arXiv:1903.03266*, 2019.

[108] D. A. Winter, *Biomechanics and motor control of human movement*. John Wiley & Sons, 2009.

[109] S. Balasubramanian, A. Melendez-Calderon, and E. Burdet, "A robust and sensitive metric for quantifying movement smoothness," *IEEE transactions on biomedical engineering*, vol. 59, no. 8, pp. 2126–2136, 2011.

[110] F. Parietti and H. H. Asada, "Independent, voluntary control of extra robotic limbs," in *2017 IEEE International Conference on Robotics and Automation (ICRA)*. IEEE, 2017, pp. 5954–5961.

[111] N. Parajuli, N. Sreenivasan, P. Bifulco, M. Cesarelli, S. Savino, V. Niola, D. Esposito, T. J. Hamilton, G. R. Naik, U. Gunawardana *et al.*, "Real-time emg based pattern recognition control for hand prostheses: a review on existing methods, challenges and future implementation," *Sensors*, vol. 19, no. 20, p. 4596, 2019.

[112] A. D. Bellingegni, E. Gruppioni, G. Colazzo, A. Davalli, R. Sacchetti, E. Guglielmelli, and L. Zollo, "Nlr, mlp, svm, and lda: a comparative analysis on emg data from people with trans-radial amputation," *Journal of neuroengineering and rehabilitation*, vol. 14, no. 1, p. 82, 2017.

[113] R. Boostani and M. H. Moradi, "Evaluation of the forearm emg signal features for the control of a prosthetic hand," *Physiological measurement*, vol. 24, no. 2, p. 309, 2003.

[114] Y. Huang, E. Burdet, L. Cao, P. T. Phan, A. M. H. Tiong, and S. J. Phee, "A subject-specific four-degree-of-freedom foot interface to control a robot arm," *arXiv preprint arXiv:1902.04752*, 2019.

[115] F. P. Kendall, E. K. McCreary, P. G. Provance, M. Rodgers, W. A. Romani *et al.*, *Muscles, testing and function: with posture and pain*. Williams & Wilkins Baltimore, MD, 1993, vol. 103.

[116] N. Jiang, H. Rehbaum, I. Vujaklija, B. Graimann, and D. Farina, "Intuitive, online, simultaneous, and proportional myoelectric control over two degrees-of-freedom in upper limb amputees," *IEEE transactions on neural systems and rehabilitation engineering*, vol. 22, no. 3, pp. 501–510, 2013.

[117] N. Jiang, K. B. Englehart, and P. A. Parker, "Extracting simultaneous and proportional neural control information for multiple-dof prostheses from the surface electromyographic signal," *IEEE transactions on Biomedical Engineering*, vol. 56, no. 4, pp. 1070–1080, 2008.

[118] S.-w. Leigh, H. Agrawal, and P. Maes, "Robotic symbionts: Interweaving human and machine actions," *IEEE Pervasive Computing*, vol. 17, no. 2, pp. 34–43, 2018.

[119] http://stelarc.org/?catID=20265.

[120] C. Véronneau, J. Denis, L.-P. Lebel, M. Denninger, J.-S. Plante, and A. Girard, "A lightweight force-controllable wearable arm based on magnetorheological-hydrostatic actuators," in *2019 International Conference on Robotics and Automation (ICRA)*. IEEE, 2019, pp. 4018–4024.

[121] F. Parietti, K. Chan, and H. H. Asada, "Bracing the human body with supernumerary robotic limbs for physical assistance and load reduction," in *2014 IEEE International Conference on Robotics and Automation (ICRA)*. IEEE, 2014, pp. 141–148.

[122] F. Parietti and H. Asada, "Supernumerary robotic limbs for human body support," *IEEE Transactions on Robotics*, vol. 32, no. 2, pp. 301–311, 2016.

[123] S. Manoharan and H. Park, "Supernumerary body schema extension to non-corporeal object by adding artificial tactile feedback using electrical stimulation," in *2019 9th International IEEE/EMBS Conference on Neural Engineering (NER)*. IEEE, 2019, pp. 989–992.

[124] B. Llorens-Bonilla, F. Parietti, and H. Asada, "Demonstration-based control of supernumerary robotic limbs. intelligent robots and systems (iros), 2012 ieee," in *RSJ International Conference on*, 2012, pp. 7–12.

[125] N. Risi, V. Shah, L. A. Mrotek, M. Casadio, and R. A. Scheidt, "Supplemental vibrotactile feedback of real-time limb position enhances precision of goal-directed reaching," *Journal of neurophysiology*, vol. 122, no. 1, pp. 22–38, 2019.

[126] A. R. Krueger, P. Giannoni, V. Shah, M. Casadio, and R. A. Scheidt, "Supplemental vibrotactile feedback control of stabilization and reaching actions of the arm using limb state and position error encodings," *Journal of neuroengineering and rehabilitation*, vol. 14, no. 1, p. 36, 2017.

[127] A. V. Cuppone, V. Squeri, M. Semprini, L. Masia, and J. Konczak, "Robot-assisted proprioceptive training with added vibro-tactile feedback enhances somatosensory and motor performance," *PloS one*, vol. 11, no. 10, p. e0164511, 2016.

[128] R. J. van Beers, D. M. Wolpert, and P. Haggard, "When feeling is more important than seeing in sensorimotor adaptation," *Current biology*, vol. 12, no. 10, pp. 834–837, 2002.

[129] J. T. Dennerlein, P. A. Millman, and R. D. Howe, "Vibrotactile feedback for industrial telemanipulators," in *Sixth Annual Symposium on Haptic Interfaces for Virtual Environment and Teleoperator Systems, ASME International Mechanical Engineering Congress and Exposition*, vol. 61, 1997, pp. 189–195.

[130] E. J. Earley, K. J. Kaveny, R. E. Johnson, L. J. Hargrove, and J. W. Sensinger, "Joint-based velocity feedback to virtual limb dynamic perturbations," in *2017 International Conference on Rehabilitation Robotics (ICORR)*. IEEE, 2017, pp. 1313–1318.

[131] A. Sengül, G. Rognini, M. van Elk, J. E. Aspell, H. Bleuler, and O. Blanke, "Force feedback facilitates multisensory integration during robotic tool use," *Experimental brain research*, vol. 227, no. 4, pp. 497–507, 2013.

[132] E. Wentink, A. Mulder, J. S. Rietman, and P. H. Veltink, "Vibrotactile stimulation of the upper leg: Effects of location, stimulation method and habituation," in *2011 Annual International Conference of the IEEE Engineering in Medicine and Biology Society*. IEEE, 2011, pp. 1668–1671.

[133] E. T. Wilson, J. Wong, and P. L. Gribble, "Mapping proprioception across a 2d horizontal workspace," *PloS one*, vol. 5, no. 7, 2010.

[134] S. S. Sawilowsky, "New effect size rules of thumb," *Journal of Modern Applied Statistical Methods*, vol. 8, no. 2, p. 26, 2009.

[135] C. O. Fritz, P. E. Morris, and J. J. Richler, "Effect size estimates: current use, calculations, and interpretation." *Journal of experimental psychology: General*, vol. 141, no. 1, p. 2, 2012.